UNIVERSITY OF SOUTHAMPTON

FACULTY OF ENGINEERING AND THE ENVIRONMENT

Institute of Complex Systems Simulation
Bioengineering Sciences Research Group

Modelling Neuronal Activity at the Knee Joint

by

Gwen Elizabeth Palmer

Thesis for the degree of Doctor of Philosophy

2013

UNIVERSITY OF SOUTHAMPTON

ABSTRACT

FACULTY OF ENGINEERING AND THE ENVIRONMENT

Institute of Complex Systems Simulation

Bioengineering Sciences Research Group

Doctor of Philosophy

MODELLING NEURONAL ACTIVITY AT THE KNEE JOINT

Gwen Elizabeth Palmer

The knee is a complex joint, prone to instability and damage, meaning a complicated architecture of soft tissues is necessary to ensure any stability of the joint. These structures are innervated, and play an important role in both proprioception, the sensing of a body's own limb positions, and nociception, the sensing of painful stimuli. The purpose of this project has been to develop a computational model that can replicate the behaviour of the mechanical sensing nerve endings in the knee joint. An adapted Hodgkin-Huxley model has been developed and used to simulate the behaviour of the nerve endings. These models have been coupled with a three dimensional finite element model of a feline knee joint, which has been built with use of x-ray CT and MRI scans of a cat's hind limb, allowing neural responses to be predicted as the position of the knee joint changes. Once the behaviour of the complete model has been verified, through comparisons with recordings of neural responses in the literature, it was possible to observe the effect of removing a soft tissue structure on the neural response. The anterior cruciate ligament (ACL) was removed from the model, and a series of tests run to determine the effect of ligament damage on neural response. It was predicted that removing the ACL from the knee joint can increase the neural responses to changes in knee position, agreeing with data in the literature. This could indicate an increase in pain at the joint, and could help with understanding the causes of pain and changes proprioception experienced by patients with damaged ACL.

Contents

List of Figures

List of Tables

Academic Thesis: Declaration Of Authorship

I, Gwen Palmer, declare that this thesis and the work presented in it are my own and has been generated by me as the result of my own original research.

Modelling Neuronal Activity at the Knee Joint

I confirm that:

1. This work was done wholly or mainly while in candidature for a research degree at this University;

2. Where any part of this thesis has previously been submitted for a degree or any other qualification at this University or any other institution, this has been clearly stated;

3. Where I have consulted the published work of others, this is always clearly attributed;

4. Where I have quoted from the work of others, the source is always given. With the exception of such quotations, this thesis is entirely my own work;

5. I have acknowledged all main sources of help;

6. Where the thesis is based on work done by myself jointly with others, I have made clear exactly what was done by others and what I have contributed myself;

7. Either none of this work has been published before submission, or parts of this work have been published as:

    - Palmer, G, Roose, T & Taylor, M (2012) *Do Ruffini Mechanoreceptors have a Preferred Sensing Direction?* Proceedings of 18th Congress of the European Society of Biomechanics, 1-4/07/2012, Lisbon, p456.

    - Palmer, G, Roose, T, Hibberd, T, Brookes, S & Taylor, M (2013) *Using digital image correlation to determine mechano-transduction behaviour of the viscerofugal neuron in the gut.* Proceedings of 19th Congress of the European Society of Biomechanics , 25-28/08/2013, Patras

Signed: ……

Date: 20/02/14

Acknowledgements

This work was undertaken with a doctoral training centre grant from the EPSRC. I would also like to express my sincere gratitude to:

- My supervisors, Prof. Mark Taylor and Prof. Tiina Roose, for their guidance and support throughout this project.
- The Institute for Complex Systems Simulation, for giving me this opportunity.
- The members of the Medical Device Research Institute at Flinders University in Adelaide for welcoming me to Australia, and assisting during my visit.
- The University of Southampton bioengineering sciences office, for their support over the last three years.
- My family and friends for their enduring support.

Abbreviations

ACL – Anterior Cruciate Ligament

CT – Computed Tomography

FE – Finite element (method)

H-H – Hodgkin-Huxley (model)

LAN – Lateral Articular Nerve

LCL – Lateral Collateral Ligament

MAN – Medial Articular Nerve

MCL – Medial Collateral Ligament

MRI – Magnetic Resonance Imaging

PAN – Posterior Articular Nerve

PCL – Posterior Cruciate Ligament

TKR – Total Knee Replacement

Definitions

A

A-fibres – myelinated nerve fibres, with large diameters of 5-20μm and high conduction velocities of 30-120m/s.

Action potential – the change in electrical potential associated with the passage of an impulse along the membrane of a muscle cell or nerve cell.

Adipose tissue – a type of body tissue containing stored fat that serves as a source of energy; it also cushions and insulates vital organs.

Axon – the long threadlike part of a nerve cell along which impulses are conducted from the cell.

B

B-fibres – myelinated nerve fibres, with diameters of 1-5μm and conduction velocities of 3-15m/s.

C

C-fibres – unmyelinated nerve fibres, with diameters of 0.2-1.5μm and conduction velocities of 0.5-2.0m/s.

Cancellous bone – also called trabecular, or spongy bone, is one of the two types of osseous tissue that form bones.

Condyle – a rounded protuberance at the end of some bones, forming an articulation with another bone.

Corpuscle – a minute body or cell in an organism.

Cortical bone – also called compact bone, is one of the two types of osseous tissue that form bones.

G

Golgi tendon organ – a type of nerve ending, a stretch receptor found mainly in the ligaments and tendons.

H

Hexahedral mesh - a mesh comprising of elements with 6 plane surfaces.

I

in vitro – taking place in a test tube, culture dish or elsewhere outside a living organism.
in vivo – taking place in a living organism.
Ion channels – locations in a cell membrane where passage of ions is possible.

L

Lamella – a thin layer, membrane, or plate of tissue, especially in bone.
Ligament – a short band of tough, flexible, fibrous connective tissue that connects two bones or cartilages or holds together a joint.

M

Mechanoreceptor – a sense organ or cell that responds to mechanical stimuli such as touch or sound.
Membrane (cell) – the thin, semi-permeable lining surrounding the cytoplasm of a cell.
Mesentery – a fold of the peritoneum which attaches the stomach small intestine, pancreas, spleen and other organs to the posterior wall of the abdomen.
Myelinated – Neurons covered with a layer of Myelin.

N

Neuron – a specialised cell transmitting nerve impulses.
Nociceptive – relating to or denoting pain arising from the stimulation of nerve cells.
Nondimensionalisation – the partial or full removal of units from an equation involving physical quantities by a suitable substitution of variables.

O

Osteoarthritis – degeneration of joint cartilage and the underlying bone, most common from middle age onward. It causes pain and stiffness, especially in the hip, knee, and thumb joints.

P

Paciniform corpuscle – a type of rapidly adapting lamellated corpuscle that responds to compression/vibration stimuli.
Plexus – a network of nerves or vessels in the body.

Proprioception – relating to stimuli that are produced and perceived within an organism, especially connected with the position and movement of the body.

R

Receptor – an organ of cell able to respond to light, heat, or other external stimulus and transmit a signal to a sensory nerve.

Ruffini ending – a type of slowly adapting nerve ending that responds to stretching stimuli.

S

Septum – a wall dividing a cavity or structure into smaller ones (plural: septae).

T

Transduction – a process in cell biology involving conversion of a signal outside the cell to a functional change within the cell.

Chapter 1

Introduction

The knee is a complex joint [1], which relies on a complicated architecture of soft tissues to ensure stability. Unfortunately this results in a joint that is highly susceptible to injuries. It is difficult to repair a damaged knee joint to a condition that will allow the same flexibility and stability of a healthy knee joint. Due to the high occurrence of injuries, this joint is a common source of pain. The origin of this pain is usually difficult to determine, since pain is a subjective entity, derived from complex processes that occur in the spinal cord and brain.

Though it can be very difficult to determine causes of pain at the knee joint, it is a heavy burden on the health care system. In an extreme case of osteoarthritis, for example, a total knee replacement (TKR) is implanted to improve function and reduce the pain experienced. TKR operations are being performed more frequently than ever, with over 84,500 primary TKR operations taking place in England and Wales in 2012 [2]. Though satisfactory function is often restored to the patient, the pain experienced post-surgery is too often at an unacceptable level [3, 4]. For example, 18% of the TKR revision procedures carried out in 2012 in England and Wales were due to unacceptable pain levels [2], and it has been reported that as many as 44% of patients still experience pain four years post TKR surgery [5]. It has also been suggested that 20% of TKR patients experience persistent pain, while 80% reported pain on movements such as standing up from a chair [6]. A better understanding of pain, and the sensory endings around the knee joint, could help to treat these patients with a higher success rate.

In 1821, Charles Bell suggested that sensory bodies in muscles contributed to a 'muscle sense' on both a conscious and subconscious level [7]. This muscle sense was later named "proprioception"; the production and perception of stimuli within an organism, especially with respect to movement and placement of parts of the body [8]. More generally, proprioception is the sense of the relative positions of parts of the body, and relies on the presence of mechanical sensing nerve endings located inside and around the tissues and joints. Thus, by definition, proprioception plays an important role in maintaining the control and balance of the body.

Precisely how proprioception around joints such as the knee is achieved is a controversial topic. There are two possible methods; one is that the sensory nerve endings at the joint itself are involved in proprioception, and the other is that sensory endings located in muscles, known as muscle spindles, are involved in proprioception. Though the more popular belief is that muscle spindles alone are involved in proprioception [9], some studies suggest that it is more likely to be a combination of joint sensory endings and muscle spindles [10, 11]. The evidence for joint sensory endings being involved in proprioception is often measured from patients with total knee replacements (TKR), where proprioception is shown to change with the addition of a TKR, and more so with sacrifice of the posterior cruciate ligament (PCL) [10, 12]. Other evidence that the sensory endings around the joint are involved in proprioception is in the type of sensory endings that have been shown to be present. There are reports that both the capsule and PCL are likely to be involved in proprioception, since these structures are innervated by the sensory nerve endings with lower thresholds [13, 14]. There are no studies, however, that attempt to find if there is any relationship between the neural response of the joint sensory endings and proprioception.

Previous studies that look at the neuromuscular system, in particular the knee joint, use invasive experimental methodologies which are extremely time consuming and ethically difficult. These studies are also limited, as it is difficult to connect the neural responses that are recorded with the pain or proprioception that are actually experienced by a patient. Due to the lack of knowledge of how the sensory neural behaviour around the knee joint is related to the sensations that are experienced, a computational model could be useful in understanding the processes that are occurring during both normal knee movement and soft tissue damage. A model of this type could not be expected to be able to predict pain or proprioception; its importance would be in indicating whether the sensory

neural response around the knee could impact proprioception, an area of controversy as described previously. The inspiration of the study described in this thesis is the lack of understanding of the relationship between proprioception and joint sensory ending response. The aim of the study has been to determine whether the sensory endings around the knee joint are likely to be involved in proprioception as well as sensing pain through the development of a model of a feline knee joint. The study focusses on the feline knee joint since this is the joint that has the more detailed neural descriptions in the literature.

This thesis describes development of a computational model for furthering our understanding of the neural systems around the knee joint. Some models already exist that describe the behaviour of nerve endings, with varying levels of complexity. Most of these involve an adapted version of the popular Hodgkin-Huxley model [15], however, none of these are related to the knee joint and very few attempt to link a mechanical model with a neural model. Those that do link the two only consider a single tissue sample and not a system such as a complete knee joint.

Published experimental work describes both the individual and global neural behaviour of nerve endings located at the feline knee joint. For this reason, this project focusses on the feline knee joint, using these studies for verification. One particularly interesting study, Gomez-Barrena et al. [16], reports that removal the anterior cruciate ligament (ACL) leads to an increase in the neural response from the remaining structures in the feline knee joint. It is hypothesised that damaging or removing a soft tissue structure in the knee joint will lead to a significant change in the neural response. The model developed in this project is used to identify the structures that are likely to be contributing to this increase in neural response, and whether this is linked with the sense of instability that is reported by patients with ACL deficient knees. The diagram in Figure 1 summarises and visualises the different stages of the study, and how they are linked together. The thesis begins by describing individual neural behaviour to local mechanical changes, and models are developed to represent this behaviour. The focus then moves onto the development of development of a feline knee joint model, before combining the models to result in a complete model that will predict neural behaviour to changes in joint position. Finally changes in neural behaviour when a soft tissue structure is removed, representing a damaged knee joint, will help to indicate whether the joint receptors are involved in proprioception. The rest of this chapter expands on the main stages of the study.

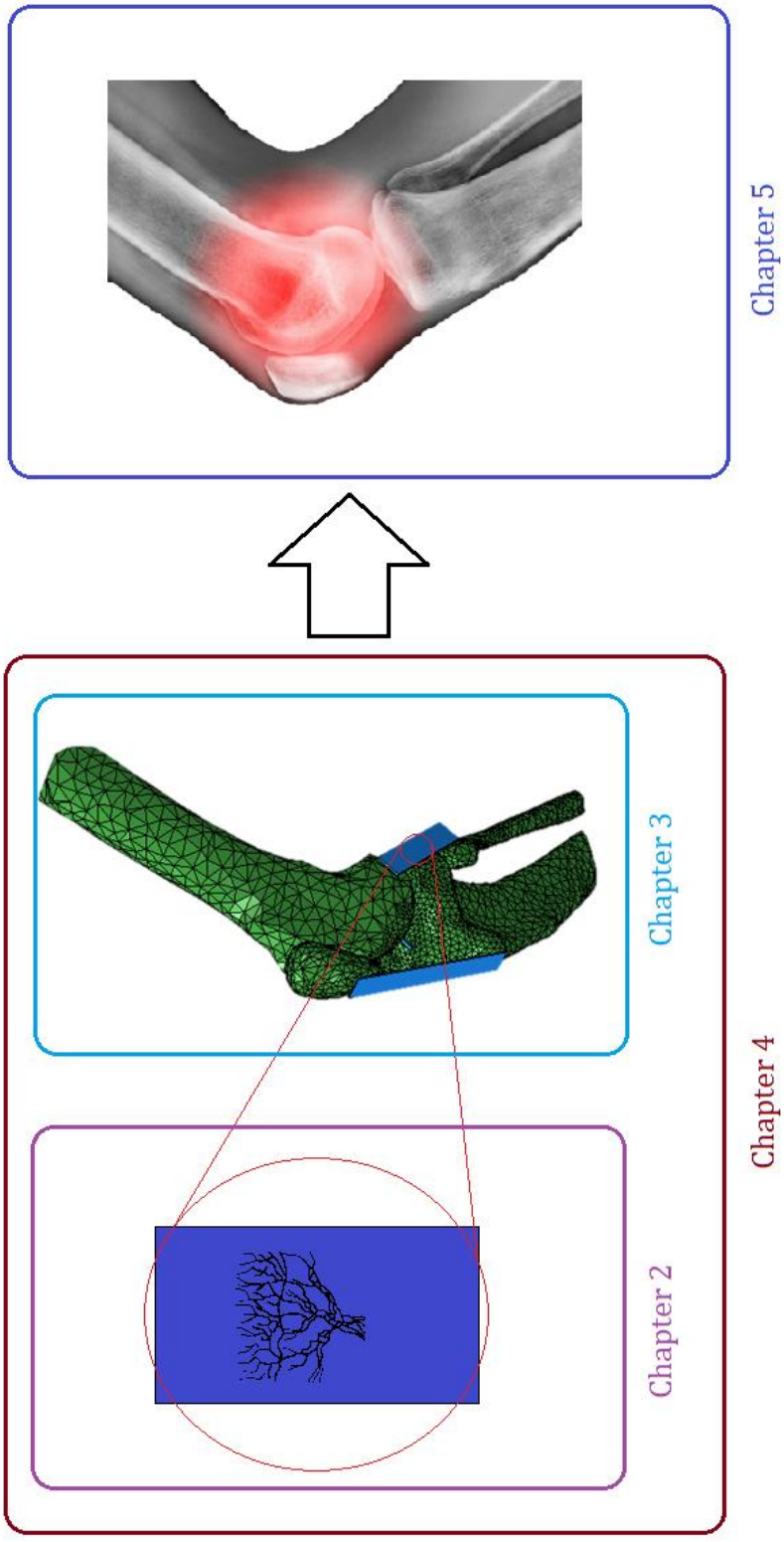

Figure 1: Diagram summarising the process followed for this thesis. Chapter 2 focusses on development of neural models, chapter 3 describes the development of a knee joint model, chapter 4 combines these models, and finally chapter 5 uses the completed model to observe changes in behaviour in a damaged knee joint.

Development of a model that can predict neural response to changes in knee joint position is ambitious, so the project has been broken down to three main stages and the modelling of the knee joint has been restricted to only include the mechanical aspects of the joint. The first of these has involved development of models that could predict the neural behaviour of individual sensory nerve endings, and is described in chapter 2. Four models are developed, to represent the behaviour of the four types of mechanical sensing endings known to be present at the knee joint [17]. In the same chapter, the generalised neural model is verified using data from the Viscerofugal neuron, in the gut of guinea pig[1].

The second part of the project involved development of a computational model that represents the feline knee joint, and is described in chapter 3. Since the majority of data available on the innervation of knee joint is based around the feline knee joint, it is sensible to develop a model of this joint. No finite element model currently exists of the feline knee joint, and current models of human knee joint do not include all soft tissue structures, such as joint capsule and fat pad, so this part of the project has required new techniques.

Chapter 4 describes linking the four neural models and feline knee joint model, so that neural responses to changes in knee joint position can be calculated. The model is shown to successfully predict neural changes during the flexion-extension movement, through verification with published experimental data. The model was then used to predict the effects of removal of anterior cruciate ligament (ACL) on neural response in chapter 5. After removing the ACL from the knee joint model, three tests were applied to the knee joint model, so that the predictions could be directly compared with the measurements of Gomez-Barrena et al. [16]; flexion-extension, anterior tibial drawer, and internal-external rotation. Finally, chapter 6 describes the conclusions of the study, and suggests future work that could benefit this field.

[1] Data collected by Timothy Hibberd at the Physiology department of Flinders University, Adelaide, South Australia.

Chapter 2

Experimental Calibration of a Model for Neuronal Response

2.1 Introduction

This chapter focusses on the development of models that can predict neural behaviour to changes in local mechanical environments; Figure 2 indicates how this chapter is linked with the overall project. Modelling methods that can describe the behaviour of nerve endings could prove valuable to the neuroscience community, however there are currently very few detailed descriptions of these model types existing. This is potentially due to the very distinct set of skills required for both modelling and experimental methods. As well as the development of a computational model, detailed experiments need to be carried out to validate the models. This chapter covers the literature relating to sensory neurons and the modelling methods available in this area, describing in detail the popular Hodgkin-Huxley (H-H) model for nerve signal generation, and its more common adaptations. The H-H model is then adapted to represent the behaviour of the four main mechanical sensing nerve endings found at the knee joint. The developed model is validated using detailed raw recordings of the neuronal response of Viscerofugal neurons, in guinea pig gut tissue, to a range of tensile loads[2].

[2] Data recorded by Timothy Hibberd, postgraduate research student at the Department of Human Physiology & Centre for Neuroscience, Flinders University, South Australia

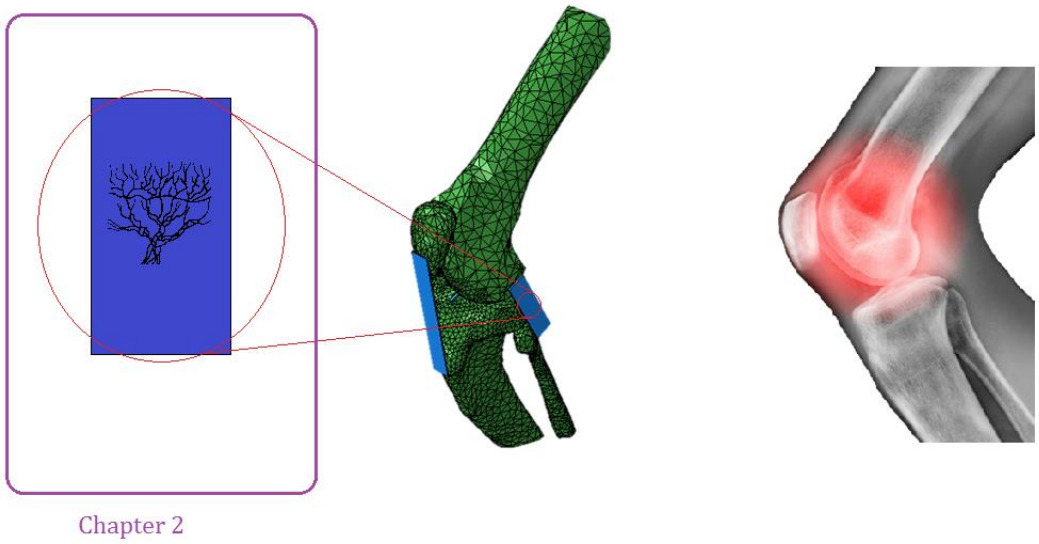

Figure 2: Diagram to highlight how the work described in chapter 2 relates to the overall project in this thesis.

Mechanical sensing nerve endings, known as mechanoreceptors, are embedded in a range of tissues and sense the mechanical changes in the local environment. They send electrical signals to the spinal cord and brain to represent these mechanical changes. Due to the difficulty in quantifying the precise mechanical environment in the soft tissues, it is often difficult to identify what stimulus is acting on the mechanoreceptor, and what the mechanoreceptor is actually responding to. For this reason, the specifics of the behaviour of the mechanoreceptor to local stimuli have not yet been reported. In addition to looking at neural modelling methods this chapter describes use of the popular engineering method, digital image correlation (DIC), to determine the local deformations experienced by a sample of soft tissue under tensile load. Figure 3 shows the process followed for this chapter.

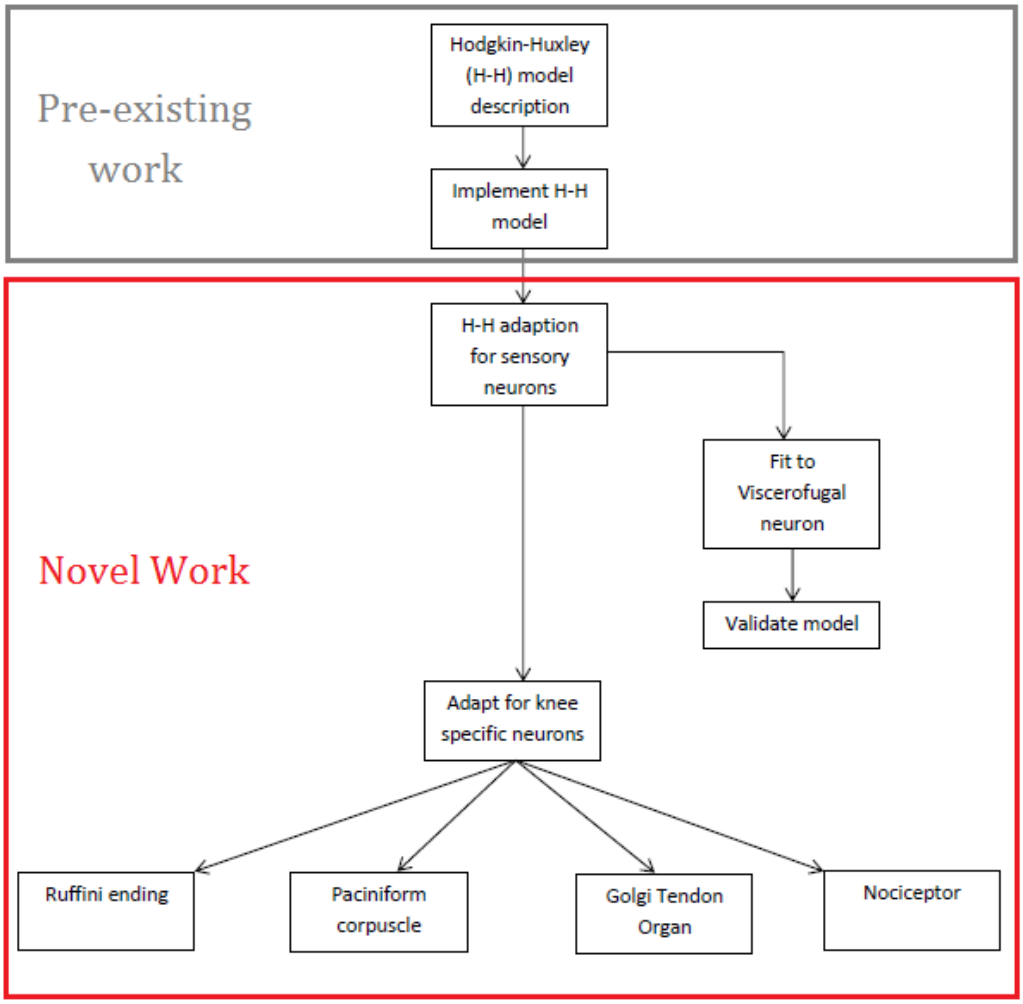

Figure 3: Flowchart for this chapter, beginning with a description and implementation of the most popular modelling method, the Hodgkin-Huxley model. This is then adapted to predict neural behaviour of sensory neurons, and tested with experimental data of the Viscerofucal neuron. Finally, once it has been shown that the H-H model can be used for modelling sensory neurons, it is adapted to represent the behaviour of the four nerve endings found at the knee joint.

2.2 Literature Review

2.2.1 A general description of nerves and the nervous system

A nerve cell, or neuron, is a specialised cell that has developed to transmit trains of action potentials [8, 18] between the brain and different areas within the body, such as soft tissues. Depending on the function of the neuron, its structure and therefore behaviour can vary accordingly. This variation has resulted in a classification system of groups A, B and C [8]; only A and C fibres branch into mechanosensors, while B fibres are associated with motor neurons. Group A fibres are larger in diameter than B and C fibres, with higher conduction velocities, and have insulating myelin sheaths along with B fibres [18]. The diameters and conduction velocities of group A fibres are highly variable, so are grouped into a further four types of nerve fibres; Aα, Aβ, Aγ, and Aδ fibres, where Aα fibres have the largest diameters and highest conduction velocities and Aδ fibres have the smallest diameters and lowest conduction velocities.

When a neuron is stimulated, an action potential is generated, which is a result of changes in concentrations of ions either side of the neuron's membrane [8]. The frequency of action potentials generated by a nerve ending represents the strength of the applied stimulus, where higher frequencies indicate higher stimulus strengths.. When a stimulus is applied to a nerve ending, the relevant ion channels open allowing movement of ions, resulting in an increased receptor potential. Morris [19] reviews mechanosensitive ion channels, and more specifically highlights the presence of stretch-activated ion channels, which are found only in mechanoreceptors. They allow movement of ions through the receptor's membrane and therefore a change in the polarity, on application of tensile force. If there is enough ion movement to result in electronegativity at the membrane, an action potential is generated [18].

Behaviour of the sensory neurons can be described as either rapidly or slowly adapting. The response of rapidly adapting receptors consists of a single action potential at the application, and sometimes the removal, of a stimulus [8]. Due to this behaviour, these types of sensors are often considered to be vibration or dynamic sensors. Slowly adapting receptors, in comparison, have a response that consists of a train of action potential peaks for the duration of a stimulus above its threshold, which stops on removal of the stimulus [8]. This type of sensor will usually be involved in the sensing of a maintained stimulus which could be mechanical, thermal or chemical; this project focusses on the mechanical sensing endings which arise from the nerve fibres with higher conduction rates.

2.2.2 Mechanoreceptors

It is the mechanical sensing nerve endings, known as mechanoreceptors, which will be considered in this section since these types of nerve endings are generally accepted to be involved in proprioception, as mentioned in chapter 1. There are four types of mechanoreceptor that have been consistently reported to be present in the knee joint. Though often under different names, they have been categorised by Freeman and Wyke [17] as types I, II, III and IV, and can be seen in Table 1.

Category	Mechanoreceptor as reported
I	Ruffini ending, Golgi-Mazzoni, Spray-type
II	Paciniform corpuscle, Krause, Vater-Pacinian corpuscle, Golgi-Mazzoni, Modified Pacinian
III	Golgi tendon organs, Golgi-Mazzoni
IV	Nociceptor, free nerve ending

Table 1: A table to summarise the categorisation Freeman and Wyke [17], which also displays the variation in naming conventions [20-26].

The names that have been carried forward throughout this thesis are Ruffini ending, Paciniform corpuscle, Golgi tendon organ (GTO) and Nociceptor. A brief description of each of these can be seen in Table 2 (page 13), along with a summary of their locations in Table 3 (page 14). Figure 4 shows the general structures of the four types of sensory endings being considered in this thesis.

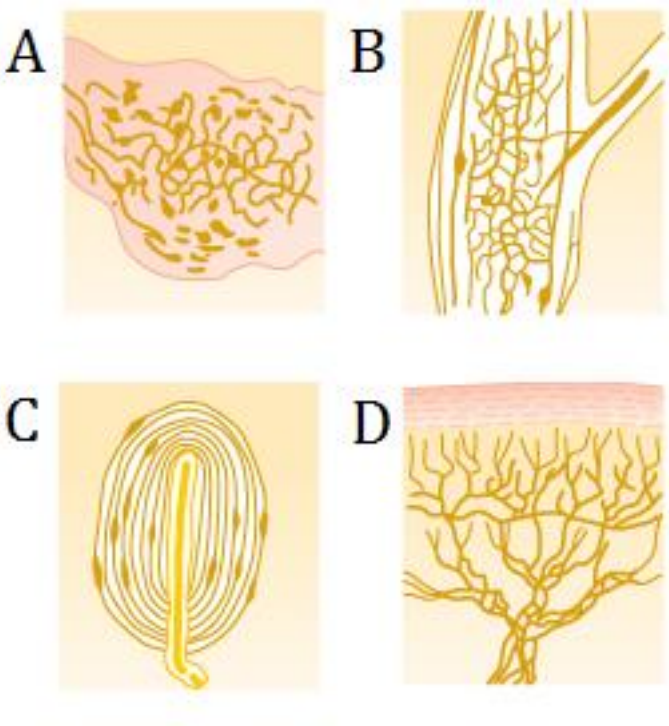

Figure 4: Diagrams of the general structures of Ruffini ending (A), Golgi Tendon Organ (B), Paciniform corpuscle (C), and Nociceptor (D) [8].

The behaviour of each of these mechanoreceptors has been researched to varying extents, with some endings having received more attention than others. Generally, the experiments that are carried out to measure neural responses to mechanical stimulation require removing the relevant mechanoreceptors along with the surrounding tissue from the knee, with the major nerve supplying the tissue still intact [21, 22, 27, 28]. Whilst ensuring the entire structure is well insulated, and immersed in an ionised bath, mechanical loads are applied to the tissue. The major nerve is dissected until a single nerve fibre is obtained, and the associated mechanoreceptor in the tissue sample identified. This nerve fibre is then placed on a recording electrode, so that any activity can be recorded. The following sub-sections will expand on the structure and behaviour of each of these mechanoreceptors with use of available data. In many cases, the published data specific to synovial joints is sparse, which could be due to their variability and the difficulty in obtaining the nerves intact from a joint, therefore in such cases more general data has been used to describe behaviour.

Table 2: A summary of the features and functions of major nerve endings in the knee joint [8, 17, 18, 20-23, 29-37], based on the categories described by Freeman and Wyke [17]

Receptor	Features	Dimensions (μm)	Function
Ruffini ending	Globular/ovoid corpuscles. Branched, 'spray-like' nerve terminals. Linked in clusters of 3-6 corpuscles. Originate from Aβ fibres.	100x40 OR 50x500	Low threshold, slowly adapting mechanoreceptor. Act as stretch receptors. Neuronal firing frequency increases (once a threshold is reached) with stimulus, until reaching a plateau. Appear to display a preferred orientation, although not all authors agree.
Paciniform corpuscle	Laminated capsule, single nerve terminal. Linked in clusters of 2-3 corpuscles. Are cylindrical or conical corpuscles. Originate from Aβ fibres.	500x700 OR 280x120	Low threshold for neuronal firing, rapidly adapting mechanoreceptor. Respond to touch and low frequency vibrations. Pacinian corpuscle specific; act as compression higher frequency vibration receptors.
Golgi tendon organ	Fusiform corpuscles. Densely branching nerve terminals. Usually single, but known to be in clusters up to 3. Originate from Aβ fibres.	600x100	High threshold, very slowly adapting mechanoreceptor. Orientated parallel to collagenous fibres of tendon fibres, encode forces developed by contracting muscles.
Nociceptor	Free nerve endings (unmyelinated plexuses). Originate from Aδ or C fibres	<1.5	High threshold, slowly adapting, threshold reduced by inflammation. Pain receptor; respond to noxious mechanical, chemical, cooling or heating stimuli. Aδ fibres result in *pricking pain*, while C fibres result in *burning pain* .

Table 3: A summary of the distributions of nerve endings in the feline knee joint [17, 23, 28, 31, 36].

Receptor	Capsule	Ligaments	Fat Pads	Menisci	Cartilage
Ruffini ending	More numerous in superficial layers (especially on posterior aspect), dense in highly stressed regions. Rare in central layers.	Found in the extrinsic ligaments related to the capsule, located superficially where ligaments blend with the capsule. Never found on cruciate ligaments.	N/A	Occasionally present embedded in the attachment of meniscus to fibrous capsule.	N/A
Paciniform corpuscle	More numerous in deeper layers, especially at junction of internal layers with subsynovial tissue. Outnumber Ruffini endings in central layers. (Pacinian corpuscles very infrequent.)	N/A	Extra articular fat pad. Small clusters scattered infrequently along blood vessels. Confined to the peripheral.	N/A	N/A
Golgi tendon organ	N/A	Most prominent. Found at surface of each ligament, at one or the other end.	N/A	N/A	N/A
Nociceptor	Represented throughout capsule, with variable density. Most dense at posterior, and less dense at sides.	Structure with the most free nerve ending. Spread out over superficial surfaces. In cruciate ligaments, dense near bony attachments.	Distributed throughout entire fat pad. This plexus in the densest in the entire joint.	Confined to connective tissue of annular ligaments surrounding periphery of discs.	N/A

2.2.2.1 Ruffini ending

Due to its distinct structure, seen in Figure 4A (page 12), the Ruffini ending is one of the better recorded and most recognised mechanoreceptors in the knee joint. Similar endings have been found in the skin [8, 38]. Since skin is more accessible than soft tissues in the knee, it means that the behaviour of Ruffini endings in the skin is better understood than in the knee joint. The Ruffini ending is a stretch receptor, generating a neural response when the surrounding tissue experiences a tensile strain. This type of ending is found mostly in the deeper tissues of the knee joint, such as the capsule and ligaments [17, 23, 25], see Table 2. They are often described as proprioceptors as they are known to transmit a neural signal in response to a range of knee joint positions [39], not only at extreme angles. This is a slowly adapting mechanoreceptor, so responds to a maintained stimulus over a long period of time. Khalsa et al. [21] supports this by showing that, on application of stimulus the Ruffini ending will generate a train of action potentials until the stimulus is removed.

When a tensile load is applied to the tissue surrounding the Ruffini ending, a neural response is triggered. In general, the frequency of response increases linearly with stimulus strength before it reaches a peak frequency, where it will plateau. The response to tensile loading of Ruffini endings in the knee joint capsule specifically has been recorded by Grigg and Hoffman [22], Khalsa et al. [21] and Eklund and Skoglund [28]. All authors agree that Ruffini endings respond to stretching stimuli, and the frequency of this response increases as the stimulus strength increases. The experimental methods followed for each of these studies were generally similar, with two edges of the tissue clamped in place, and hooks inserted to the free edges. Either a fixed displacement is applied using a stepping motor, or a load is applied through a pulley system. Although the Ruffini ending responds to strains, studies generally report the stimuli in the form of applied loads instead of the resulting strains or displacements. Though the studies mentioned here are not recent, their methods are still used in modern studies of mechanical stimulation of sensory neurons [40, 41].

This type of mechanoreceptor has displayed asymmetric behaviour, where a stronger response is produced in one direction than the other [21, 22, 28, 31]. The direction of this stronger response appears to depend on the mechanoreceptor's location in the tissue. Khalsa et al. [21] noted that those classified as biased in the medial-lateral axis were found in the upper half of the capsule, while those classified as biased in the proximodistal axis

were found in the lower half. This could be related to the orientation of collagen fibres in the capsule [42], which lie parallel to each other and the medial-lateral axis in the upper margin, and are more randomly organised in the lower part.

There is high variability in the quantitative responses of Ruffini endings that have been reported, these could be due to both the variability in biological tissues, and differences in methodologies. In 1960, Eklund and Skoglund displayed a range of threshold values between 5 and 10kPa and maximum responses of up to 70imp/sec for loads of 25kPa [28]. Grigg followed a similar method, but takes advantage of motor actuators which may have led to more control over the loading process. Here the thresholds were reported to be higher, between 40kPa and 70kPa, and maximum recorded responses 45 impulses per second (imp/sec) and 40imp/sec for loads of around 117kPa and 206kPa respectively, depending on the direction of loading. In another set of experiments, with differences in the attachment of actuators to tissue, Khalsa et al. [21] reported responses to a smaller range of loads. The threshold here appears to be around 15kPa and the highest reported responses were 14 and 16imp/sec for stresses of 70kPa and 50kPa respectively.

Of these three sources of data, only Eklund and Skoglund loaded the Ruffini endings to saturation, where the same maximum response was recorded even after further increase of tension [30]. It is therefore difficult to make direct comparison between the different sets of experiments, as the endings have not been loaded over the same range of conditions. More detail would be required to further understand the meaning of these reports.

As already mentioned, Ruffini endings are also commonly found in skin [38, 43], where they are also described to be slowly adapting stretch-receptors. The responses of these have been recorded in a similar method to those in the feline knee joint capsule. Grigg [43] reported similar biased behaviour to tensile loading, with stronger responses being recorded in one direction than the other; the highest frequency 35imp/sec at 80kPa, followed by a drop to 20imp/sec at 100kPa, with a threshold of around 20kPa. Grigg [43] also reported the mechanical properties of the skin specimens. These are anisotropic, with the less stiff direction being the ‘preferred’ direction of the Ruffini ending. The neural responses are comparable to those recorded from the knee joint capsule, with any differences being potentially due to the tissue properties. It is, however, difficult to make direct comparisons with authors reporting different ranges of loading magnitudes, along with the high variability between each Ruffini ending.

The actual cause of the biased behaviour of the Ruffini ending has resulted in some conflicting opinions in authors. Some authors [21, 22, 31] state that the Ruffini ending itself has a preferred orientation, while Eklund and Skoglund [30] believe that this behaviour is in response to the properties of the soft tissue. This is supported by the relationship between location and biased direction reported by Khalsa et al. [21] and the symmetrical structure of the ending (see Figure 4A, page 12). Currently there is no description of either computational or mathematical model to represent the behaviour of the Ruffini ending.

2.2.2.2 Golgi Tendon Organ

The Golgi Tendon Organ (GTO) is another type of slowly adapting stretch receptor, however it differs from the Ruffini ending in both its structure, Figure 4B (page 12), and location in the knee, Table 3 (page 14). It is found mainly at the ends of ligaments and tendons around the knee joint [17, 23, 36]. The GTO is larger than the Ruffini ending, at 600x100μm, and the structure is a fusiform corpuscle [8, 17, 18, 23]. This ending is generally oriented parallel to the collagen fibres of the ligaments and tendons [44, 45], and it is believed that this can be used to describe how they respond to stretching stimulus [46]. Fukami and Wilkinson [47] reported that the mechanoreceptor responds to the strain experienced by the corpuscle itself, and that since they are parallel to collagen fibres they are encoding the strains in this direction.

This mechanoreceptor, as with the Ruffini ending, responds to tension and has a relatively high threshold [17]. Examples of these thresholds have been published by Fukami and Wilkinson [47], who conducted *in vitro* experiments on GTOs from cat tail muscles. In this case, the endings were isolated from surrounding tissue and their responses to ramp-and-hold stretching recorded. As with the Ruffini ending, the neuronal frequency increases with the magnitude of stretch. This relationship also begins linearly, and reduces as a maximum frequency, of around 10imp/s, is reached. The threshold values, however, were seen to vary greatly amongst the eleven GTOs tested; from 0.08-1.7mN. This linear response is the more popular description of the behaviour of GTOs [47-49].

In comparison, Schäfer et al. [44] describe the response of GTOs in feline tibial anterior muscle to ramp-and-hold stretching as power functions, and this is supported by Stephens et al. [50]. Schäfer et al. [44] also reported far higher responses to mechanical stimuli of up to 100 or 400imp/s to a 10N load, depending on the type. Two types of GTO are reported here; one GTO had an initial frequency (iGTO), which increased on application of a

stretching load, while the other had no initial frequency (niGTO) and on application of a load generated a far greater response than the iGTO. The threshold values of these two types also differed, with the iGTOs having lower thresholds of around 0.1-0.2N, and the niGTOs having thresholds closer to 0.5N. Neither of these thresholds match those reported by Fukami and Wilkinson [47].

Models for the GTO have been developed using a method that involves the use of a gain factor to obtain a frequency response from the local state. This method has been implemented by Mileusnic and Loeb in their model of the GTO [46, 51]. Though a frequency of the response is calculated, some information could be lost from not calculating the actual signal. This is a limited method, and it would be difficult to develop the research further to include transmission of the response, or effects of branching of a nerve.

2.2.2.3 Paciniform corpuscle

This type of mechanoreceptor has the most variation in naming and identification in the literature, with authors describing Vater-Pacini, Golgi-Mazzoni, Type II, and Pacinian corpuscles; summarised in Table 1 (page 11). The more general name of Paciniform corpuscle will be used for the rest of this project. Hogervorst and Brand [20] discuss this controversy in classification of mechanoreceptors, and suggest the receptors are not distinct types, but represent a continuum that is related to adaption to local conditions. This helps to explain the great variation that there appears to be in the reports of the Paciniform corpuscle type of mechanoreceptor. It is not only the naming of this nerve ending which results in confusion; the description of the occurrence of the Paciniform corpuscle in the knee joint is also widely varied. Gardner [52] states that there are no endings of this type in the knee joint, while Freeman and Wyke [17] suggest it is the most common of the mechanoreceptors found in the joint. Both Skoglund [23] and Boyd [25] describe this type of ending to appear infrequently in the knee joint. Pacinian corpuscles, a type of Paciniform corpuscles, are well reported to be present as vibration sensors in both the skin [8, 34] and cat mesentery [33, 53].

The Paciniform corpuscle is a rapidly adapting ending, so it only generates an action potential when a stimulus is applied, and sometimes when it is removed, suggesting it responds to changing stimuli, for example strain rates. It is a conical-shaped corpuscle, with the nerve ending itself at the centre and lamellated layers of membrane and fluid, Figure 4C (page 12). Although the response of Paciniform corpuscles in cat mesentery is

well documented [33, 53, 54], there is little data available describing the behaviour of these nerve endings at the knee joint. When found in the skin and mesentery, these endings respond to vibrations [8, 33, 54, 55]. Skoglund describes that a rapidly adapting response can be activated by a change in tension of the capsule [23]. More specifically, it can be activated by a rapid movement, without dependence on the initial position of the joint [23], and the rate of this movement must reach a minimum magnitude before the endings respond.

Bolanowski and Zwislocki [54] found that the behaviour of the Pacinian corpuscle depends on the combination of frequency and amplitude of the applied stimulus. It is pointed out that, irrespective of the required response, the U-shaped relationship between the stimulus frequency and amplitude is seen, as shown in Figure 5. For example, to produce 1 spike/second the optimal frequency is ~450Hz with amplitude of 0.0178μm [34].

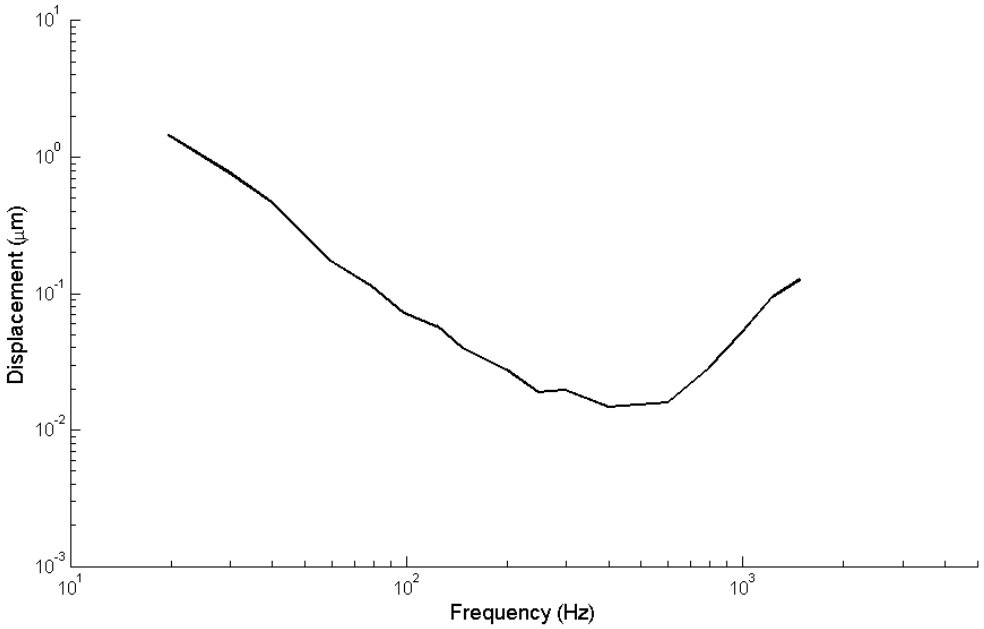

Figure 5: Response curves of Pacinian corpuscles to varying amplitude (displacement) and frequencies of vibrating stimulus, figure reproduced from Bolanowski and Zwislocki [54] with displacement plotted as μm rather than dB re. 1μm. The curve represents the combinations required to product one action potential per second, and the mean values from the original figure.

Loewenstein [33] applied mechanical pulses to different locations of a Paciniform corpuscle from a cat mesentery, and recorded the receptor potential in response to this. The change in this potential depended on stimulus strength and the magnitude of area the

stimulus was applied to. As the amplitude of vibrations (stimulus strength) increased, so did the receptor potential, until 50% stimulus strength was reached, at this point the response increase rate slowed, where 100% stimulus strength represents the strength required for receptor saturation. Loewenstein then developed a mathematical description of this behaviour;

$$V = k\frac{E \cdot bx}{1 + bx}\left(1 - e^{-t/R_t C}\right), \tag{1}$$

where V is the amplitude of the receptor potential; k is a constant that depends on the location of recording electrodes; E is the resting potential; $(1 + b)$ is the ratio between resting potential and the value to which the membrane potential drops due to a mechanical stimulus; R_1 is the membrane resistance; and C is the membrane capacitance. The variable x can either be the ratio of excited area to total excitable area of the receptor membrane, or the ratio of applied stimulus to maximum stimulus.

The Hodgkin-Huxley model [15] has been adapted for the modelling of a Paciniform corpuscle by Bell and Holmes [55, 56]. This involved mathematically modelling the structure of the corpuscle itself, including the movements of fluid between the lamellar layers, to determine the hoop strain when a compressive force is applied. The hoop strain was then included in an exponential function. The behaviour of this model is similar to that displayed by Paciniform corpuscles; it fires once on application of a stimulus, or twice if a larger amplitude is applied [55].

2.2.2.4 Nociceptor

Nociceptors are not restricted to only sensing mechanical stimuli, and are known to respond to other noxious stimuli such as thermal and chemical changes in their environment [8, 57, 58]. Since these endings respond to noxious stimuli, they have high thresholds, which can be around 0.2MPa [59, 60]. These are slowly adapting [37], so respond to maintained stimuli. Nociceptors are less involved in proprioception than the other nerve endings found in the knee joint, however they still play an important role in sensing potentially dangerous stimuli. If pain was not felt when a joint was reaching hyper-extension or flexion, for example, the tissues would very quickly be damaged, risking instability and loss of control.

Nociceptors are often named “free nerve endings”, due to their non-corpuscular, branched structure [17], see Figure 4D (page 12). There are two types of nociceptor, those that

branch from the unmyelinated group C nerve fibres, and those that branch from the thin, myelinated A-δ nerve fibres [37]. Depending on the type of fibre the endings have originated from, a different type of pain is experienced; a pricking pain is sensed by the endings arising from A-δ fibres, while a burning pain is sensed by those from C fibres [17, 37].

Most structures in the knee joint have nociceptors present, summarised in Table 3 (page 14), with varied densities. For example, an average of 15.4 endings were found in the posterior cruciate ligament, while an average of only 2.8 were found in the anterior cruciate ligament [61]. The fat pad apparatus, which acts as a shock absorber to protect the structures underneath [62, 63], has a particularly high density of nociceptors [17] while the cartilage has no innervation [64].

A model to represent nociceptors for thermal pain in the skin has been developed by Xu et al. [59], through adaptation of the Hodgkin-Huxley model. In their paper, a function was included to represent the flow of ions in response to a thermal stimulus, which was calculated through use of a thermo-mechanical model of skin. Since the authors used the Hodgkin-Huxley model as a basis of their model, a neural signal was calculated so that it could be directly compared with experimental data. Clearly, the Hodgkin-Huxley model is popular in the modelling of neural behaviour, so it has been described in detail and implemented in the following section.

2.3 The Hodgkin-Huxley model

Modelling can be used to further our understanding in the behaviour and underlying mechanisms that are involved in mechanoreceptors, when experimental tests may not be possible. Before the behaviour of individual nerve endings can be modelled, the general response of nerves must be understood. This field is mostly dominated by the Hodgkin-Huxley (H-H) model [15], a mathematical description of generation of an action potential across a nerve membrane. A series of papers in 1952 [15, 65-68] describe both experimental measurements and development of the model. These papers have been the basis of most neuron modelling to date [55, 59, 69]. Alternatives to the H-H model have been developed, including the parallel stochastic ion channel simulator (PSICS), developed by Robert Cannon [70]; a software that simulates the ion channels on extended cells. However, since the H-H model is widely accepted to be the best model to predict the generation of an action potential, this is the model that has been carried forward through

this project. This section describes, in detail, the development of the H-H model as presented in their papers in 1952 [15, 65-68], and then implements the original model using Matlab. Popular improvements to the run-time and stability of the model are then implemented [71-73], and their accuracy tested.

The first stage of development of the H-H model involved measurement of the flow of electric currents across a nerve's membrane. The giant axon of a squid was used for the experiments, to determine how the movement of ions, the membrane current, varies with the potential. The behaviour that was discovered formed the starting point of the Hodgkin-Huxley model. An electrical circuit model was proposed [74], with the total ionic current split into three terms; the current carried by both sodium and potassium ions and a leakage current from other ions. These currents can also be described in potential difference and ion conductance terms. Ion conductances change with the membrane potential due to the effect of the electric field on the distribution of molecules with a charge. There is also a time-dependence with the ion conductances, with the change in potassium ion conductance being slow, and sodium ion conductance adapting faster with a shorter timescale.

The model can be implemented using differential equation solvers, such as the ode15s solver in MATLAB. However due to the nonlinear nature of the model, it is slow to reach a solution robustly in its native state. This is a well-known problem in mathematics, and it has been shown that stabilising the model, through scaling and nondimensionalisation, can lead to more efficient and accurate computational results [73]. The accuracy of the original model is not lost through this process, and time to solution is greatly reduced. Some authors have also suggested that the model can be reduced, to further improve efficiency [71, 75]. The following sections of this chapter describe the paper series of Hodgkin and Huxley [65-68] in more detail and implement the model.

2.3.1 Experimental basis for model development

The first stage of development of this model involved the measurement of the flow of electric currents through a nerve's membrane. For this, the giant axon from a squid was used, of which the potential was maintained at uniform, controlled magnitudes. Silver wires, inserted down the centre of the axon, were used to measure both the membrane potential and apply current, see Figure 6. With these controlled conditions, it was possible to determine the membrane potential with which the nerve responded to specific applied currents.

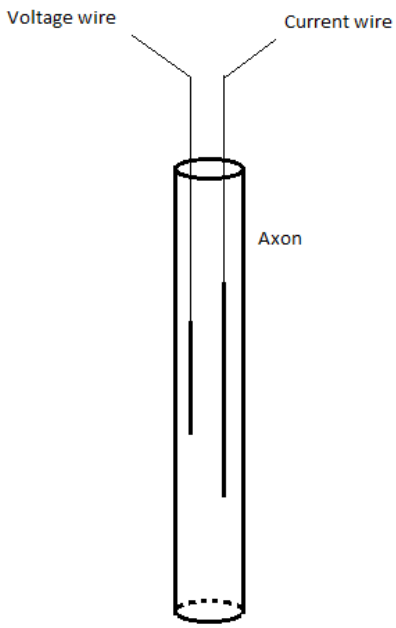

Figure 6: A schematic, simplified from the original paper of Hodgkin and Huxley [65], to show the experimental set-up of the nerve axon and measuring devices. Two internal silver wires used to measure the membrane potential and apply current to obtain the required change in membrane potential.

When a voltage step was applied through one of the internal wires, the membrane voltage was displaced causing depolarisation of the membrane; repolarisation of the membrane occurs when the membrane potential returns to its original value. Under these conditions the membrane current consisted of very brief currents at the beginning and end of the voltage step. When the axons were stimulated with these brief membrane current shocks an action potential was achieved, with an 'all-or-nothing' response at a threshold of around 15mV. Not only the action potential was measured, the ionic movement across the membrane could also be determined, i.e. the membrane current. Ions can move both into and out of the axon, through the membrane, resulting in 'inward currents' and 'outward currents'. This membrane current was found to vary with the membrane potential, with the response to small changes in the membrane potential being small outward currents and the response to larger changes being large inward currents. If the displacement in potential reached a particularly large value, the current would return to an outward direction. This continuous relation between ionic current and membrane potential came to be the starting point for the H-H model development.

The response of the membrane observed through their experiments led Hodgkin and Huxley to suggest that it could be described by the electrical circuit in Figure 7, where all I terms represent current density. The total ionic current has been split into three terms; the current carried by sodium and potassium ions (I_{Na} and I_K) and a 'leakage current' (I_l) from other ions such as chloride. Each component of the ionic current can also be described by the electrical potential difference and the electrical conductance. For example, the sodium current is equal to the difference between membrane potential (E) and the equilibrium potential for sodium (E_{Na}), multiplied by the sodium electrical conductance (g_{Na}). The equilibrium potential of an ion is the membrane potential at which the net movements of that particular ion from one side of the membrane to the other are zero, and electrical conductance is the inverse quantity of electrical resistance. This relationship can be extended to both the potassium and leakage currents. The experiments suggested that the ionic conductances, g_{Na} and g_K, are dependent on both time and membrane potential, while the ionic equilibrium potentials and membrane capacitance (C_M) can be treated as constant.

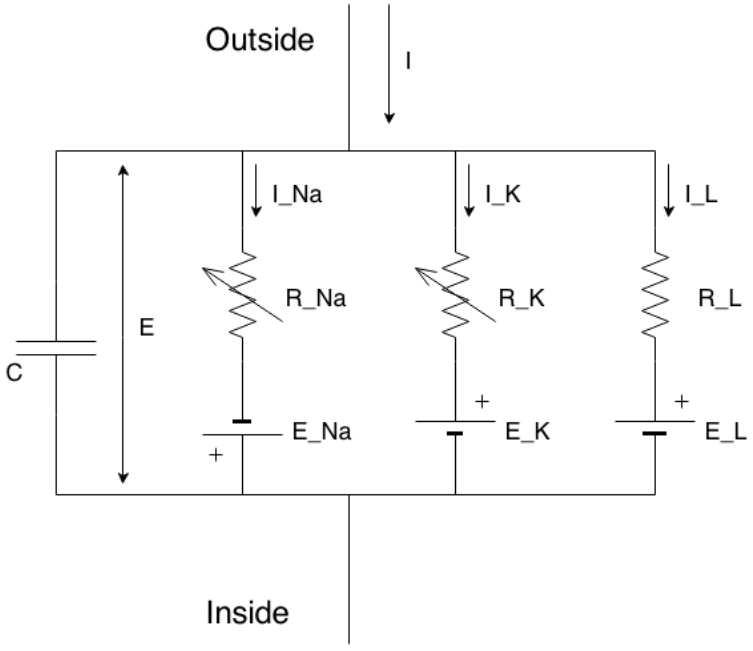

Figure 7: The electrical circuit representing membrane of a nerve, as suggested by Hodgkin & Huxley [15] in their figure 1. In this image, R_Na=$1/g_{Na}$, R_K=$1/g_K$ and R_L=$\frac{1}{g_l}$.

Since the ionic equilibrium potentials do not change, it is the ionic conductances that will change in response to changes in ionic current. Hodgkin and Huxley then continue to suggest that the ionic movement depends on the distribution of these charged particles; when the membrane potential is high, the flow of ions is initially high before a decline of this ionic movement.

2.3.2 Mathematical description of membrane current

With the behaviour of the ionic currents understood, it was now possible for Hodgkin and Huxley to begin building a mathematical description of membrane potential. This involved several steps, the first of which was to divide the membrane current into the ionic and capacity current terms:

$$I = C_M \frac{dV}{dt} + I_i, \tag{2}$$

where I is the total membrane current density, I_i is the ionic current density, V is the change in membrane potential from its resting value, C_M is the membrane capacity per unit area, and t is time. Equation (2) can be further divided to take the different ionic currents into account (equation (3)), and these ionic currents can be expressed in terms of their ionic conductances, shown in equations (4)-(6):

$$I_i = I_{Na} + I_K + I_l, \tag{3}$$

$$I_{Na} = g_{Na}(V - V_{Na}), \tag{4}$$

$$I_K = g_K(V - V_K), \tag{5}$$

$$I_l = g_l(V - V_l), \tag{6}$$

where V_{Na}, V_K, and V_l are the change in membrane potential due to sodium, potassium and leakage ions, respectively. The rates of change in potassium conductance occur far quicker with the sodium ions than potassium, as shown in Figure 8 and Figure 9. It is extremely difficult to calculate the time course of ionic conductances from first principles, so a more realistic approach was taken by finding the equations which best described the behaviour.

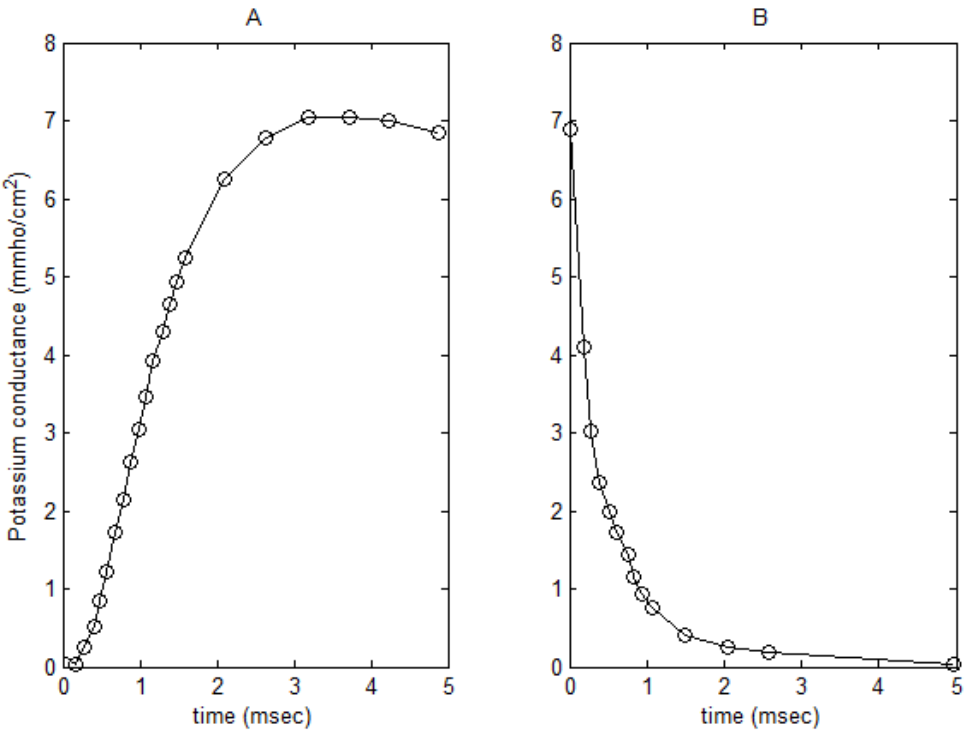

Figure 8: A plot to show the potassium conductance varying with time, adapted from Hodgkin & Huxley [15] figure 2. Part A is associated with depolarisation of the membrane, and part B is associated with repolarisation to the resting potential.

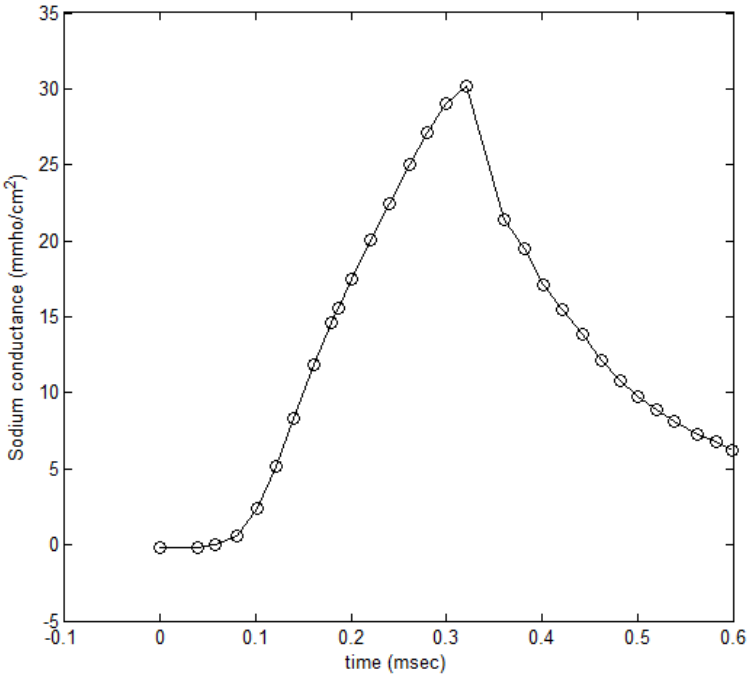

Figure 9: A plot to show the sodium conductance varying with time, adapted from Hodgkin & Huxley [67] figure 5. The membrane potential is reduced by 97.5mV at zero time, and restored to its resting potential at 0.32 msec.

As shown in Figure 8, the change in potassium ion conductance begins with a rapid increase, which is followed by a plateau when the membrane is depolarised, and an exponential fall when it is repolarised. This behaviour can be simplified by assuming that g_K is proportional to the fourth power of a variable which obeys a first-order equation. This can be relatively easily described using the following two assumptions:

$$g_K = \bar{g}_K n^4, \tag{7}$$

$$\frac{dn}{dt} = \alpha_n(1-n) - \beta_n n, \tag{8}$$

where $\bar{g}_K$ is a constant with dimensions of S/cm^2, α_n and β_n are rate constants with units $[time]^{-1}$ and n is a dimensionless variable which varies between 0 and 1 in the equilibrium. In equation (8), the n term represents the proportion of potassium ions that are at the inside of the membrane, while the $(1-n)$ term represents the proportion of potassium ions that are outside. This means that α_n describes the rate of transfer from outside to inside of the membrane and β_n describes the rate of transfer from inside to outside of the membrane. After applying boundary conditions to these equations, it is possible to fit the curves to the data by setting the following expressions:

$$\alpha_n = \alpha_{n0}(V + V_{n0}) / \left[exp\left(\frac{V+V_{n1}}{V_{n1}}\right) - 1\right], \tag{9}$$

$$\beta_n = \beta_{n0} exp\left(\frac{V}{V_{n2}}\right), \tag{10}$$

where $\alpha_{n0} = 0.01 ms^{-1} mV^{-1}$, $V_{n0} = V_{n1} = 10mV$, $\beta_{n0} = 0.125 ms^{-1}$, and $V_{n2} = 80mV$. Similar principles can be followed to describe the behaviour of sodium ion conductance over time in the form of equations, which is a far shorter timescale than that of the potassium ion conductance, see Figure 9. The route taken here assumes that the sodium conductance is determined by two variables, each of which obeys a first-order equation. These assumptions in mathematical form are:

$$g_{Na} = m^3 h \bar{g}_{Na}, \tag{11}$$

$$\frac{dm}{dt} = \alpha_m(1-m) - \beta_m m, \tag{12}$$

$$\frac{dh}{dt} = \alpha_h(1-h) - \beta_h h, \tag{13}$$

where $\bar{g}_{Na}$ is a constant, with unit S/cm^2 and the α's and β's are again rate constants, with unit $[time]^{-1}$ which are functions of V. The variable m represents the proportion of sodium ions inside the membrane which are activating the ion channels, and h represents the proportion of sodium ions outside of the membrane which are inactivating the ion channels. Again, applying boundary conditions to these equations and fitting them to data results in:

$$\alpha_m = \alpha_{m0}(V + V_{m0}) / \left[exp\left(\frac{V+Vm_0}{V_{m1}}\right) - 1\right], \tag{14}$$

$$\beta_m = \beta_{m0} exp\left(\frac{V}{V_{m2}}\right), \tag{15}$$

$$\alpha_h = \alpha_{h0} exp\left(\frac{V}{V_{h0}}\right), \tag{16}$$

$$\beta_h = 1 / \left[exp\left(\frac{V+V_{h1}}{V_{h2}}\right) + 1\right], \tag{17}$$

where $\alpha_{m0} = 0.1ms^{-1}mV^{-1}, V_{m0} = 25mV, V_{m1} = 10mV, \beta_{m0} = 4ms^{-1}, V_{m2} = 18mV,$ $\alpha_{h0} = 0.07ms^{-1}, V_{h0} = 20mV, V_{h1} = 30mV,$ and $V_{h2} = 10mV$.

2.3.3 Reconstruction of nerve behaviour

2.3.3.1 The original model

Substitution of the expressions for conductances into equation (2), page 21, results in:

$$I = C_M \frac{dV}{dt} + g_{Na} m^3 h(V - V_{Na}) + g_K n^4 (V - V_K) + g_l (V - V_l), \tag{18}$$

$$\frac{dm}{dt} = \alpha_m(1-m) - \beta_m m, \tag{19}$$

$$\frac{dh}{dt} = \alpha_h(1-h) - \beta_h h, \tag{20}$$

$$\frac{dn}{dt} = \alpha_n(1-n) - \beta_n n, \tag{21}$$

where parameter values and symbols are defined in the following table [15]. Equation (17) displays the behaviour seen in Figure 8 and Figure 9. Parameters m^3 and h obey a 1st

order equation, where *m* and *h* are dimensionless and represent proportions of sodium particles inside the membrane. The parameter n^4 obeys a separate 1st order equation, where *n* is also dimensionless and represents the proportion of potassium particles inside the membrane. Equations (19) and (20) represent the sodium ion parameters, and equation (21) represents the potassium ion parameters.

Parameter	Symbol	Value
Equilibrium potential for sodium ions	V_{Na}	$-115mV$
Equilibrium potential for potassium ions	V_K	$12mV$
Equilibrium potential for leak ion channels	V_l	$-10.613mV$
Sodium ion conductance	g_{Na}	$120\,mS/cm^2$
Potassium ion conductance	g_K	$36\,mS/cm^2$
Conductance of leak ion channels	g_l	$0.3\,mS/cm^2$
Initial value of α_m	α_{m0}	$0.1[time]^{-1}$
Initial value of β_m	β_{m0}	$4[time]^{-1}$
Initial value of α_n	α_{n0}	$0.01[time]^{-1}$
Initial value of β_n	β_{n0}	$0.125[time]^{-1}$
Initial value of α_h	α_{h0}	$0.07[time]^{-1}$
Initial value of β_h	β_{h0}	$1[time]^{-1}$
Membrane capacity per unit area	C	$1\,\mu F/cm^2$

Table 4: Parameter values for the Hodgkin-Huxley model, as defined in the original paper [15].

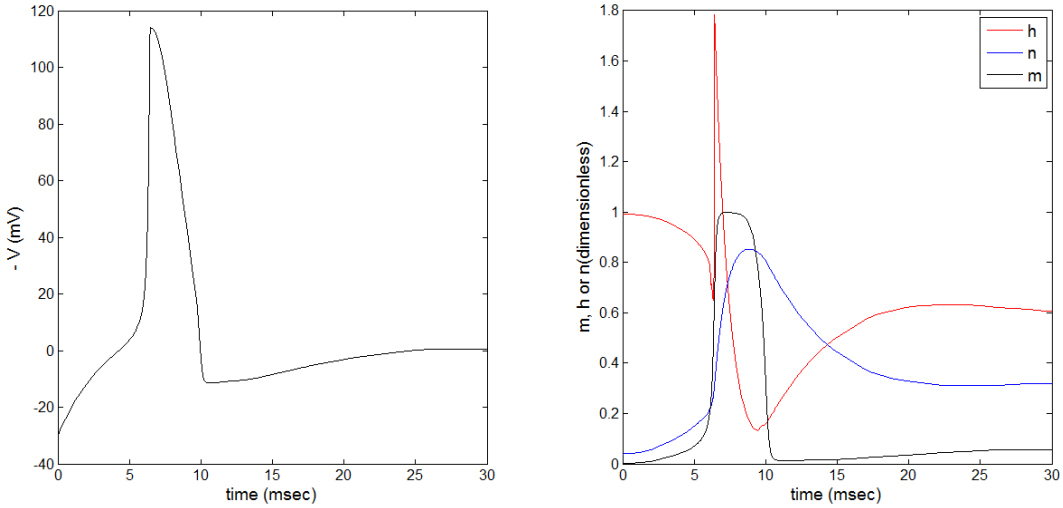

Figure 10: Response of the H-H model. On left: membrane potential behaviour after an initial displacement in potential of 30mV. On right: behaviour of the dimensionless parameters m, n and h under the same membrane potential displacement.

The four differential equations described in equations (18) to (21) can be implemented with the use of the ode15s differential equations solver in MATLAB. If an initial membrane potential is applied ($V = 30mV$) an action potential is generated; shown in the left plot in Figure 10. The right plot in Figure 10 shows the behaviour of each of the ionic conductance variables, m, n and h.

When the model is adapted to take a stepped change in membrane potential, as a stimulus, the peak seen in Figure 10 is repeated until the applied stimulus is removed. An example of this response is shown in Figure 11, where the red line represents the stimulus and the blue line represents the response. The equation used for the stimulus, in this case, is;

$$stim = a[\tanh(bt - bc_1)) - \tanh(bt - bc_2))], \qquad (22)$$

Where $a = 10mV/sec$, $b = 5$, t is the time in *sec,* and c_1, c_2 are the times at which the stimulus is applied and removed, respectively.

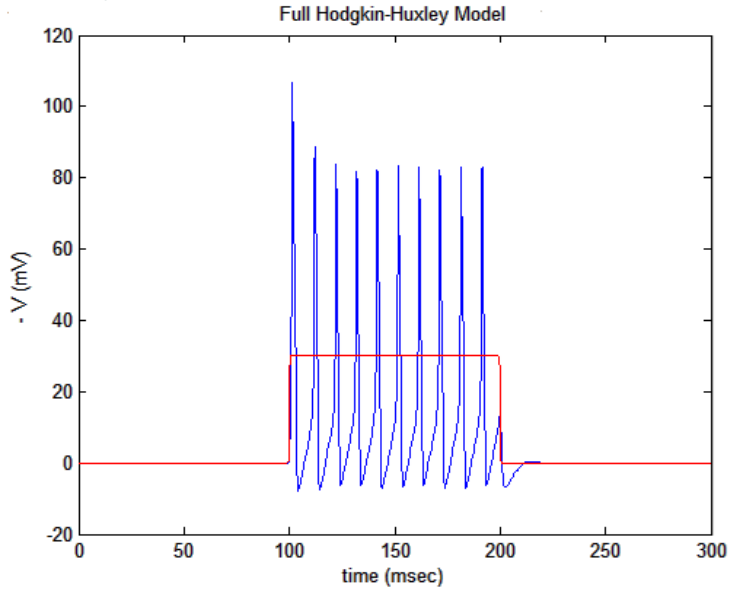

Figure 11: Response of the H-H model to a stepped displacement in membrane potential of -30mV over a time period of 100 milliseconds. The red line represents the stimulus, and the blue line represents the response.

The frequency of the response from the H-H model varies with the stimulus strength; this can be seen in Figure 12.

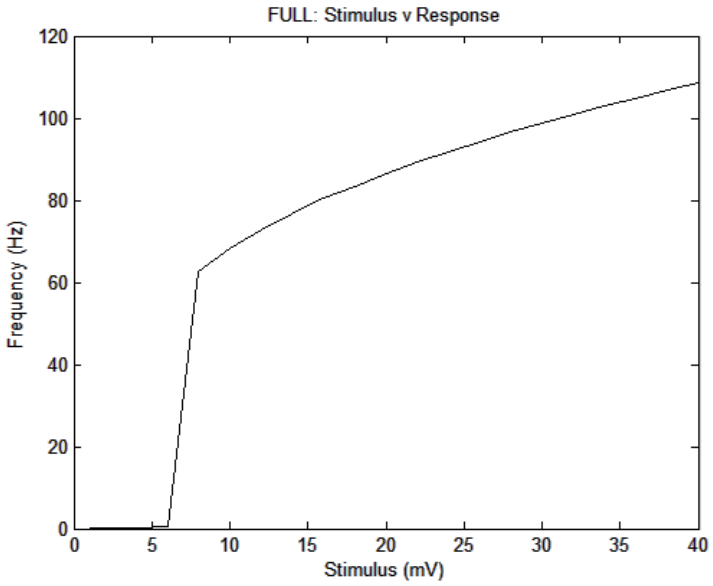

Figure 12: Frequency response of the H-H model, varying with the magnitude of membrane potential displacement.

These plots confirm the implementation of H-H model to be correct [15], and that this behaviour is typical of that seen in nerve endings [8]. Although these plots support the behaviour of the H-H model, the time to solution is large, taking 7.7 seconds[3] to generate the plot in Figure 11. This is for a timescale of only 300mseconds, with the stimulus present for 100mseconds, which is not representative of the activities which will be required of this model. Eventually, the model is used to represent multiple nerve endings, running for longer time periods, which would be likely to result in problems if this full H-H model were to be used.

2.3.3.2 Nondimensionalisation

As mentioned in the previous section, the original H-H model is, although accurate, slow to reach a solution because of nonlinearities and floating point errors. This is not an ideal situation if the model is to be used for larger stimuli from simulations that run for similar runtimes (300mseconds), for 10s to 100s of mechanoreceptors. It could, therefore, be beneficial to attempt to stabilise the numerical model, through scaling and nondimensionalisation [73, 76]. Since the fundamental units of the equations are those of membrane potential (V) and time (t), these are the parameters that will be scaled. This scaling is possible through introducing parameters with inverse units such as $[V]$ and $[t]$, with units mV^{-1} and s^{-1} respectively. This results in $V = [V]\bar{V}$ and $t = [t]\tau$, where $\bar{V}$ and τ are the dimensionless terms representing the membrane potential and time respectively.

After substituting these definitions into the original H-H model, the nondimensional equations are:

$$\frac{d\bar{V}}{d\tau} = \frac{[t]}{C}\left[-g_{Na}m^3h(\bar{V}-\bar{V}_{Na}) - g_K n^4(\bar{V}-\bar{V}_K) - g_l(\bar{V}-\bar{V}_l) + \frac{I_a}{[V]}\right], \qquad (23)$$

$$\frac{dm}{d\tau} = \alpha_{m0}[t][V]\left[\frac{\bar{V}+\bar{V}_{m0}}{exp\left(\frac{[V]}{10}(\bar{V}+\bar{V}_{m0})\right)}\right](1-m) - \beta_{m0}[t]exp\left(\frac{[V]\bar{V}}{18}\right)m, \qquad (24)$$

[3] Simulations carried out on a University of Southampton research workstation. Specifications of this workstation can be found at http://www.soton.ac.uk/isolutions/computing/staff/uderange/researchworkstationsys2.html [accessed 16/06/2011]

$$\frac{dh}{d\tau} = \alpha_{h0}[t]exp\left(\frac{[V]\bar{V}}{20}\right)(1-h) - \left[\frac{\beta_{h0}[t]h}{exp\left(\frac{[V]}{10}(\bar{V}+\bar{V}_{h0})\right)+1}\right], \quad (25)$$

$$\frac{dn}{d\tau} = \alpha_{n0}[t][V]\left[\frac{\bar{V}+\bar{V}_{n0}}{exp\left(\frac{[V]}{10}(\bar{V}+\bar{V}_{n0})\right)-1}\right](1-n) - \beta_{n0}[t]exp\left(\frac{[V]\bar{V}}{80}\right)n, \quad (26)$$

where $\bar{V}_{Na} = \frac{V_{Na}}{[V]}$, $\bar{V}_K = \frac{V_K}{[V]}$ and $\bar{V}_l = \frac{V_l}{[V]}$

The parameter values that have been used here are the same as those used in the original model with two additions:

$$[t] = 10\text{s}^{-1},$$

$$[V] = 100\text{mV}^{-1},$$

The initial values for m, n and h were calculated using the expressions:

$$m_0 = \frac{\alpha_{m1}}{\alpha_{m1}+\beta_{m1}}, \quad (27)$$

$$n_0 = \frac{\alpha_{n1}}{\alpha_{n1}+\beta_{n1}}, \quad (28)$$

$$\text{and } h_0 = \frac{\alpha_{h1}}{\alpha_{h1}+\beta_{h1}}. \quad (29)$$

When this model is implemented, the efficiency is greatly increased, while maintaining the accuracy of the model. For example, the time to produce the plot in Figure 11 took only 0.06 seconds, compared with the original H-H model's time of 7.7 seconds. This impressive improvement in efficiency implies that the model has been successfully stabilised.

2.3.3.3 Reduction

On observing equations (23) to (26) and the behaviour of *m* in Figure 10, it is appears possible to reduce the number of variables in the model in a similar method followed by FitzHugh [71, 73]. When the initial α and β parameters are compared from Table 4, page 29, it can be seen that those associated with the parameter *m* are far higher than those of *n* and *h*. These parameters can be grouped with the nondimensionalisation scaling terms in

equation (24) to obtain the new scaling parameter term of $\varepsilon_m = \frac{1}{\alpha_{m0}[t][V]}$ which is of the scale 10^{-2}. Applying this scaling to equation (24) results in $dm/d\tau \approx 0$, and;

$$m = \left[\frac{\bar{V}+\bar{V}_0}{exp\left(\frac{[V]}{10}(\bar{V}+\bar{V}_0)\right)-1}\right] \Bigg/ \left[\frac{\bar{V}+\bar{V}_0}{exp\left(\frac{[V]}{10}(\bar{V}+\bar{V}_0)\right)-1} + \frac{\bar{\beta}}{\bar{\alpha}} exp\left(\frac{[V]\bar{V}}{18}\right)\right], \tag{30}$$

where $\bar{\alpha} = \alpha_{m0}[t][V]$ and $\bar{\beta} = \beta_{m0}[t]$, resulting in just three equations describing the model;

$$\frac{d\bar{V}}{d\tau} = \frac{-g_{Na}m^3h[t]}{C}(\bar{V}-\bar{V}_{Na}) - \frac{g_K n^4[t]}{C}(\bar{V}-\bar{V}_K) - \frac{g_l[t]}{C}(\bar{V}-\bar{V}_l) + \frac{I_a[t]}{C[V]}, \tag{31}$$

$$\frac{dh}{d\tau} = \alpha_{h0}[t]exp\left(\frac{[V]\bar{V}}{20}\right)(1-h) - \frac{\beta_{h0}[t]h}{\left[exp\left(\frac{[V]}{10}(\bar{V}+\bar{V}_0)\right)+1\right]}, \tag{32}$$

$$\frac{dn}{d\tau} = \alpha_{n0}[t][V]\left[\frac{\bar{V}+\bar{V}_0}{exp\left(\frac{[V]}{10}(\bar{V}+\bar{V}_0)\right)-1}\right](1-n) - \beta_{n0}[t]exp\left(\frac{[V]\bar{V}}{80}\right)n. \tag{33}$$

Common sense suggests that with one less differential equation involved in the model, the time to solution should reduce further. However this is not the case, with the time to solution actually being higher than that of the full, dimensionless model; for example the time taken to generate a response to a stepped stimulus, as in Figure 11, with this reduced model is 0.1 seconds. Unfortunately it is not only the efficiency that is reduced; the accuracy of the model is also lost. This can be seen in Figure 13, where the blue line represents the response of the reduced model, the red line represents the response of the nondimensional model, and the black line represents the response of the original model. The loss of accuracy that is displayed by the reduced model could be due to some of the more specific aspects of the system being lost through the reduction process. Figure 14 shows that the behaviour of *m* in the reduced model does not match that of the full H-H model. The reduction process could have resulted in loss of information in the behaviour of *m* that would have otherwise been captured by the original model. Simplification of the

behaviour of *m* results in its peak occurring earlier than in the full model; this could be the main cause of the poor accuracy seen in Figure 13.

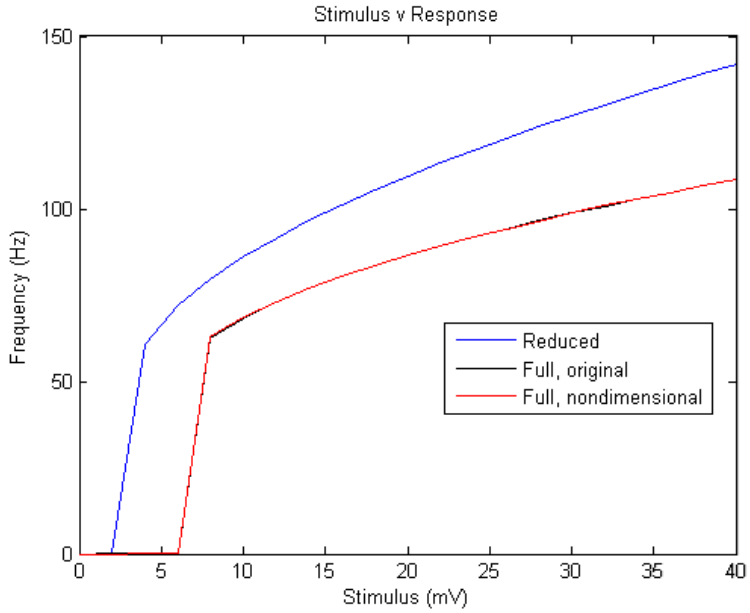

Figure 13: Frequency response to varied stimulus strength; the red line represents the reduced model, the blue line represents the full nondimensional and the black line represents the original model.

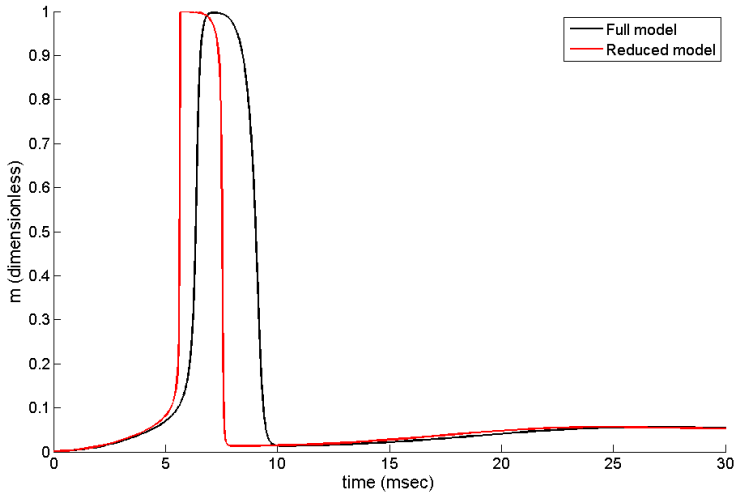

Figure 14: Behaviour of the dimensionless variable *m* during generation of action potential. Black line represents behaviour of the full model and red line represents behaviour of the reduced model.

Though the reduced model can be used to help in the understanding of this type of system, due to its poorer accuracy it has not been used further in this project. Since the non-dimensional model retained accuracy (mean squared error of prediction (MSEP)=0.019) while improving run time, this is the model that has been used for the rest of this project.

2.4 Sensory Neuron Models

The rest of this chapter describes the development and verification of models that will represent the behaviour of mechanoreceptors at the knee joint, through adaption of the H-H model. A calibration and verification process is possible with the use of recordings recorded from Viscerofugal neurons during tensile loading of gut tissue. Viscerofugal neurons are found in the guinea pig colon, and are reported as stretch-sensing mechanoreceptors which respond more strongly to stretching in one direction than the other. Their behaviour appears to be similar to that of the Ruffini ending, so if the model can be validated using data from the Viscerofugal model, it can be assumed that it is applicable to the Ruffini ending.

2.4.1 Model Development

The model was developed in two parts; a finite element model that represents the mechanics of soft tissue deformation, and a neural model based on the H-H model. The first part has been built using Comsol Multiphysics 4.3a, and is a plane stress structural model of a small piece of tissue. Two edges are fixed, and loads are applied to the remaining two edges, as illustrated in Figure 15 below. Local mechanical states have then been obtained at the location of a mechanoreceptor. This model is easily adapted for the relevant tissue dimensions and properties.

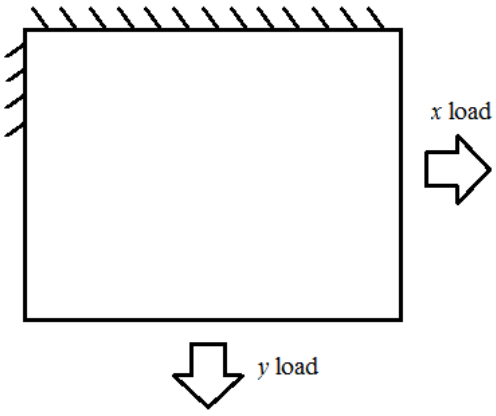

Figure 15: Diagram of the boundary conditions applied to the finite element model in Comsol, where available the boundary conditions match those applied during experimental studies.

The nondimensionalised Hodgkin-Huxley model can be adapted such that an action potential response is achieved from a stimulus [55, 59]. A new parameter is introduced to the voltage equation of the model, *U*, which represents the change in current density at the membrane as shown in equation (34). This adaptation is inspired by the mechanical portion of the model developed by Xu et al. [59]. In their study, an extra current density term is applied to the model, *U*, which has a linear relationship with the mechanical stimulus experienced by the soft tissue, γ.

$$\frac{d\bar{V}}{d\tau} = \frac{[t]}{C}\left[-g_{Na}m^3h(\bar{V} - \bar{V}_{Na}) - g_K n^4(\bar{V} - \bar{V}_K) - g_l(\bar{V} - \bar{V}_l) + \frac{U}{[V]}\right]. \qquad (34)$$

The relationship between mechanical stimulus and change in current density is assumed to be linear (equation (35)), continuing with the assumption made by Xu et al. [59]. There is no literature suggesting that the relationship between changes in current density and mechanical stimulus would not be linear, so this has assumption has been kept the same. For our model, the mechanical stimulus is assumed to be hydrostatic strain, though later in this chapter, the model's sensitivity to the type of stimulus input is tested;

$$U = c\gamma, \qquad (35)$$

where γ is the hydrostatic strain, and *c* is a coupling factor which can be optimised to best fit experimental data. Since this model has been developed for use with any slowly adapting mechanoreceptor, and there is little data available on those at the knee joint, model validation will be carried out using data from the Viscerofugal neurons. Figure 16 summarises this model.

Figure 16: The developed model, consisting of a set of mathematical equations describing the generation of action potential across a nerve membrane, based on the Hodgkin-Huxley model, and the coupling stage between the H-H model and mechanical model. The circuit diagram represents the four ionic movements identified on the left of the image. C represents the membrane capacitance, V_{Na} V_{Na}, V_K and V_l represent the equilibrium potentials (mV) for sodium, potassium and leak ion channels, α and β are rate constants ($[msec]^{-1}$). In the circuit diagram, R_{Na}, $R_K R_K$ and R_l represent the resistances of the ion channels, with $R_{Na} = 1/g_{Na}$ $R_{Na} = 1/g_{Na}$, $R_K = 1/g_K$ and $R_l = 1/g_l$. Arrows to the left of the circuit indicate the movement of ions through the membrane, which is then represented by the circuit.

Hodgkin-Huxley

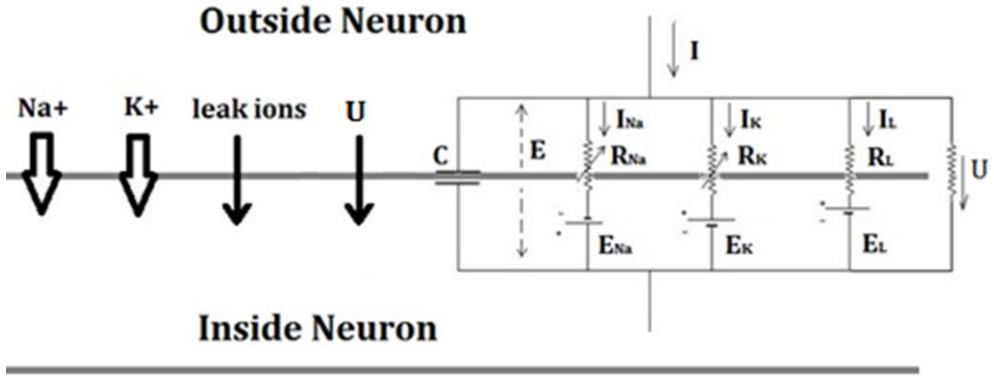

Voltage Equation:

$$\frac{dV}{dt} = \frac{1}{C}\left[-g_{Na}m^3h\left(V - V_{Na}\right) - g_k n^4\left(V - V_K\right) - g_l\left(V - V_l\right) + U\right], \quad (1)$$

Sodium Ion Equations:

$$\frac{dm}{dt} = \alpha_{m0}\left[\frac{V - V_{m0}}{\exp\left(\frac{1}{10}\left(V + V_{m0}\right)\right)}\right]\left(1 - m\right) - \beta_{m0}\exp\left(\frac{V}{18}\right)m, \quad (2)$$

$$\frac{dh}{dt} = \alpha_{h0}\exp\left(\frac{V}{20}\right)\left(1 - h\right) - \left[\frac{\beta_{h0}h}{\exp\left(\frac{1}{10}\left(V + V_{h0}\right)\right) + 1}\right], \quad (3)$$

Potassium Ion Equation:

$$\frac{dn}{dt} = \alpha_{n0}\left[\frac{V - V_{n0}}{\exp\left(\frac{1}{10}\left(V + V_{n0}\right)\right)}\right]\left(1 - n\right) - \beta_{n0}\exp\left(\frac{V}{80}\right)n. \quad (4)$$

$$U = \gamma c. \quad (5)$$

2.4.2 Model validation

Viscerofugal neurons are a unique population of mechanosensory interneurons present in the gastrointestinal wall that fire directly to mechanical stimuli. All studies to date have compared neural firing responses to the global strain or applied loads. These have indicated the adequate stimulus for their activation, but not how local mechanical states relate to firing. It is possible that digital image correlation (DIC) can be used to calculate the local strains experienced by viscerofugal neuron bodies within the soft gut wall. In vitro physiological mapping and neuroanatomical tracing techniques [77] have recently been adapted to localise viscerofugal neurons in the gut wall [41]. These techniques have been combined with the DIC method for the first time. Six datasets were collected, comprising of the neural responses to a range of tensile loading conditions.

Once the relationship between local strains and neural response has been identified, it was possible to calibrate and validate the computational model described previously to represent this behaviour. The basis of this model is the Hodgkin-Huxley mathematical description of an action potential. This has been adapted to represent sensory neuron behaviour, such that action potentials are generated in response to a mechanical stimulus.

2.4.2.1 Methodology

The experimental recordings were taken by Timothy Hibberd, Flinders University in Adelaide. Paralysed flat-sheets of guinea-pig colon were loaded uni- and bi-axially, while video recording. Viscerofugal neurons were localised and recorded extracellularly from colonic nerves [41]. Carbon graphite markers were applied to the tissue surface, and viscerofugal cell bodies identified for subsequent image analysis. The markers were applied using a 100mg (1mN) von Frey hair tip covered in an evaporated sucrose solution [41], and were mostly located around the cell body. There were around 30 markers applied to each tissue sample. Circumferential and longitudinal displacements were recorded for future global strain calculation. Figure 17 shows an example of the tissue surface. Hooks were attached to the free edges of the samples, to allow the loading to be applied. The experiments were force controlled, with a pulley system attached to the hooks, to which weights were applied; 1g, 3g, 6g, 9g and 12g.

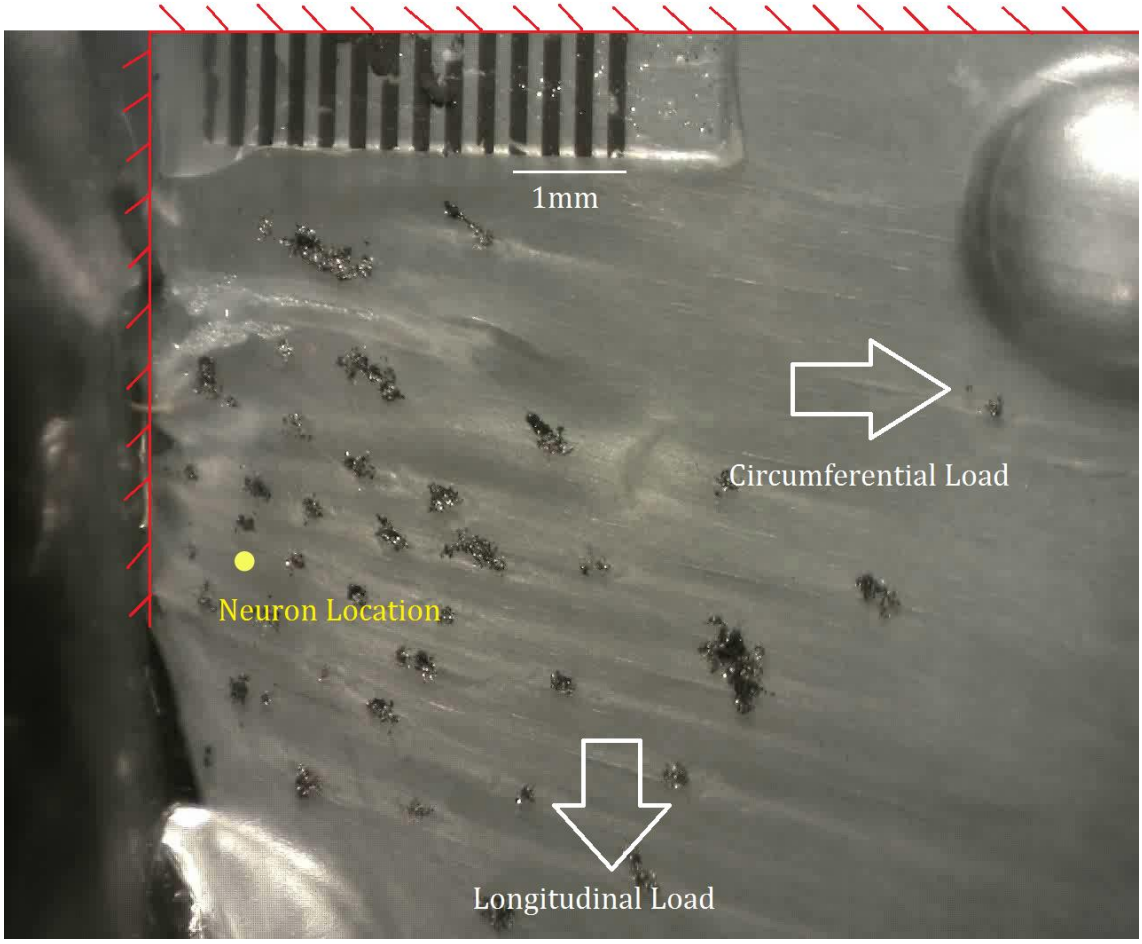

Figure 17: Example image from experimental loading viscerofugal neurons. Red lines at the top and left of image represent the fixed edges of the tissue, the remaining edges are free, arrows represent the directions of applied loads, and yellow dot represents the estimated neuron location.

In materials science, DIC is a valuable tool for determining the deformation of materials under applied loads. DIC uses tracking and image registration techniques for measurements of changes between digital images. Cross-correlation is used to track markers in a set of digital images, using pixel intensity values to identify different regions of an image. Due to the nature of this cross-correlation, contrast is required in the images to allow distinction of regions. Since soft tissue is generally lacking in contrast, numerous graphite markers were applied to the tissue surface.

Several DIC specific software exist which are optimised and calibrated to accurately track displacement. Generally, these have been developed for materials with high stiffness values, thus will only track small displacements. They are also often calibrated with specific cameras and for speckled surfaces. For these reasons, they are not ideal for this

study. A DIC script[4] [78], developed for use with MATLAB, is more generalised and has now been adapted by the authors to allow for both the uniquely placed markers, and larger displacement which is displayed by soft tissues. Once the DIC process has completed, the local strains in both circumferential and longitudinal directions can be calculated.

2.4.2.2 Experimental Results

2.4.2.2.1 Global Strains

Using the recorded displacement of sample edges, the global strains experienced by the soft tissues can be calculated as;

$$\varepsilon_{circ} = \frac{\Delta l_{circ}}{l_{circ}}, \tag{36}$$

$$\varepsilon_{long} = \frac{\Delta l_{long}}{l_{long}}, \tag{37}$$

where ε_{circ} and ε_{long} are the circumferential and longitudinal strains respectively, Δl_{circ} and Δl_{long} are the displacements, l_{circ} and l_{long} are the resting lengths. Figure 18 shows an example of the global displacements, the resultant global strains and instantaneous frequency, against time for a circumferential load of 6g. The instantaneous frequency is the reciprocal of the interval between impulses.

[4] Script by Chris Eberl, available at https://www.mathworks.co.uk/matlabcentral/fileexchange/12413-digital-image-correlation-and-tracking [accessed 15/09/2013].

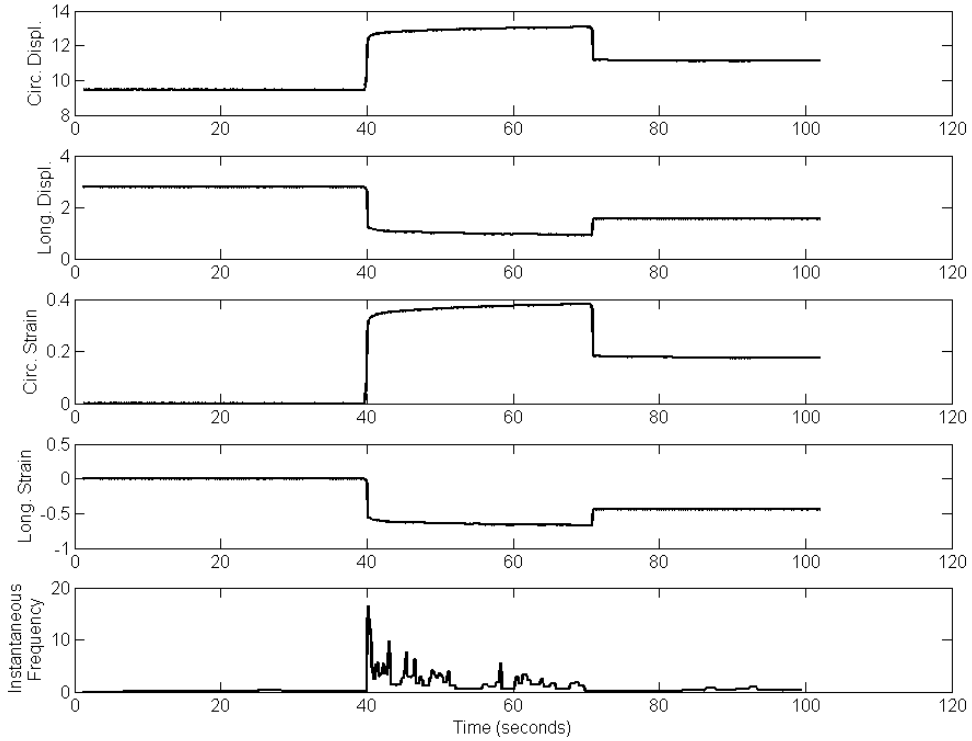

Figure 18: The displacement and global strain of tissue under 6g circumferential load, and associated instantaneous frequency response for the dataset 20121212.

The plots in Figure 18 show a negative displacement in the longitudinal direction of around 2mm. This is likely to be the Poisson's ratio effect of the tissue, which is calculated to be around 0.4; the Poisson's ratios of each sample are summarised in Table 6, page 45. Figure 19 below shows the global circumferential and longitudinal strains plotted against the recorded mean neural frequencies, which are calculated using the equation;

$$\mathrm{F_{mean}} = \frac{\sum_{n}^{i=0} \mathrm{AP}}{(\mathrm{tn})}, \tag{38}$$

where n is the number of frames, in this case $\mathrm{n} = 100$, AP is the number of action potentials recorded, and t is the time per frame, in this case $\mathrm{t} = 0.04$. The strains plotted are those experienced during both uniaxial and biaxial loading of the tissue samples. The curve fitting tool, cftool, in MATLAB is used to fit curves to the data in Figure 19. Exponential curves are used rather than linear or quadratic, as they are most likely to allow for the threshold behaviour that nerve endings exhibit. A better fit is achieved for the circumferential strains than the longitudinal strains, with higher R^2 values for these strains; as summarised in Table 5, page 44.

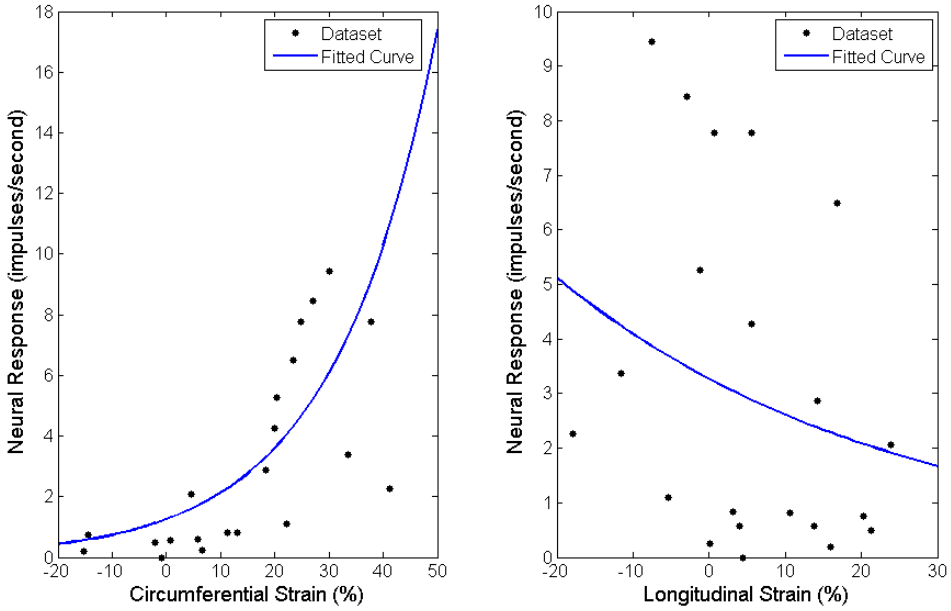

Figure 19: Left plot shows circumferential global strains (x) against mean neural frequency (y), and the right plot shows the longitudinal global strains (x) against mean neural frequency (y) for one of the datasets. Circumferential $R^2 = 0.484$, longitudinal $R^2 = 0.082$.

2.4.2.2.2 Local Strains

During the loading of the tissue samples, the displacement experienced by the Viscerofugal neuron is unlikely to be as great as the edge displacement recorded, as the neurons were generally located near the fixed edge of the tissue. DIC is used to track the displacement of markers on the soft tissue during loading, allowing the strains at the location of the neuron, the local strains, to be calculated. The local strains calculated from DIC are lower than the global strains, and give a stronger correlation with mean neural response, as shown in Figure 20 below. As with the global strains, exponential curves have been fitted to the data, and better fits were achieved for the circumferential strains than the longitudinal strains. This suggests that the Viscerofugal neurons still have directional behaviour locally. Table 5 compares the R-squared values of local and global circumferential strains. The R-squared values were calculated using the curve fitting tool in MATLAB, fitting an exponential curve to the data robustly.

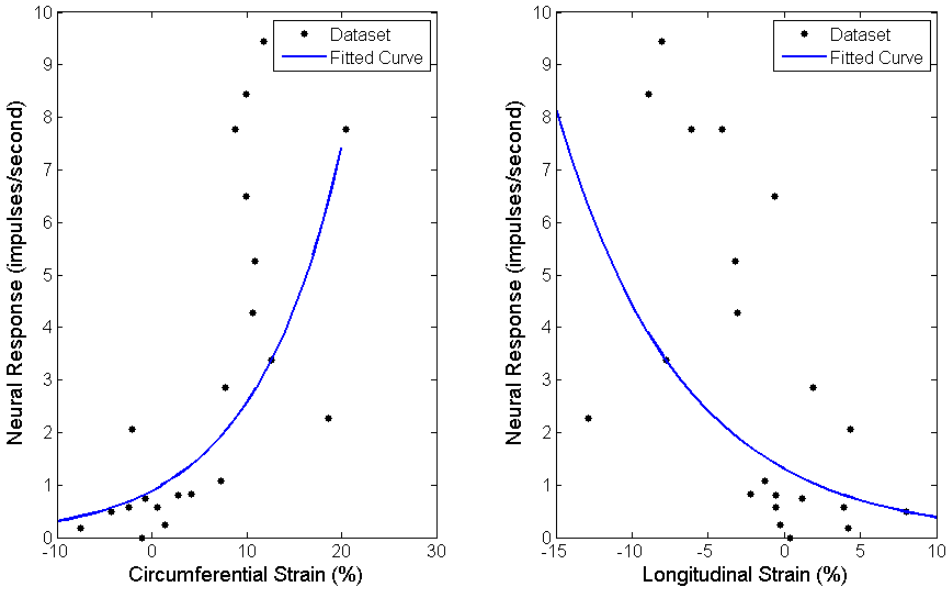

Figure 20: Left plot shows the circumferential local strains (x) against mean neural frequency (y), and the right plot shows the longitudinal local strains (x) against mean neural frequency (y) for the same dataset as shown in figure 2, for consistency. Circumferential $R^2 = 0.9028$, longitudinal $R^2 = 0.088$.

Dataset	Local circumferential strains (R-squared values)	Global circumferential strains (R-squared values)
1	0.7713	0.1358
2	0.8099	0.4787
3	0.9028	0.484
4	0.7902	0.431
5	0.0125	0.01698
6	0.3229	0.3411

Table 5: R-squared values of both global and local circumferential strains against mean neural response, when exponential curves fitted to data.

2.4.2.3 Computational Model

The model is built in two parts, as described previously, to replicate the experimental results. Six unique finite element models were developed in COMSOL 4.3a to represent the six different samples used experimentally, using their resting dimensions. The Young's moduli were calculated from the applied loads and resulting global strains, by determining the gradient of the linear portion of the stress-strain curve for each sample. Poisson's ratios were calculated from the resultant displacement of the samples during maximum circumferential uniaxial loading, and shear moduli calculated as $G = {}^{E}/_{2(1+\nu)}$, where G is the shear modulus, E is the Young's modulus, and ν is Poisson's ratio. Table 6 summarises the Young's moduli and Poisson's ratios used for each model. Unfortunately, since there were no repeated tests, it was not possible to check how robust these properties were. However the global displacements were measured to a high accuracy with an ionic transducer, so great variation within the same sample would not be expected.

Dataset	Circumferential Young's Modulus (kPa)	Longitudinal Young's Modulus (kPa)	Poisson's Ratio
1	51.98	107.34	0.25
2	18.09	49.54	0.44
3	25.46	58.96	0.39
4	19.97	155.24	0.36
5	16.87	105.16	0.34
6	30.09	101.85	0.42

Table 6: Material properties of each of the six datasets, determined experimentally.

The same loading conditions from the experimental methodology were applied to the finite element models, for more accuracy. Local mechanical states can be estimated and compared with the local strains from the DIC. Figure 21 shows the local strains from the DIC plotted against the local strains obtained from the computational model, for this model the root mean squared error of prediction (RMSEP) is 0.064.

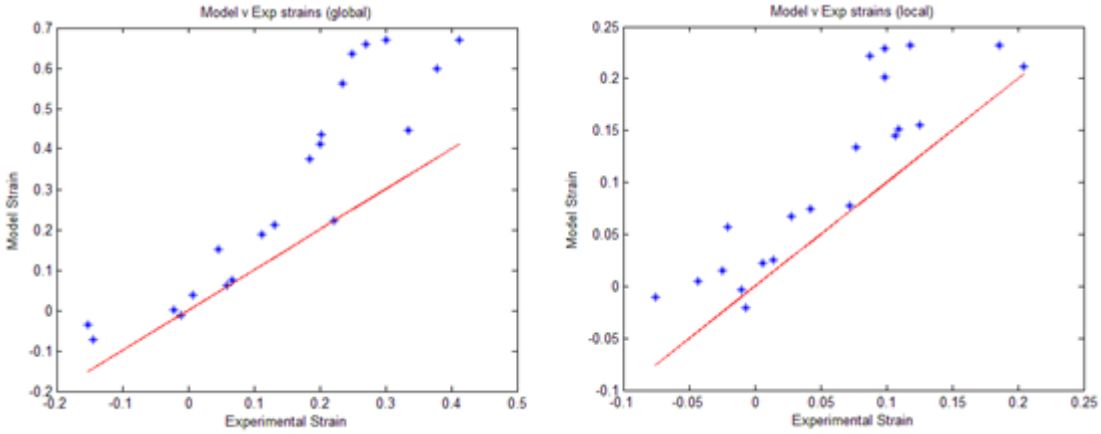

Figure 21: Plots of model predictions against experimental strains, both global (left plot) and local (right plot) strains. The red lines represent a perfect fit.

The value of the coupling factor of the neural model (Figure 16) is determined through optimisation of the model against the experimental data, using the *fminsearch* in MATLAB. The function is used to find the coupling factor that generates the lowest sum of mean squared error of prediction (MSEP) across the datasets. Five of the six datasets are used for the optimisation process, and the final one is used for validation of the final model. This was carried out six times, so that there was no bias in the model training/validation process.

2.4.2.4 Results

After optimisation to the experimental data over 5 of the datasets, the model can be validated using the remaining dataset. Figure 22 shows the comparison between predicted frequency and experimental frequency for the results of one of the six optimisation processes. The mean and confidence intervals for the thresholds of predictions and experimental datasets are also plotted in Figure 22, showing a clear overlap. The range of the thresholds for the experimental datasets is larger than the predictions, which is most likely to be due to the highly variable nature of biological systems. In this plot, the predicted neural responses are to the same load experienced by the tissue sample during experiment. The behaviour of the predicted response appears to be stepped; this could be due the shape of the H-H curve at the lower frequencies (Figure 12, page 31).

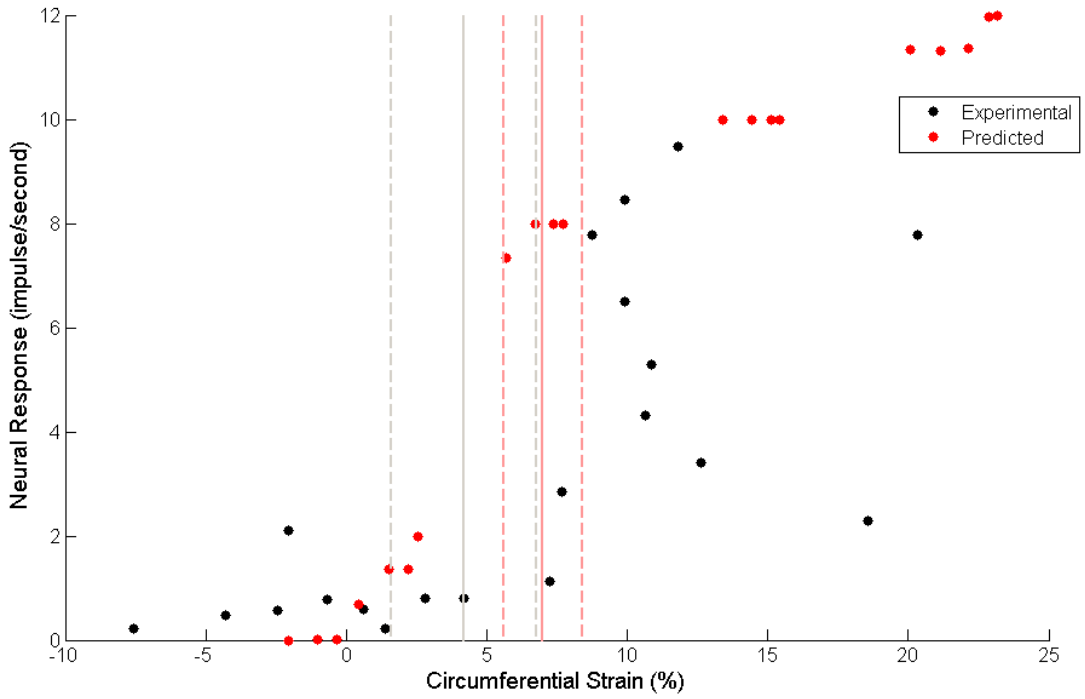

Figure 22: Predicted response from optimised H-H model (red dots), and experimental response (black dots) against the local circumferential strains at the location of Viscerofugal neuron. Solid and dashed grey lines indicate the experimental mean and 95% confidence intervals, and solid and dashed pink lines indicate the predicted mean and 95% confidence intervals for the 6 datasets.

The data displayed in Figure 22 shows that the model is able to predict both the threshold strains for the Viscerofugal neuron and the maximum neural response. The fit that has been achieved here has been through adjusting only one parameter; the coupling factor for equations (34) and (35). This makes the resulting fit more impressive, even though there are still aspects of behaviour that have not been captured by the model. These aspects include the apparent decrease in neural response at higher circumferential strains, and the neural responses being recorded at negative strains. These could be due to the longitudinal loads affecting the neural responses, perhaps as they reach larger values. Another reason for the decrease in neural response at higher circumferential strains could be saturation of the nerve ending as a more extreme stimulus is reached. This is behaviour that has not been included in the neural model, but could be considered in future improvements. Although optimising other parameters of the H-H model could result in a better fit, it is not required as it is the threshold and maximum neural responses that are of more interest to the future stages of this study.

This study has implemented a well-established engineering method, digital image correlation (DIC), to a novel application; sensory neurons and the soft tissues surrounding them. Generally, the neural responses were shown to have a stronger relationship with increases in circumferential strain than with longitudinal strains in the gut tissue samples, as shown in Figure 20, page 44. Unfortunately, the high variability that is displayed by biological systems, such as neurons, means that some of the datasets do not give as high correlation as others. Also, although Viscerofugal neurons have a preference of the circumferential direction, in some cases of high loads in the longitudinal direction, the Viscerofugal neuron will result in a response. This could be due to the neurons having a far higher threshold to strains in the longitudinal direction, or they could be responding to the resultant negative strains in the circumferential direction.

A computational model has been developed to represent both the mechanical behaviour of the soft tissues and the neural response. At this point, the model only displays some of the characteristics of neurons, for example it does not currently include adaption of a neural response. Another assumption that has been made in the development of this model has been that the soft tissue model, in COMSOL, has linear material properties. It is known that soft tissues display nonlinear phenomena, which will not have been captured by the model. However, since the model is only simulating short-term behaviour, neither of these assumptions should affect the results obtained from this study. The purpose of this study was to test the behaviour of the adapted H-H model for the use of predicting neural responses to changes in the surrounding soft tissues. Since the model is able to predict both the threshold and neural responses to maximum tensile strains, we can progress with this model for the neural models of mechanoreceptors in the knee joint.

2.5 Knee specific neural models

Now that a computational model has been calibrated and validated to represent the behaviour of the Viscerofugal neuron, the general neural model can now be adapted to represent the behaviour of the nerve endings found around the knee joint. Very limited data is available on these endings, with the most complete dataset being on the Ruffini ending by Khalsa et al. [21]. Therefore, in some cases, it has been necessary to only fit the models qualitatively. In the following section, the coupling factor from the generalised model has been changed so that the model produces behaviour similar to the Ruffini ending, Golgi tendon organ, and Nociceptor. Since the Paciniform corpuscle displays very different behaviour to that of the other three endings, as described in the literature review

of this chapter, a different adaption to the H-H model has been implemented using a model for the Pacinian corpuscle found in skin built by Holmes and Bell [55, 56]. At the end of this section, the responses of the four types of model are compared qualitatively.

2.5.1 Ruffini ending

The model for the Ruffini ending is calibrated to the most complete set of data available; Khalsa et al. [21]. In this study, samples of feline knee joint capsule were loaded, and the neural response of Ruffini endings recorded. There are several variations between the study described previously for the loading of gut tissue, and the study conducted by Khalsa et al. [21]. Both studies were force driven, however actuators and load cells were used rather than the pulley system used for the gut tissue. Also, the gut tissue was fixed at two edges, while all of the edges of the joint capsule in the experiments of Khalsa et al. [21] were loaded. Finally, more types of loading conditions were applied, allowing shear stresses and strains to be induced. The loading paradigms are shown in Figure 23, indicating how shear loading was achieved, as well as the other types of loading.

The recorded neural responses against the estimated stress in the joint capsule during the full range of loading conditions, as reported by Khalsa et al. [21], are replicated in Figure 24. The plots indicate the six different types of loading; uniform, biaxial, uniaxial *x*, uniaxial *y*, positive shear, and negative shear. They suggest that there is a stronger relationship between the neural response and loading in the *y* direction than loading in the *x* direction. The *y* direction lies along the long axis of the leg. This is highlighted in the neural responses for uniaxial loading in the *y* direction reaching 11impulses/second, while the uniaxial loading in the *x* direction does not result in any strong neural response. However, while there is no *x* stress plotted for the uniaxial *y* loading, some *y* stress is reported during uniaxial *x* loading. In their paper, Khalsa et al. [21] are not clear on the boundary conditions during the uniaxial loading conditions. If the unloaded edges were fixed during the experiment, a stress could have been induced due to the tissue being unable to contract in this direction as would be expected from the Poisson's effect. The magnitude of this stress would depend on the material properties, which are known to be anisotropic in the feline joint capsule [42].

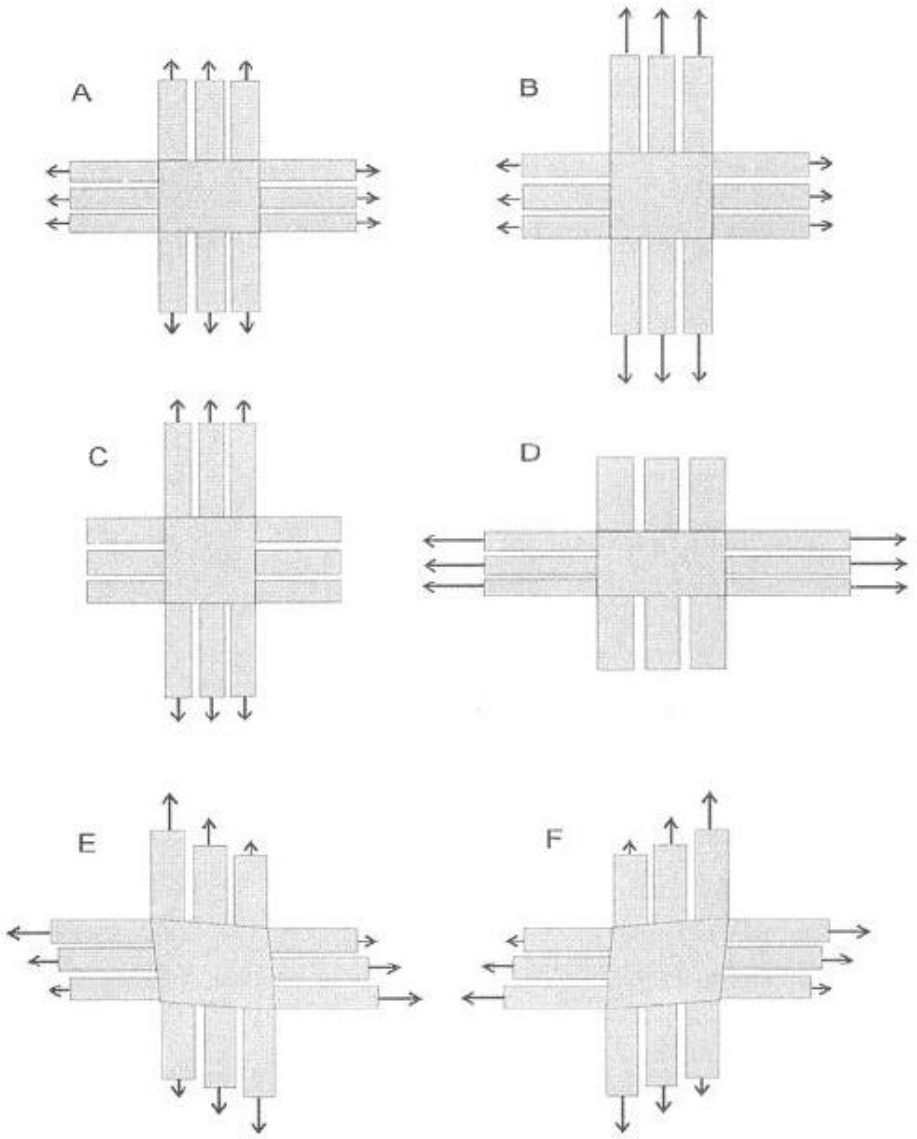

Figure 23: Loading paradigms for stretching the joint capsule. The length of the arrows indicates the relative magnitude of the load applied. A: uniform, B: biaxial (Y biased; biaxial X biased not shown), C: uniaxial Y, D: uniaxial X, E: negative shear, F: positive shear. Image from Khalsa et al. [21].

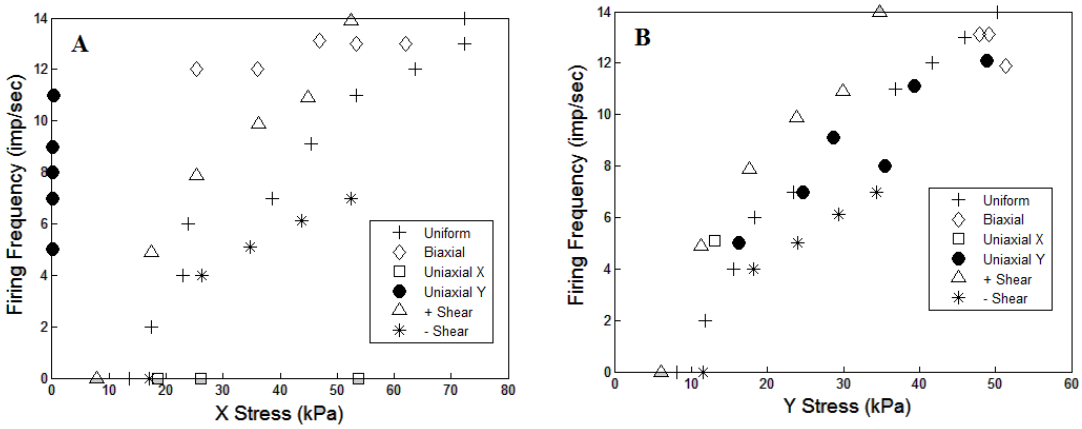

Figure 24: The recorded neural responses to tensile stresses in both x and y directions, from samples of joint capsule, as reported by Khalsa et al. [21]

In this case, the material properties of the samples were not reported so these were included in the optimisation process, using starting positions from the literature [42]. After optimisation of both material properties and coupling factor, the following plots were obtained. The root mean squared error of prediction (RMSEP) for this optimised model is 2.76. As with the optimised model of the Viscerofugal neuron previously, both the magnitude and threshold of the Ruffini ending have been captured by the model. Figure 26 highlights a few outliers, where the model is predicting no neural frequency when Khalsa et al. [21] report frequencies of 4 to 6impulses/second. This is likely to be due to the model perhaps having a slightly larger threshold than the Ruffini ending.

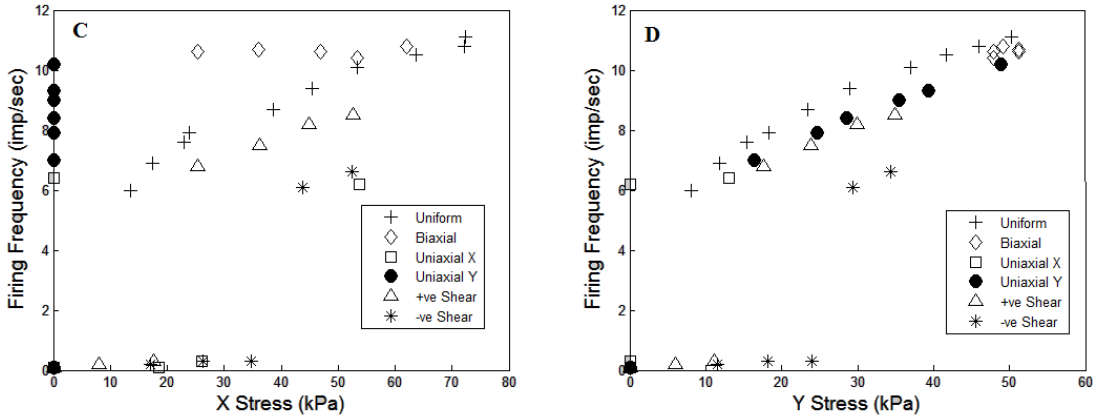

Figure 25: Predicted response from Ruffini model to applied stress, with a coupling factor of 7.5 after optimisation to the data from Khalsa et al. [21].

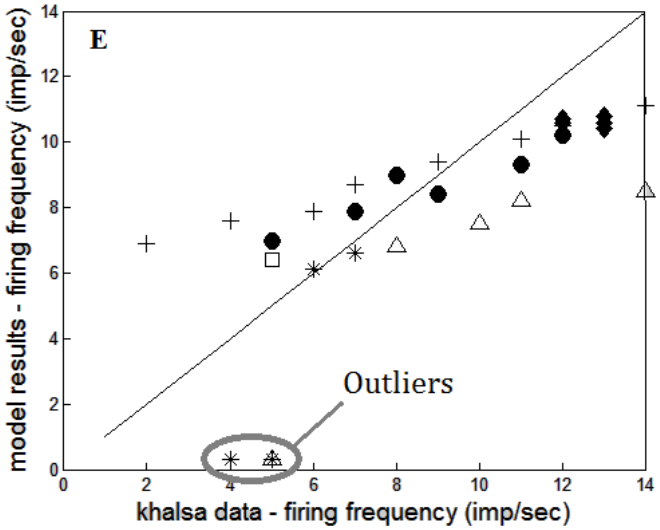

Figure 26: Predicted response plotted against experimental response. A perfect fit is represented by the black line. MSEP value for this is 7.61.

Although the dataset from Khalsa et al. [21] is limited, it is the most complete one available, and has allowed us to calibrate the generalised neural model to produce response similar to that of the Ruffini ending. Since we do not know how the apparently biased behaviour is achieved from the Ruffini ending, or the specific tissue properties of the samples used by Khalsa et al. [21] in their experiments, the optimisation process has been re-run for other scenarios. Altogether, the three scenarios were; anisotropic tissue properties with hydrostatic strain (as shown in the previous plots), isotropic tissue properties with only strain in the y direction, and isotropic tissue properties with hydrostatic strain. In these cases, the tissue properties were optimised as well as the coupling factor. The plots in Figure 27 suggest that the model is producing results with similar mean squared error of predictions (MSEP) for all three scenarios. This suggests that the model is not sensitive to different types of strain input.

Isotropic Ruffini
Isotropic Capsule

E = 1.24MPa
C = 9.94

MSEP = 7.70

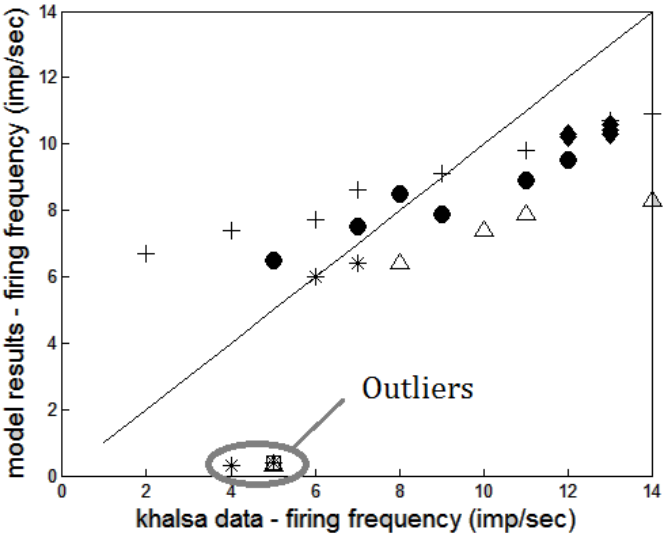

Anisotropic Ruffini
Isotropic Capsule

E = 1.83MPa
C = 10.28

MSEP = 6.64

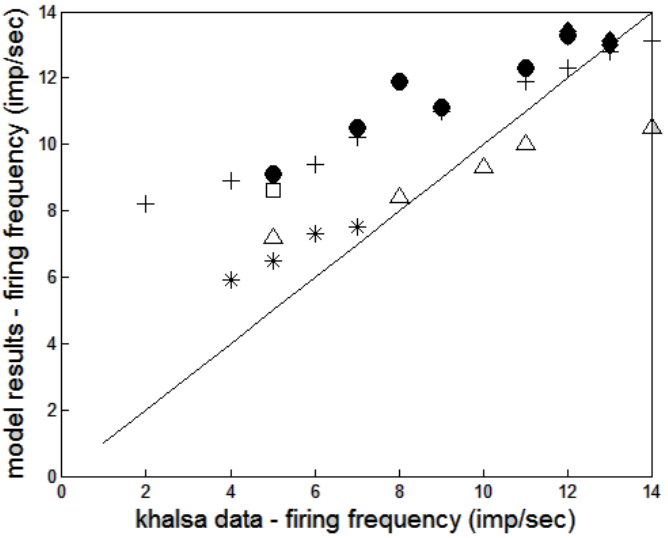

Figure 27: Sensitivity test results, where the model's predictions with different combinations of isotropic/anisotropic tissue properties and isotropic/anisotropic Ruffini ending are tested. Both plots show the model's predictions plotted against experimental predictions, where a perfect fit would be represented by $y=x$, and the top plot shows the predictions for isotropic tissue properties and y strains, the bottom plot shows the model's predictions for isotropic tissue properties and hydrostatic strains.

2.5.2 Golgi tendon organ

As discussed in Chapter 2, the response of the Golgi tendon organ is similar to that of the Ruffini ending. Gregory and Proske [45] record the neural response of this type of nerve ending to tensile loads, measured in grams. They report thresholds of the Golgi tendon organ at around 100g, which is lower than the thresholds of the Ruffini ending [21, 79]. Unfortunately, Gregory and Proske [45] do not report the dimensions or edge displacements of the tissue, so it is not possible to determine the stress or strain that this corresponds to. With no more useful data available to us, the generalised neural model has been adapted for the Golgi, although a different, higher coupling factor is used to allow for the lower threshold; a coupling factor of 9 is used.

2.5.3 Paciniform corpuscle

The Paciniform corpuscle is a rapidly adapting mechanoreceptor, so the generalised model could not be used in this case. Bell and Holmes [55, 56] developed a mathematical model that describes the behaviour of the Pacinian corpuscle, a type of the Paciniform corpuscle that is found commonly in the skin. The encoding part of this model is, again, an adaptation of the Hodgkin-Huxley model, using the model of Bell and Holmes as inspiration. In comparison to the Ruffini model, the adaptation is made in the equation describing the sodium ion channels, equations (40) and (41), as well as the voltage equation (equation (39)). An exponential relationship between changes in the mechanical state and the opening of sodium ion channels is defined, giving the unique Paciniform behaviour. This exponential relationship is developed by Bell and Holmes [55], through determining the energy activation of the ion channel, the rate of which is assumed to be exponential [55]. Though their model also includes the effect of temperature on the Paciniform corpuscle's behaviour, this has been simplified in the model for this study, shown in equation (43).

$$\frac{d\bar{V}}{d\tau} = \frac{[t]}{C}\left[-g_{Na}m^3h(\bar{V}-\bar{V}_{Na}) - g_K n^4(\bar{V}-\bar{V}_K) - g_l(\bar{V}-\bar{V}_l) + \frac{I_a}{[\bar{V}]}\right], \quad (39)$$

$$\frac{dm}{d\tau} = \alpha_m(1-m) - \beta_m m, \quad (40)$$

$$\frac{dh}{d\tau} = \alpha_h(1-h) - \beta_h h, \quad (41)$$

$$\frac{dn}{d\tau} = \alpha_n(1-n) - \beta_n n, \quad (42)$$

with;

$$\alpha_m = \alpha_{m0}[t]\exp(a_1 U + a_2\bar{V}[V]), \quad (43)$$

$$\beta_m = 4[t]exp\left(\frac{\bar{V}[V]}{18}\right), \tag{44}$$

$$\alpha_h = 0.07[t]exp\left(\frac{\bar{V}[V]}{20}\right), \tag{45}$$

$$\beta_h = \frac{[t]}{exp\left(\frac{\bar{V}[V]+30}{10}\right)+1}, \tag{46}$$

$$\alpha_n = \frac{0.01[t](\bar{V}[V]+10)}{exp\left(\frac{\bar{V}[V]+10}{10}\right)-1}, \tag{47}$$

$$\text{and } \beta_n = 0.125[t]exp\left(\frac{\bar{V}[V]}{80}\right). \tag{48}$$

As with the Ruffini model, all the parameters are as defined by Hodgkin and Huxley in the original model [15], see Table 4 (page 29). The parameters a_1 and a_2 have values 1 and 0.01 respectively [55]. *U* is the strain experienced by the nerve ending.

To highlight the Paciniform corpuscle's response to an oscillating stimulus, as often reported from experimental data [33, 54], the model's response to a sinusoidal stimulus has been plotted in Figure 28 below. This displays the 'one spike per peak' behaviour that the Paciniform is known for. The literature also indicated that the Paciniform corpuscle responds to the stimulus rate only and if a stimulus is held over a longer period of time, there will still only be one action potential, which represents the onset of stimulus. This behaviour has been plotted in Figure 29.

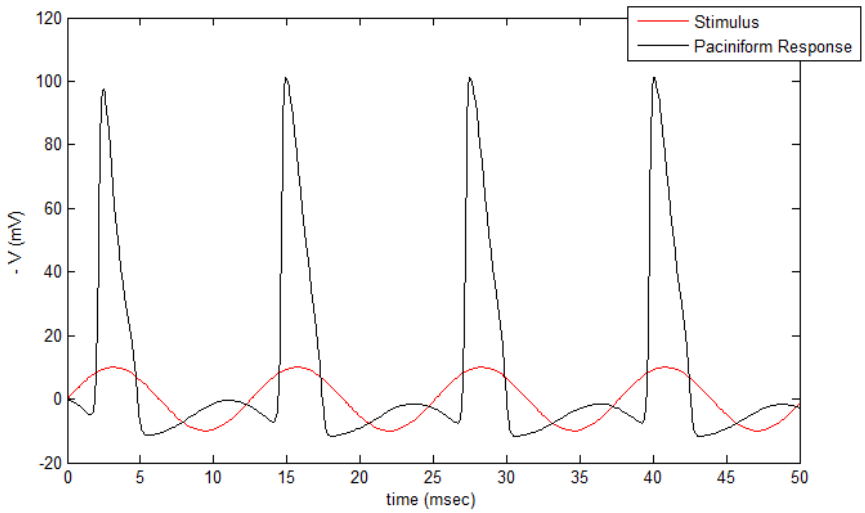

Figure 28: Response of Paciniform model, with the black line representing the response and the red line representing the sinusoidal oscillating stimulus.

Figure 29 shows how the Paciniform model responds to a step-up, step-down stimulus. This is an example of how the Paciniform corpuscle will only respond with a single spike as the stimulus is applied. In this plot, it can be seen that the voltage does not return to zero for 30msec after the stimulus has been removed. This behaviour is not seen *in vivo*, so is a possible area for improvement of this model, perhaps through applying the temperature terms from the Bell and Holmes [55] model or including an ion channel closing parameter. Another area where the model may not be fully capturing the behaviour of the Paciniform corpuscle is in the comparison of tensile and compressive strains. The model will only predict a neural response (as seen in Figure 28 and Figure 29) when the stimulus is a tensile strain. However, since this type of nerve ending is not densely populated in the feline knee joint, this behaviour should not adversely affect the global neural response.

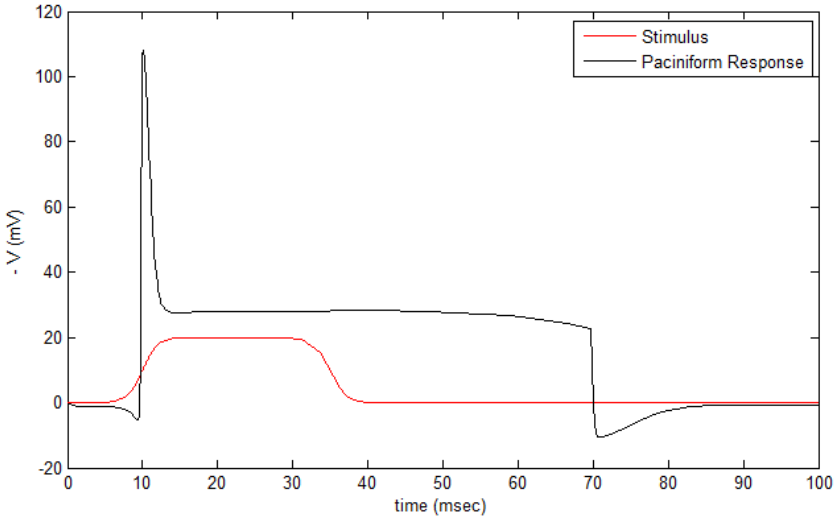

Figure 29: Response of Paciniform model to a step-up, step-down stimulus. The black line represents the response and the red line represents the stimulus.

2.5.4 Nociceptor

As the Nociceptor is a pain specific mechanoreceptor, it only responds to noxious stimuli. A noxious stimulus is a stimulus that is potentially damaging to the soft tissue surrounding the nerve ending. The only available threshold for the Nociceptor in the literature is for that in the skin, which is 0.2MPa [59, 80]. This may be lower than that expected for the tissues in the knee joint, however it is a justifiable starting point for the model. Though we have already indicated that nerve endings are sensitive to strain rather than stress, often the techniques used to determine nerve ending thresholds involve force driven experiments, and the results are reported in stress terms. The model that has been developed to predict the Nociceptor behaviour uses the Ruffini model, with a lower

coupling factor of 1.5. This results in the model having a higher threshold to applied stimuli, as shown in Figure 30.

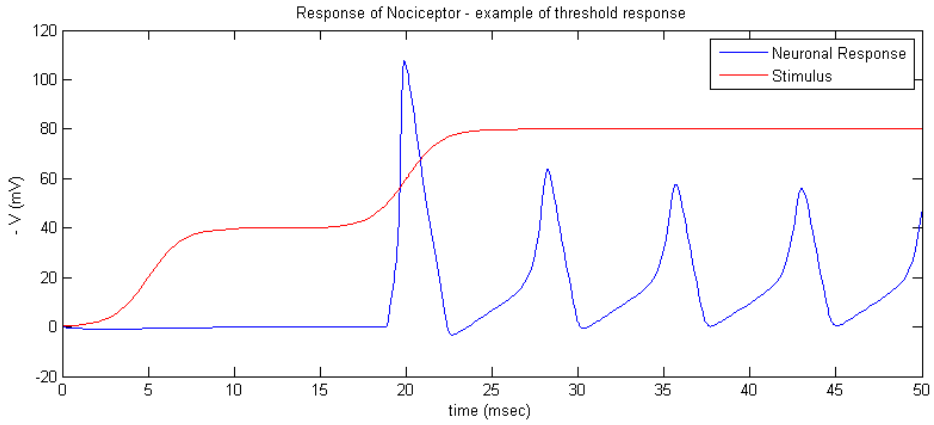

Figure 30: Response of nociceptor model; no response to initial stimulus step, however this changes when the threshold is reached.

As already mentioned, there is little data available describing the behaviour of the Nociceptor. This makes it difficult to calibrate this model, to ensure its behaviour represents reality as well as possible. It is understood that the Nociceptor will adapt if a stimulus is present for a period of time. This is a mechanism known to be present in most nerve endings; however the Nociceptor model does not exhibit this behaviour. This is an aspect of the model which will be pursued later in the project. A specific type of Nociceptor, known as 'silent Nociceptors' are also known to be present in the knee joint; these are Nociceptors that will continue to transmit electrical signals even after the stimulus has been removed. Again, this is an area that has not been included here.

2.5.5 Model Comparisons

Four models representing the behaviour of mechanoreceptors found at the knee joint have been developed. So it is possible to understand how they differ, the same stimulus has been applied to each of the models; two 'step-up, step-down' stimuli, with the second being three times greater than the first. This is an example of how the response of each ending has its own role in sensing different stimuli in the knee joint. Figure 31 shows how a strong stimulus would result in a much higher global frequency response, with the Ruffini ending's response increasing, and the Nociceptor's threshold being reached. The Golgi model has the lowest threshold, and gives the highest frequency response to the stimuli.

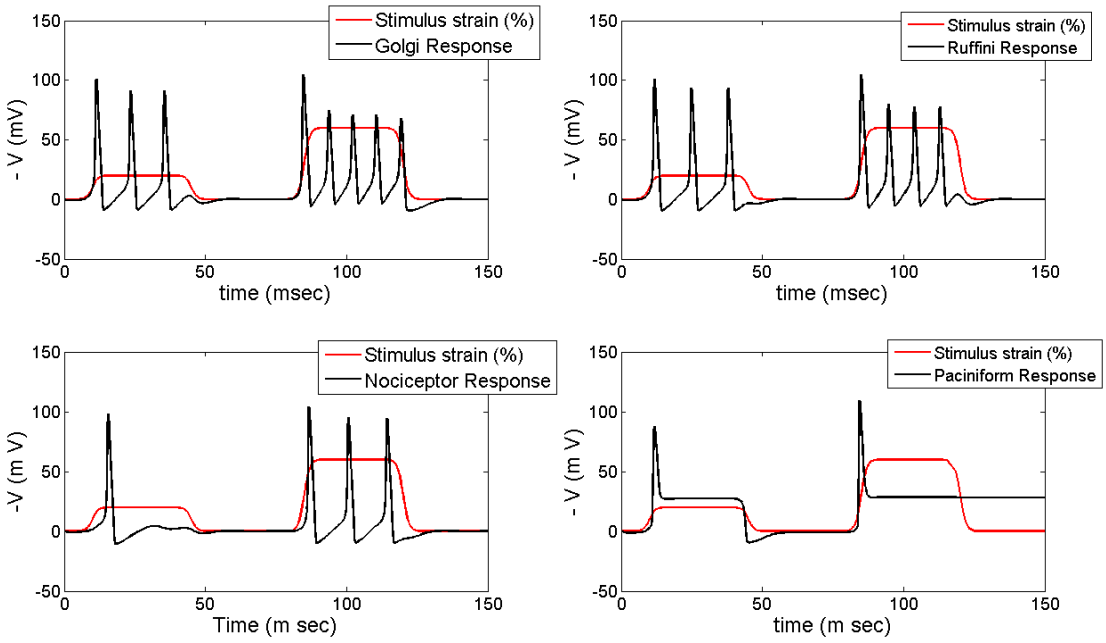

Figure 31: Direct comparison of the response of Paciniform, Nociceptor, Ruffini and Golgi response to two different strengths of stimulus.

As described previously, the Paciniform corpuscle responds to the rate of change of a stimulus, which differs from the other three types of mechanoreceptors. In the figure above this difference is clear, with only a single action potential generated for each occurrence of stimulus, while the other endings produce trains of action potentials for the duration of the stimulus. The variation in behaviour of the four types of mechanoreceptors should allow most stimuli in the tissues around the knee joint to be encoded to a neural signal.

2.6 Discussion

In this chapter, the popular H-H model has been discussed in detail, and stabilised using nondimensionalisation. It has been adapted to represent the behaviour of the four nerve endings at the knee joint, and the behaviour of the general model has been verified using experimental recordings of the Viscerofugal nerve. The adaptations that have been made have been based on two models in the literature; the Nociceptor model of Xu et al. [59] and the Pacinian corpuscle model of Bell and Holmes [55]. In the case of the Nociceptor model [59], the focus of their study was to model thermal pain of the skin, so their results are not comparable with this study. The Pacinian corpuscle model developed by Bell and Holmes [55, 56] included both mechanical aspects and an adapted H-H model. The layered structure of the mechanoreceptor was modelled using shell theory and fluid mechanics

[56], meaning the hoop strain of the receptor was used as stimulus to the H-H based model. Since the structure itself has not been modelled in this study, our results are not directly comparable with those of Bell and Holmes [55]. However, the model is able to predict the unique behaviour of a single action potential per cycle during a periodic stimulus. The advantage of using the H-H model as a basis for the neural models is that a signal response is predicted. This differs from the predictions from some models such as that of the Golgi tendon organ developed by Mileusnic et al [46], where a gain factor was applied to the strain experienced by the mechanoreceptor to obtain a frequency. This is particularly useful when comparing behaviour of the four nerve ending types, specifically the Paciniform corpuscle behaviour in comparison with the other three endings.

The generalised model that was used for the Ruffini ending, Golgi tendon organ, and Nociceptor was tested using experimental recordings from the Viscerofugal neuron. The model was able to predict the neural threshold of the Viscerofugal neuron and the maximum frequency values. Possible improvements for the model include using ionic conductances, which could be recorded experimentally, to allow the H-H model to be fitted to the specific species, as the original H-H parameters are for the giant axon of a squid. The models that have been developed in this chapter are for use in a larger scale model, which can predict the global neural response of a feline knee joint during a range of movements. Unfortunately there is very limited data available for optimisation and verification of the knee specific neural models. However, since we have been able to show that the general model can predict important aspects of the Viscerofugal neuron's behaviour, we have assumed that the other models are behaving satisfactorily also. It has been possible to test the model's sensitivity to the input stimulus; after running optimisation of the coupling factor for different types of input strains, little difference in behaviour was observed. The methods used for applying these models to the knee joint model, and for combining multiple signals are described in chapter 4.

Chapter 3

Development of a Feline Knee Model

3.1 Introduction

Previously in this thesis, computational neural models have been developed for each of the four mechanoreceptors known to be present at the knee joint. Since this project focusses on the global neural response to changes in joint position, a computational model that represents the feline knee joint must be developed. This chapter describes the development process for building a three dimensional, finite element (FE) model of a feline knee joint. Figure 32 highlights how this work is related to the overall project. At the end of this chapter, the model is in a state that is ready for integration with the four neural response models.

As described in Chapter 2, the joint capsule and fat pads of the knee joint are known to be highly innervated [17], so it is necessary to include these structures in the knee model. They are not included in current finite element models of knee joints, as these models are generally developed with stability as a primary interest; for which the ligaments are far more involved than the capsule and fat pads. For this reason the model that is developed in this chapter contains original elements. Another area which provides a challenging component to this project is that it is a model of a feline knee joint, and not human. There are no current FE models that focus on the feline knee joint, and very limited data available on the properties of the soft tissues around the knee joint of this particular species. This lack of knowledge of the structures specific to the feline knee joint means that assumptions will have been made based on knowledge from other species.

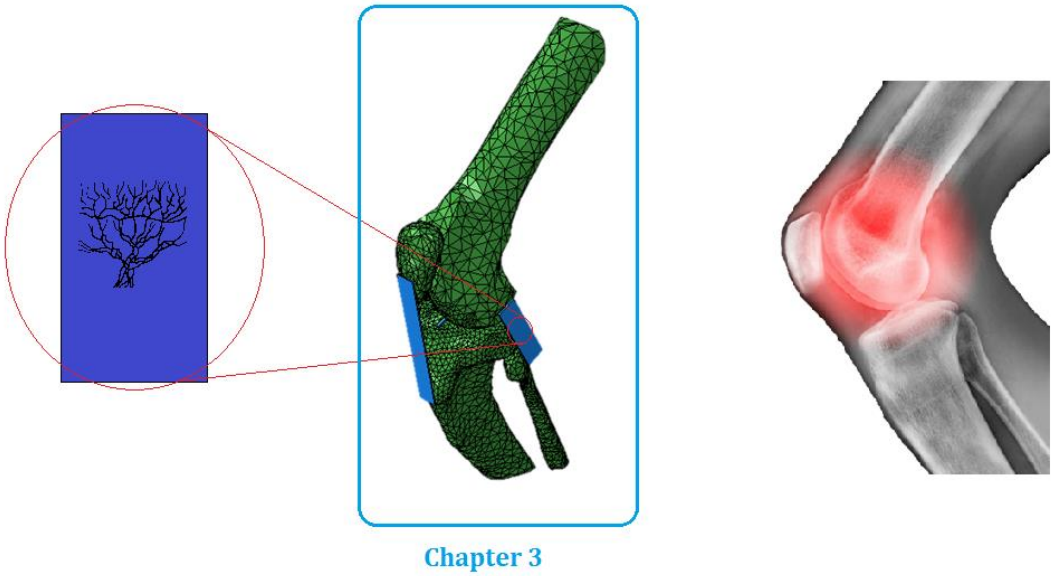

Figure 32: Diagram to show how the work in this chapter is involved in the overall project, repeated from chapter 1.

The first section of this chapter describes the anatomy of the knee joint, and how it differs between feline and human. Modelling methodologies are then discussed for each type of structure in the knee joint, and for a knee joint as a whole. Finally, the model development process is described in detail, and its behaviour tested qualitatively.

3.2 Literature Review

The purpose of this section is to describe the knee joint and structures that provide for its function. The current methods used for modelling knee joints, and the relevant soft tissues are also discussed. This will indicate the most appropriate methodologies for development of a computational model of a feline knee joint. As discussed in the previous chapter, most of our understanding of the neuronal activity at the knee joint is focussed on that of the feline, however most models of the knee joint have been developed to describe the human knee joint. For this reason, both the human and feline knee joint will be described and compared, with purpose to determine the extent of transferrable information between the two joints.

3.2.1 Anatomy of the knee

The general structure of the knee consists of the tibio-femoral and the patella-femoral joints; the tibio-femoral joint is unstable and requires a complex architecture of soft tissues to ensure stability [81]. There are four major ligaments present in this joint; the anterior and posterior cruciate ligaments, and the medial and lateral ligaments (Figure 33).

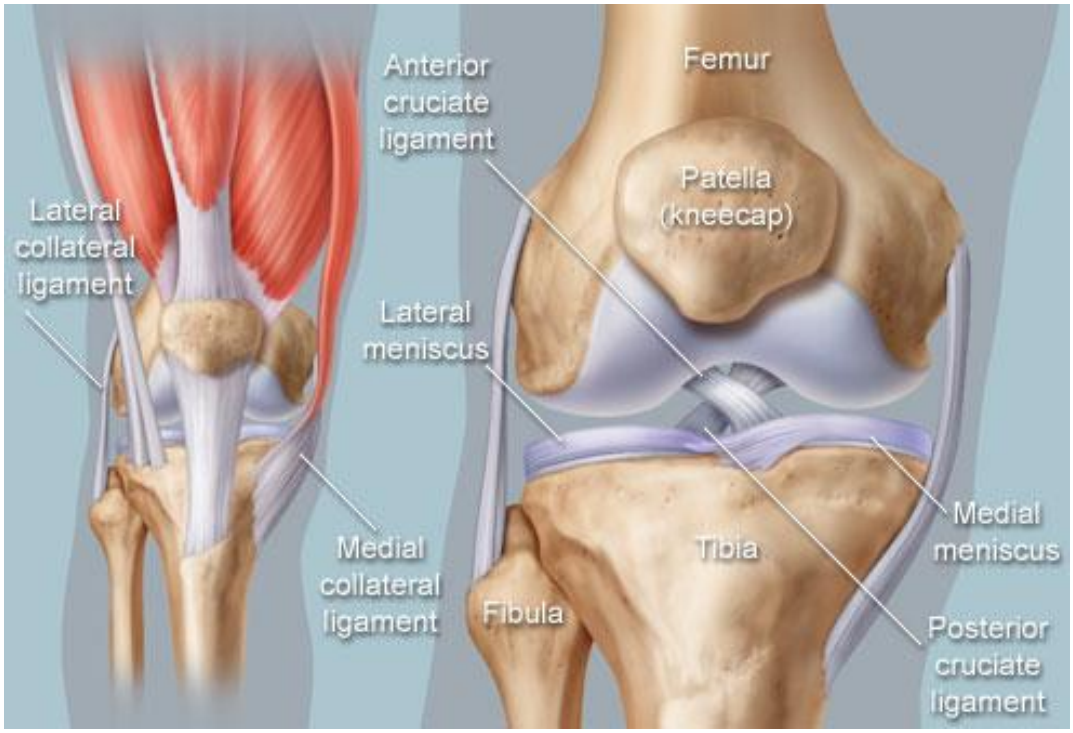

Figure 33: Anatomy of the human knee joint, image from WebMD [82], indicating the major structures.

It has been suggested in the literature that the human knee is comparable to that of the feline [83, 84]. The images in Figure 34 represent the structure of the feline knee joint; the similarities with the human knee are evident, with the major ligaments being the same. Prosé [84] gives a detailed description of the anatomy of the feline knee joint, followed by a discussion and comparison with the human knee joint. He suggests that the main differences occur in the proportions of the components in the joint [84].

The most prominent difference that is highlighted between the feline and human knee joints is seen in the groove in which the patella fits in the femur; that of the feline reaches further proximally and has marked ridges medially and laterally that the human knee does not have. The feline knee joint transmits forces at a lesser degree of extension than the human knee, resulting in all muscles involved in extension being better developed in the feline. This does not appear to affect the ligaments however, as Prosé [84] indicates that there are no clear differences in shape, attachment or arrangement of cruciate ligaments

of man and feline. The cross section of cruciate ligaments of both human and feline knee joints are generally circular in shape [84], with attachment sites on the femur and tibia such that a cross shape is created between the two ligaments. Other differences between the human and feline knee joint involve the shapes of bony structures, such as the femoral condyles being more parallel in the feline, and the shape of proximal end of the feline tibia being more triangular than the oval human tibia [84].

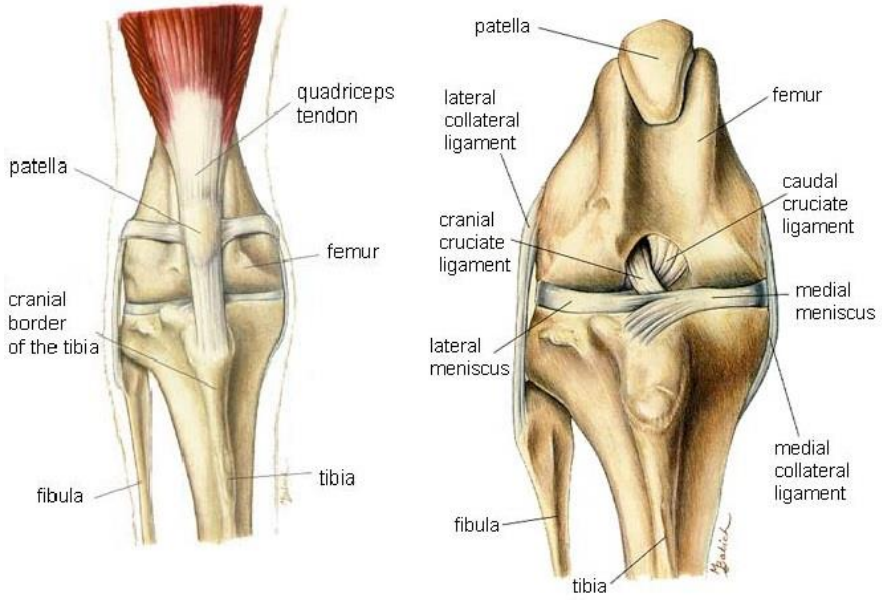

Figure 34: Anatomy of the feline knee joint, image from Hill's Pet Nutrition [8], indicating the major structures in the joint.

The cartilage thickness around the surfaces of the feline knee joint have been reported to be between 0.3 and 0.6mm [85], while that of the human knee joint has been reported to be between 0.8 and 2.5mm [86]. This difference should not be a surprise, based on the difference in joint sizes and the loads that will be experienced by the cartilage. The loads experienced by the knee joints of the two species are likely to be very different, based on their masses alone. The uses of the two types of knee joints also differ, with one being a two legged mammal, and the other being four legged; this affects the range of motion of the joints, which is described in section 3.2.2. Finally, the combination of loading conditions and range of motion being different between the human and feline knee joints would result in the most common failure mechanisms being different. For example, the human knee joint is inherently unstable, with failure or damage of the ACL being one of the more common injuries, while the feline knee joint is more stable with injuries being relatively uncommon.

Since the soft tissues are of most interest to us in this project, and there are no clear differences in shape or attachments between human and feline, we can assume that there are enough similarities between the two knee joints for direct comparisons, anatomically. However, there are still differences between the two joints, such as range of motion and tissue properties. These will be discussed in the following sections.

3.2.2 Range of Motion

As mentioned above, one major difference between human and feline knee joints is in the range of motion that they experience [84]. Again, the purpose of this study is to model the neural response to different joint positions. Much of the published data is related to moving the joint to *maximum* positions of the feline knee joint, therefore it is important to understand the complete range of motion that it will realistically experience (Table 7) as compared to the human joint.

The angles for flexion, extension and neutral position in Table 7, for both feline and human knee joints, assume that an angle of 0˚ occurs when the tibia is flexed to be parallel with the femur. For internal and external rotation positions, 0˚ is assumed to be at the knee's resting position. The anterior tibial drawer test is a popular method for determining the laxity of the knee joint. The ACL is the main ligament to restrict the anterior movement of the tibia, so this test is often used to check for damaged ACLs. Though this test is also used for determining ACL damage in the feline knee joint, it is an uncommon injury so there is no literature describing measurements of the anterior drawer of the feline tibia.

		Human Knee	Feline Knee
Neutral Position		180˚	120˚
Maximum Flexion		42.5˚	30˚
Maximum Extension		182.5 ˚	195˚
Maximum Internal Rotation	**At 30˚ flexion**	7.7˚	15.3˚
	At 90˚ flexion	7.7 ˚	7.7˚
Maximum External Rotation	**At 30˚ flexion**	13 ˚	14˚
	At 90˚ flexion	5.3 ˚	5.2˚
Maximum anterior tibial drawer		0-5mm	-

Table 7: The maximum positions in degrees (and mm, for the maximum anterior tibial drawer), for both human [87, 88] and feline knee joints [89-91] 5.

3.2.3 Modelling Methodologies

3.2.3.1 Soft Tissues

The soft tissues that are considered in this study are those that are known to be innervated; ligaments, tendons, fat pads and joint capsule. Though both skin and muscles are known to be innervated, and involved in proprioception they have not been included in this model since the focus of the project is determining whether the joint receptors (found in the deep tissues of knee joint, such as ligaments and capsule) are involved in proprioception. The properties and modelling methods of the four soft tissues of interest are summarised in Table 8 (page 71). The material properties summarised in the table are for soft tissues in human, except for the joint capsule, which is from feline knee joint [42]. The following sub-sections, however, describe the functions, properties and modelling methods in more detail.

[5] Feline knee positions also advised by Petra Agthe, Medical Imaging Specialist, Anderson Moores Veterinary Specialists

3.2.3.1.1 Ligaments

There is a far larger catalogue of modelling methods for ligaments than any other soft tissue of interest here, which varies from assuming linear behaviour to modelling the collagen fibres and surrounding matrix [92]. Though the latter of these methods is likely to be the most accurate, it also required a large amount of data for calibration, and is also likely to be computationally expensive.

The properties of tissues within one species are highly variable, depending on the age of the subject and the location of the soft tissue. There have also been studies showing variation of tissue properties between species [93]. It has been suggested that as the animal size decreases, the elastic modulus of ligaments increases [93, 94]. Though these studies do not specifically describe the ligaments of the feline knee joint, this trend has been taken into account when developing the computational model. An example of the nonlinear behaviour of ligaments is seen in Figure 35, which shows the stress-strain curve for rat MCL during tensile loading [95].

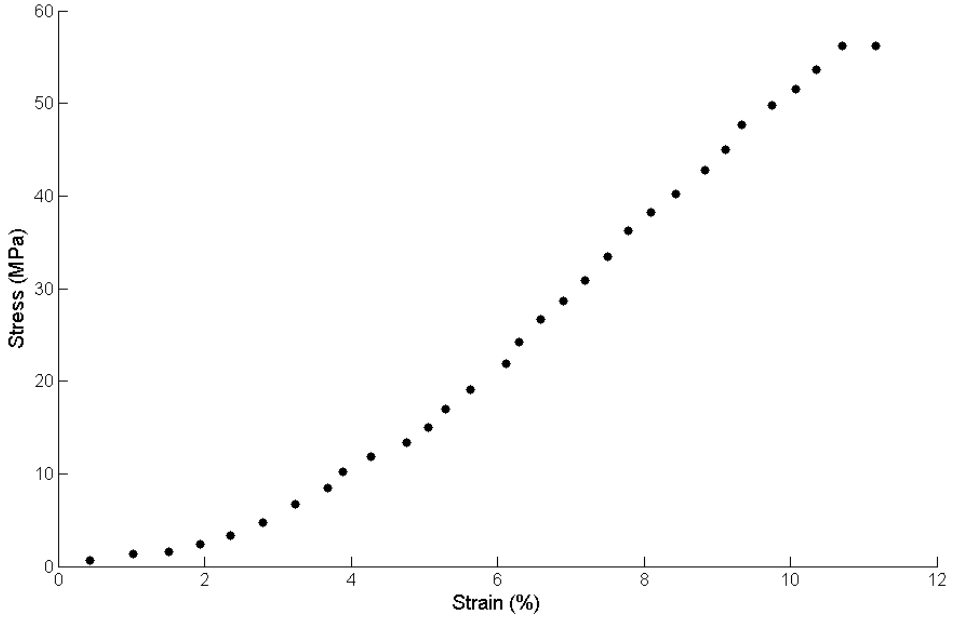

Figure 35: Stress-strain curves for control rat medial collateral ligament, reproduced from figure 5A of Provenzano et al. [95].

The curve in Figure 35 above is typical of ligament nonlinear behaviour, with an initial low stiffness region. The stiffness then increases significantly, in this curve at around 2% strain, behaving fairly linearly before the ligament begins to fail [64, 95, 96]. This

behaviour is only seen during tension; ligament behaviour is very different during compression. This type of soft tissue cannot hold its shape under a compressive load, it will buckle. Other tissue properties that are displayed by ligaments include creep, stress relaxation and hysteresis [96, 97]. However, the model that has been developed in this study does not consider effects of time on behaviour, so these properties have not been considered in the modelling of ligaments. Table 8 (page 71) summarises ligament properties and potential modelling methods available.

3.2.3.1.2 Tendons

Tendons attach muscles to bone; an example is the quadriceps tendon which connects the quadriceps muscle to the patella. Tendons have similar properties to ligaments but generally display higher stiffness [96]. This higher stiffness is due to the almost entirely well-aligned collagen fibres, and is required so that the forces exerted by muscles are not modified by creep or relaxation of the tendons [96].

Although the knee joint does have tendons present, which are included in the FE feline knee model, there is no literature describing their behaviour. Since there is already the generalisation that all ligaments in the knee have the same properties, it is has also been assumed that the patellar tendon also has the same properties.

3.2.3.1.3 Joint Capsule

The joint capsule is a membranous tissue that lines the entire joint, and serves multiple functions. One is to keep the synovial fluid of the joint in position, and the other is to provide stability to the joint. Though the majority of the capsule is thin, it thickens in areas to form the MCL, LCL and patellar ligament, thus providing stability to the knee. Clearly, the properties of the capsule vary greatly throughout the joint. The thickened regions can be assumed to have properties of ligaments, as described previously, and the rest will be assumed to have 'capsule' properties.

The posterior section of feline knee joint capsule was measured by Hoffman et al. [42]. They described the capsule to be composed of three regions of different stiffness, as shown in Figure 36. Region 1 represents a cable-like structure with far stiffer properties to the rest, with horizontal elastic moduli of regions 1, 2 and 3 being 9.32 MPa, 2.17 MPa and 1.90 MPa, respectively. The vertical modulus was not shown to vary with location, and was reported as 0.7 MPa.

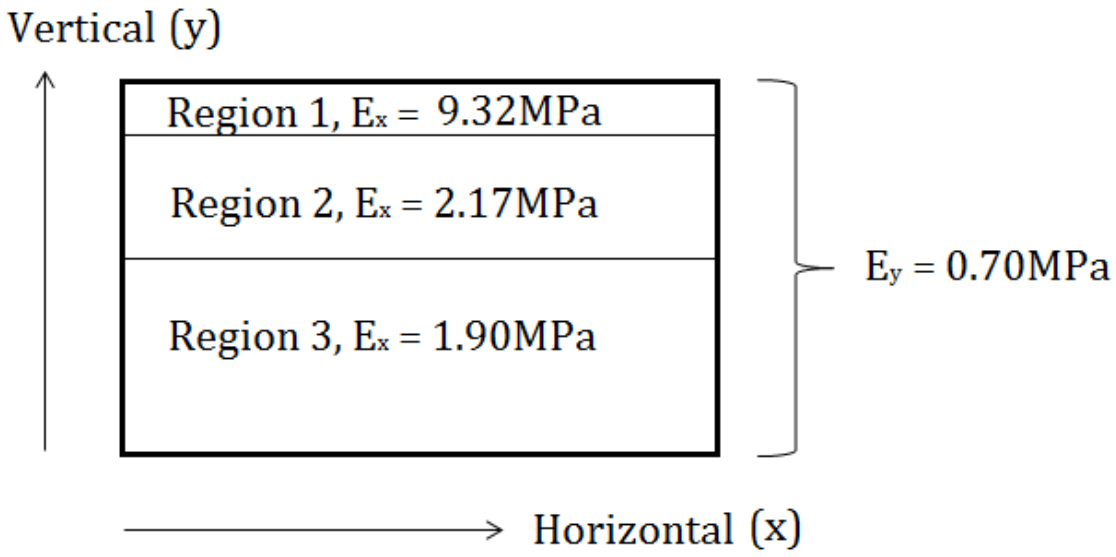

Figure 36: Posterior knee capsule, highlighting the three regions of different tissue properties reported by Hoffman et al. [42]. Image reproduced from Fig. 1 in Hoffman et al. [42], regions are not to scale.

Hoffman et al. [42] also develop a biomechanical model of the upper margin (region 1) of the posterior joint capsule. Since it has a far higher stiffness than the rest of the capsule, they base the model on a two-segment catenary suspension cable. They do not model the other regions of the capsule; however their tensile tests suggest that the behaviour is linear.

3.2.3.1.4 Fat Pads

The fat pad in the knee joint, also known as Hoffa's fat pad, is found in the space between the back of the patellar ligament, the femur and tibia, shown in Figure 37. Through analysing its deformation during flexion and extension, it has been shown to have a cushioning role in the knee [63]. Hamarneh et al. developed a model to represent the deformation of Hoffa's fat pad. In this model, the fat was assumed isotropic, with elasticity parameter of 150 kPa. The purpose of this model is to focus on the deformation of Hoffa's fat pad, through use of image registration techniques during knee flexion, through measuring volume changes.

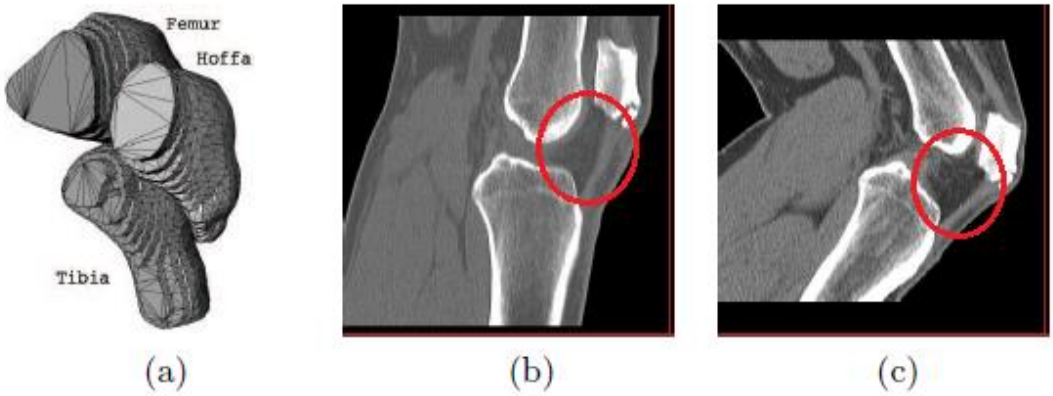

Figure 37: The Hoffa's fat pad shown (a) in relation to the femur and tibia bones. Sagittal CT slices showing the fat pad of a human knee in (b) extended and (c) flexed positions, highlighted by red circles. Images adapted from figure 1 of Hamarneh et al. [63].

This is the only model developed for Hoffa's fat pad in particular, however data does exist describing the behaviour of fat pads in the foot heel, the calcaneal fat pad, and other areas of the body [98-100], which suggest that the compressive modulus is around 105kPa.

Table 8: A summary of the properties and modelling methods of the four major soft tissues in the knee joint [1, 13, 17, 42, 63, 92, 93, 97-104].

Soft Tissue	Function/description	Tissue Properties	Modelling Methods
Ligaments	- Attaches bone to bone - Multi-scale structure	- Non-linear viscoelastic - Buckle under a compressive load - Elastic modulus of human ACL 65MPa-111MPa	- Empirical/discrete - Collagen fibres & surrounding matrix - Assume internal friction between fibres - Springs/dampening - Discrete element networks; cannot predict stress - Isotropic material symmetry; large errors - Transversely isotropic material symmetry
Tendons	- Attaches muscle to bone	- Same general properties as ligaments, but with higher elastic modulus	- See ligament modelling methods
Joint Capsule	- Tissue that lines the cavity of knee joint - Provides stability and keeps synovial fluid in position - Medial and lateral of capsule thicken to form MCL and LCL	- Posterior capsule properties are more stiff in upper section than lower; - horizontal elastic moduli 9.32MPa, 2.17MPa, 1.8MPa - vertical elastic modulus 0.7MPa	- Model developed by Hoffman et al., describing capsule to behave as a suspension cable.
Fat Pads	- Provide cushioning to the joint & energy storage	- Will not buckle when experience compressive loads - Compressive modulus of fat pad ~105kPa	- Isotropic behaviour.

3.2.3.2 Entire Joint

The modelling methods of individual structures in the knee joint have been identified now, the methods for developing a model of an entire joint should be discussed. Very little modelling literature is available of the feline knee joint specifically, as it is not a commonly damaged joint [105], and therefore not examined in detail. The only model that has been developed is that of Burkholder et al. [106], who built a three dimensional model of the feline hind limb, based on digitised musculoskeletal anatomy. The model consisted of the hip, knee and ankle, digitised the anatomy of five cats using the software DADS [107], and has seven degrees of freedom. Though the geometry aspect of this model was detailed, the focus of Burkholder et al. [106] in their study was on the muscles and the moment arms generated by them, rather than ligaments. For this reason, and the fact that no tissue properties were revealed, the methods are not transferrable to this project.

Though there is little literature available on the computational modelling of feline knee joints, the modelling of human knee joints is well developed and recorded. The most popular methods implement finite element analysis [108-111], using powerful software such as Abaqus CAE. The general process that is followed for developing a computational model of a knee joint is described by Chizari et al. [108], and shown in Figure 38. As already discussed, properties of tissues in the feline knee joint are not readily available; however scaling laws are extremely prominent in animals, so using knowledge of tissue properties in other species it is possible to estimate those specific to the feline. Since the general structure of the feline knee joint is comparable to the human knee joint, as described previously, and it is the soft tissues that are of most interest in this study, the modelling methods used for human knee joints can be transferrable.

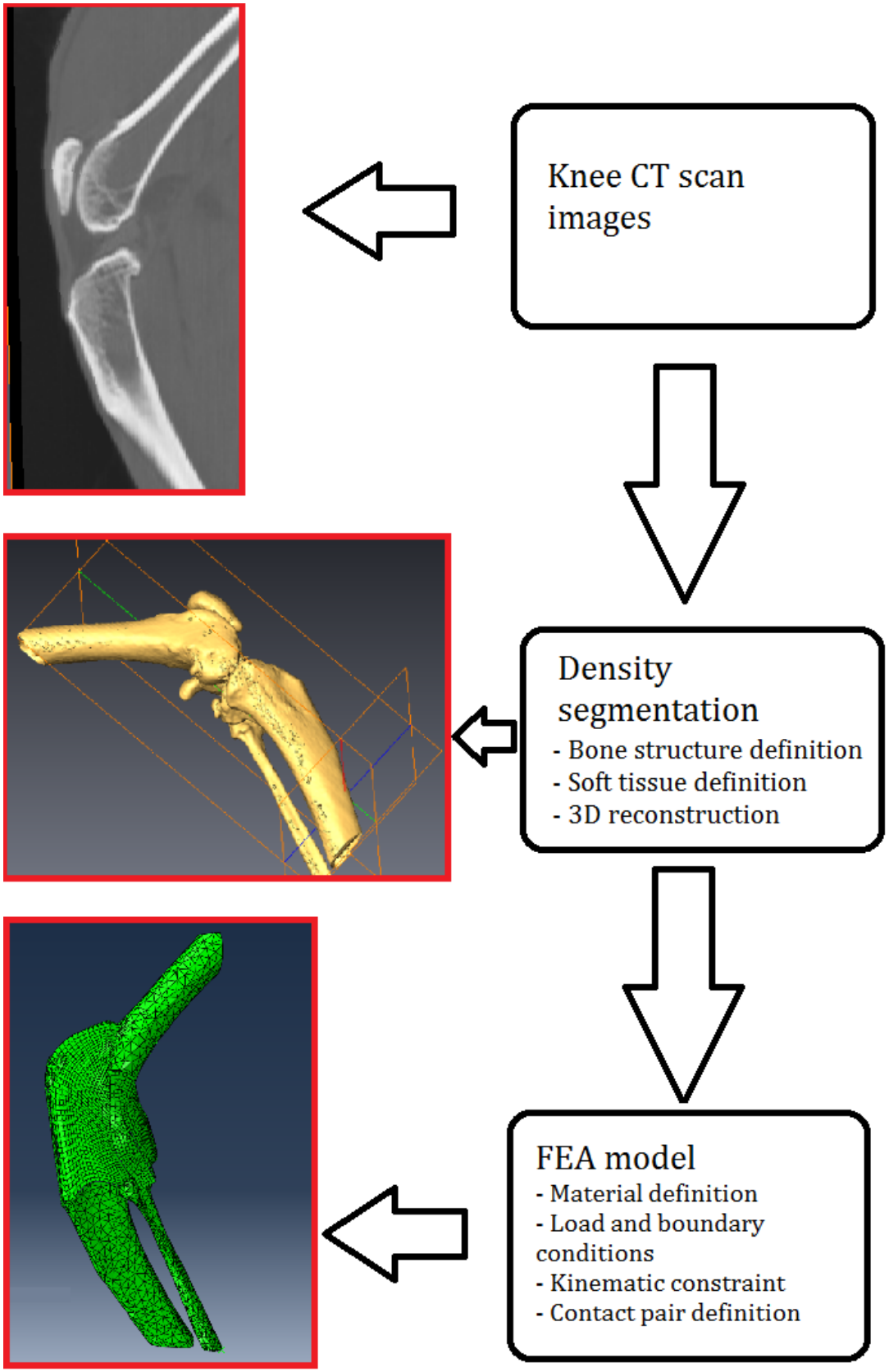

Figure 38: Modelling methodology of 3D modelling of a knee joint, reproduced from Chizari [108], beginning with scans from a knee joint and resulting with a finite element model of the joint.

A geometry model of the knee joint can be generated using image processing analysis software, such as Avizo [112], with sets of x-ray Computed Tomography (CT) and Magnetic Resonance Imaging (MRI) scans. X-ray CT scans provide clear images of bone, while MRI scans can give clearer images of soft tissues in the joint. Visualisation software, such as Avizo, can be used to identify the relevant structures, in a method known as segmentation. The fully manual method can be both lengthy and tedious, so automated processes are very appealing. Both semi-automatic and fully automatic methods exist, and are possible through use of pattern recognition techniques [113]. In these techniques, the major structures within the scans can be identified automatically based on similarities with an 'average' dataset. The major limitation of these automated methods, however, is that any abnormal or damaged structures may not be recognised by the algorithm.

Once the required geometries have been obtained from the x-ray CT and MRI scans, the geometries are meshed ready for finite element simulations with applied loads. If structures are being modelled as rigid bodies, then a triangular surface mesh is adequate [108, 112]. Other structures, such as the soft tissues can be composed of either hexahedral [114] or tetrahedral [108]. Hexahedral elements are generally preferred for soft tissues since they maintain smooth surfaces, even for thin structures, as well resisting large deformations. Sometimes a separate piece of software for meshing with elements of this type is usually required, however, meaning the less robust tetrahedral elements are often used.

Finite element models of joints can be force driven or displacement driven, depending on the purpose of the model. If the muscles are being modelled, and it is the change in the joint's position in response to these of interest, then the model should be force driven. Force driven models, however, can be more difficult to control, as both the *in vivo* force magnitude and direction are required. Since this project is concentrating on the neuronal activity due to changes in position of the joint, displacement control is the preferred option. A further advantage of developing a displacement controlled model is that rigid bodies are best moved through applying displacement to the reference point.

The use of rigid bodies in computational modelling is a method that can be implemented if certain structures within a model are not expected to deform, or are of less interest to the modeller [108]. This can result in lower computational costs, as only the displacement of an object is calculated; not the deformation. In the case of this project, it is possible to model the bony structures as rigid bodies, since they have higher stiffness [96] and are

unlikely to deform greatly and it was the mechanical states of the soft tissues which were of interest. The properties and modelling methods of these soft tissues are described previously in section 3.2.3.

3.3 Building the Finite Element Model

The remainder of this chapter focusses on the development of the finite element model of feline knee joint, through developing the individual features of the knee. Established methods in finite element modelling of joints are implemented for this part of the study [108, 115]. The model is described with the bones only; femur, tibia, fibular and patellar tendon. Here the contacts between bones are implemented, to represent the presence of cartilage, and the boundary conditions required for changes in joint position. The ligament geometries are then created, and their properties described, before connecting to the bones. Finally, the capsule and fat pad are created and applied, each with their own properties and connection methods. As already mentioned, inclusion of joint capsule and fat pad make this computational model of the knee novel, as there is no current model including all of these structures.

Abaqus/Explicit is used for analysis of the model instead of implicit modelling. Although the model is not required to be run as a function of time, large deformation of the soft tissues was expected, and since the bones were modelled as rigid bodies, there was likely to be rigid body contact; factors which are not supported by the implicit Abaqus/Standard well. As summarised in Figure 38 (page 73), the basis for building the 3D finite element model of a feline joint was a set of X-ray CT and MRI scans. The set of X-ray CT and MRI scans of a feline knee joint have been obtained, with thanks to Irene Schaafsma and Petra Agthe[6].

The X-ray CT images were taken from the left hind leg of an adult cat, using 0.6mm slices in the transverse plane, and MRIs from the same hind leg, using a range of sequencing methods, allowing all required structures to be viewed. X-ray CT scans are generally only used for building models of bony structures, while soft tissues are extracted from MRI scans. However, even use of the finest settings of the medical MRI scanner, smooth images of a joint of the small dimensions of the feline were not possible. For this reason, the MRI scans have been used qualitatively. Geometries of the soft tissues have been simplified, using dimensions taken from the structures in both X-ray CT and MRI scans, allowing

[6] European Specialists in Diagnostic Imaging at Anderson Moores Veterinary Specialists, www.andersonmoores.com [accessed 09/10/2013].

structures to be meshed more easily. The easier a structure is to mesh, the higher the mesh quality is likely to be, resulting in better element behaviour. As already described, the experiments that have been replicated by the FE model were performed after removing the quadriceps tendon, therefore this structure has not been included in the model.

3.3.1 Bones

3.3.1.1 Geometries

The geometries of bone structures were built through segmentation process of the x-ray CT scans of the feline knee joint. Avizo Standard 6.3 [112], was used to segment the required bone structures from the image stacks; femur, tibia, fibular and patella.

Figure 39: Image of geometries of the bony structures of the feline knee joint, after segmentation of x-ray CT scans using Avizo Standard 6.3.

3.3.1.2 Properties and meshing

As summarised in the literature review, the innervation of bones is not well documented. However, while it is likely that they are involved with nociception, it can be assumed that they are not involved in proprioception; the main focus of this project. Since innervation of bones has not been included in this model, it was not necessary to calculate the deformation of these structures. Bone also has a far higher stiffness than soft tissues [96, 97]. For these reasons, the bony structures have been modelled as three dimensional, discrete rigid bodies. In order to import the bone geometries to Abaqus from Avizo, triangular surfaces were created (Figure 40).

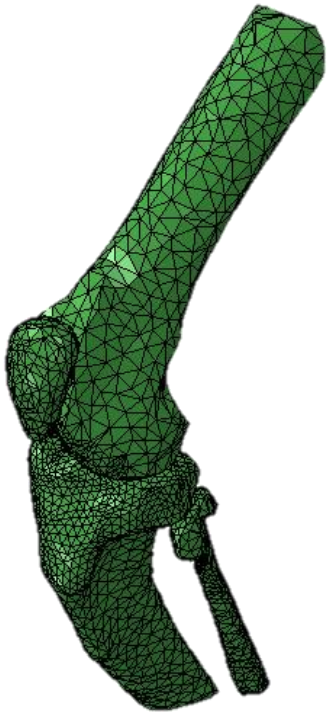

Figure 40: Meshed bony structures of the knee joint, after exporting to ABAQUS, using triangular elements.

Since the bones are modelled as rigid bodies, their material properties are not necessary for this model. However, since the model was run explicitly over a time of 0.01 seconds (chosen for a reduced run time), their inertial properties are required to ensure the complete model has the correct mass; these values are shown in Table 9 below. They have been calculated using mass from estimates of their volume and the assumption that average bone density is equal to $1500 kg/m^3$.

	Mass (g)	Inertia (gmm^2)		
		I_{xx}	I_{yy}	I_{zz}
Femur	18	61416	30528	404528
Tibia	18	72810	24498	55872
Fibular	2	5384	1348	4330
Patella	1.2	300	108	346

Table 9: Inertial properties of the four bones in the feline knee joint; the femur, tibia, fibular and patella.

3.3.1.3 Interactions and boundary conditions

Although the bones are modelled as rigid bodies, they still experience contact between each other. More specifically, there is contact at the femur-tibia joint, tibia-fibular joint, and patella-femoral joint. Cartilage is a tissue located at the contact points between bones, so that minimal friction is obtained and to protect the bones from premature damage. Since there is no innervation of cartilage [17], its deformation was not required for calculation. However, without cartilage in the model there would be a gap left between the bones obtained from the x-ray CT-scans. Cartilage, along with synovial fluid, also allows for low coefficient of friction between bones. To represent the presence of cartilage, frictionless contact between bones is defined. A contact thickness of $0.5mm$ was defined, to model the effect of a surface coating thus representing the presence of cartilage [85, 116].

In order to verify the behaviour of the FE knee model, it will be important to replicate experimental methods described in the literature. In one such paper, Grigg [39] reports the torque-joint angle relationship for passive flexion and extension of the feline knee joint. The experiments carried out by Grigg [39] involved the fixing of hip and femur, while the tibia is displaced. To represent this, the femur is fully constrained, the fibular tied to the tibia, and the tibia moved through application of appropriate displacement. The patellar does not require any artificial constraint, as its movement is controlled by the patellar tendon and joint capsule. Displacement is applied to the tibia through application of boundary conditions to its reference point. The tibia is moved from its initial, neutral position of 120° to the maximum positions defined in Table 7 (page 66). Table 10 summarises the boundary conditions applied to the tibia in order to achieve these displacements.

	Required Displacement	Applied boundary conditions		
		X axis	Y axis	Z axis
Flexion (30°)	90°	90 °	0 °	0 °
Extension (195°)	75 °	-75 °	0 °	0 °

Table 10: Applied boundary conditions to the tibia to achieve flexion and extension of the knee joint, from its initial position of 120°.

3.3.2 Ligaments

3.3.2.1 Geometries

As already mentioned, the MRI scans available are not fine enough to generate the smooth and regular soft tissue geometries that are required for an acceptable mesh. For this reason, simplified structures were created, using dimensions obtained from the scans using the FE software, Abaqus [117]. It was possible to determine the insertion sites of each ligament from the MRI scans, from which the dimensions could be calculated. Simple rectangular cross-sections were used for each ligament, which were then extruded to the required length. Figure 41 shows these simplified structures with the meshed bones.

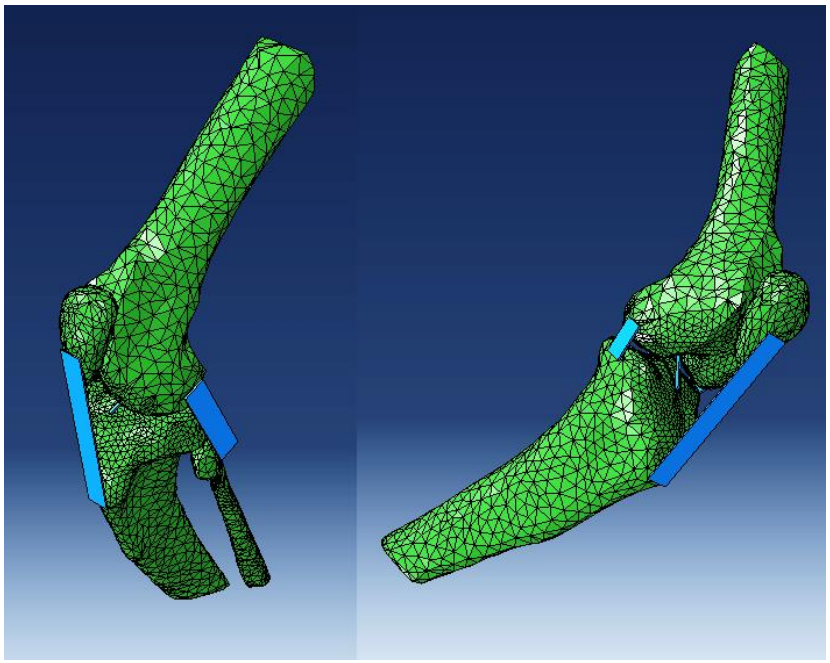

Figure 41: Simplified geometries of the MCL, LCL, PCL ACL and patellar tendon, in their positions with the bones.

The method that has been used to generate geometries of the ligaments and patellar tendon only results in the lengths at neutral joint position, which is 120˚ for the feline knee joint. The actual resting lengths of the structures are likely to be shorter than these, since ligaments are rarely in a stress-less state [96, 114]. Exceptions to this would be in the ACL and PCL, where at flexion the PCL would relax to its resting length and at extension the ACL would reach its resting length. Since we do not have scans of the knee joint in either flexion or extension, it is not possible to determine the resting lengths of these ligaments so it is not possible to include this behaviour in the model.

3.3.2.2 Properties and meshing

All the ligament geometries were meshed using hexahedral elements, to achieve a smooth mesh. Ligaments display nonlinear, anisotropic mechanical behaviour. Though it is known that the properties of ligaments can vary depending on their location, they have been assumed to be generalised in this case, as there are no detailed descriptions of any of the ligaments' properties in the feline knee joint specifically.

Abaqus allows the user to implement a range of nonlinear material models. The hyperelastic Holzapfel-Gasser-Ogden (HGO) model [117, 118] has been used for this model, as it displays the directional behaviour due to differently orientated fibres. This model allows for the compressive property that ligaments display; they will not display strain, and will buckle, during compression loads. This model is popular in the modelling of muscles, in particular those of artery walls, though a model has been developed for ligaments using a method motivated by the HGO model [119].

Though there are more detailed methods for modelling the behaviour of ligaments, as summarised previously in this chapter, these may not be required for a model which is developed for testing the relationship between joint movement and neural response. The generalised form of the HGO model is shown in equation (48) below [117, 120]. This version of the model is extended from the original Holzapfel model [120], which focussed consisted on the first and third terms where the isotropic, non-collagenous part of the tissue, and the anisotropic behaviour of collagen fibres are defined respectively.

$$U = C_{10}(\bar{I}_1 - 3) + \frac{1}{D}\left(\frac{(J^{el})^2}{2} - \ln J^{el}\right) + \frac{k_1}{2k_2}\sum_{\alpha=1}^{N}\{\exp[k_2\langle\bar{E}_\alpha\rangle^2] - 1\}, \quad (49)$$

with $\bar{E}_\alpha = f(\kappa, \bar{I}_1)$, where U is the strain energy per unit of reference volume; C_{10}, D, k_1, k_2, and κ are temperature-dependent material parameters (see Table 11); N is the number of families of fibres ($N \leq 3$); $\bar{I}_1$ is the first deviatoric strain invariant; and J^{el} is the elastic volume ratio. The elastic volume ratio defines how the volume changes during loading, and is equal to 1 for incompressible behaviour. The parameter κ, ranging between 0 and 1/3, describes the level of dispersion in the collagen fibre directions, where $\kappa = 0$ represents the fibres being perfectly aligned, and $\kappa = 1/3$ represents the fibres being randomly dispersed resulting in isotropic behaviour. A basic assumption of this model is that the fibres can support tension only; they would buckle under compressive loading. This is enforced by the $\langle \bar{E}_\alpha \rangle$ term, where $\langle . \rangle$ is defined as $\langle \bar{E}_\alpha \rangle = \frac{1}{2}(|\bar{E}_\alpha| + \bar{E}_\alpha)$, hence the anisotropic contribution of the strain energy function appears only when the strain of the fibres is positive.

Parameters	Value
C_{10}	10
D	0
k_1	345
k_2	345
κ	0.33

Table 11: Parameters for the Holzapfel model, to define ligament behaviour, adapted from parameters in ABAQUS examples [117].

Here, $\kappa = 1/3$ so that the ligaments in the FE model have isotropic behaviour and will buckle under compressive loading. This allows the general behaviour of ligaments to be captured, while maintaining the simplicity required for using the same properties for all ligaments in the model. The values for these parameters have been set to give stress-strain plots matching those of the Rhesus monkey [93], which is of a similar size to the cat. D represents the bulk modulus, which is set to 0 for incompressible behaviour; the volume of the material does not change. This assumption is made as the ligament has very little compressibility compared to its shear flexibility [117].

As an example of the behaviour displayed by this material model, the average stress experienced by the ACL during compression and extension of $2mm$ is shown in Figure 42. This shows that minimal stress is taken by the material during compression, however on stretching it is experiences tensile stresses. In this figure, the small number of sample points results in the curve appearing to be piece-wise linear; the behaviour of the model is actually a smooth curve.

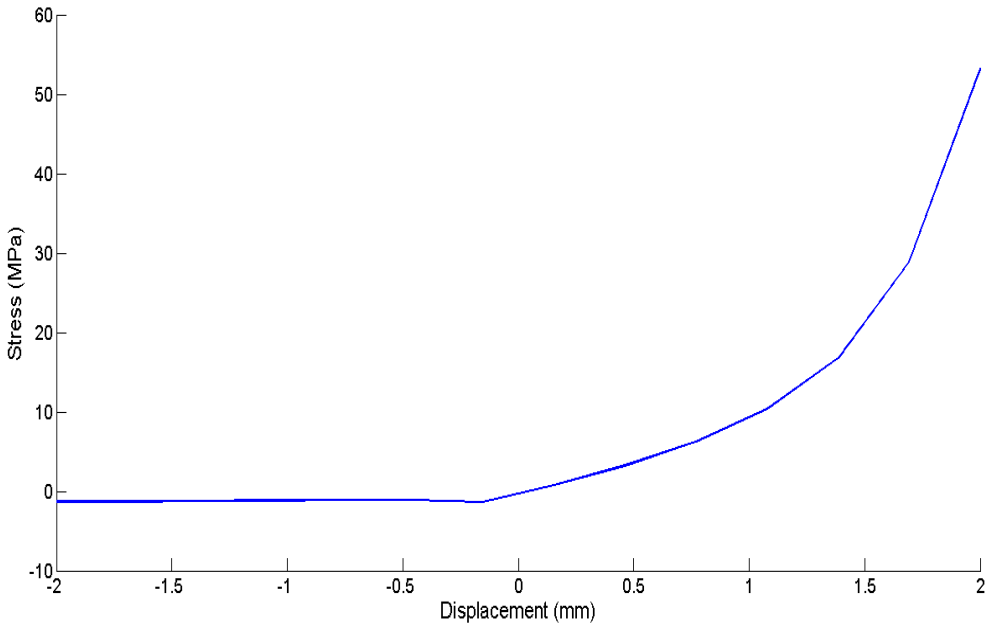

Figure 42: ACL behaviour to compression and tension of 2mm in both directions, with material properties defined by the HGO model, using parameters defined previously.

As already summarised, there are no stiffness properties specific to the ligaments in the feline knee joint; however properties of the ligaments of the Rhesus monkey, which is only slightly larger than the cat, have been published to be 194 ± 28kN/m [93]. Noyes and Grood [93] suggest that the stiffness of ligaments increases as the specimen decreases in size, with stiffness of the larger human ACLs being 129-182kN/m. The stiffness of ACL when using the previously described material properties is 250kN/m, so matches the trend suggested by Noyes and Grood [93]. Wilson et al. [121] report that there is no significant difference between stiffness of MCL and LCL, even though their geometries and strength are very different. This suggests that any differences observed between the behaviour of ligaments could be more due to their geometries than their tissue properties. For simplicity of the model in this study, all ligaments have been assumed to have the same tissue properties.

3.3.2.3 Interactions

Attachment of ligaments to bones around the knee joint is made up of thickening of fibrous tissues. The method for fixing the ligaments to bone in the FE model uses the penalty friction surface-to-surface contact[7], using a coefficient of friction of 0.8 and contact pressure factor of 10. This method for attachment allows the loads to be transferred to the section of the ligament that is aligned with bone, thus avoiding the stress from being unrealistically high at the attachment sites.

3.3.3 Fat Pad

As described previously, the fat pad is found behind the patellar ligament and acts as a shock absorber in the knee to protect the bones. When the segmentation process of MRI scans was used to build the geometry of fat pad, the structure does match the images seen in literature [63], however was not smooth enough for clean meshing due to the coarse MRI scans. For this reason a simplified geometry has been created in ABAQUS, similar to how the ligament geometries were done. This structure can be seen in Figure 43, below. Although this is not the typical shape of fat pads in the knee joint, it has anatomical dimensions from the scans, so should provide the shock absorbing effect satisfactory. The geometry still fits the description of having its largest part in the centre, and smaller at the top and bottom [63].

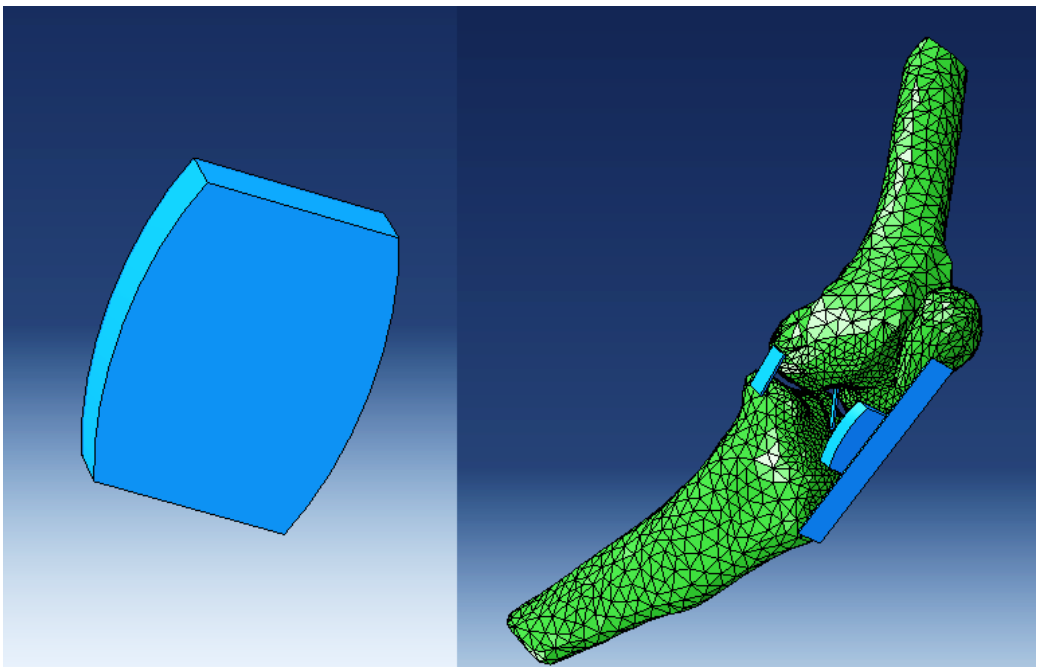

Figure 43: The simplified fat pad geometry on its own (left) and as part of the full model (right).

[7] As advised by Clare Fitzpatrick, Research Scientist in the Department of Mechanical and Materials Engineering at the University of Denver.

The geometry is meshed using hexahedral elements, as the ligaments were, using the ABAQUS meshing tools. The current methods for modelling fat pads are summarised previously in this chapter. For simplicity, isotropic linear elastic materials are chosen here; with $E = 150kPa$, and $\nu = 0.49$ [63] which are the properties specifically relating to the Hoffa's fat pad in the knee joint.

Anatomically, the fat pad is described to be attached to the patella, patellar tendon, the menisci, and anterior capsule [122]. These attachments maintain the fat pad's location in the knee joint, not allowing it to migrate into the cavity between the femur and tibia. In the knee model, tie constraints have been applied between the fat pad and the tibia. Penalty contact was also defined between the fat pad and patella, as well as patellar tendon. The penalty contact was frictionless, allowing tangential movement between fat pad and patellar tendon. Separation was not allowed ensuring the fat pad remains anterior in the joint. These constraints allowed the fat pad to move and deform slightly, following the tibia as the knee joint changes position. It maintained enough rigidity to avoid the fat pad gaining momentum, or moving to unrealistic locations within the knee.

3.3.4 Joint Capsule

3.3.4.1 Geometry

The joint capsule is a thin, membrane structure that surrounds the knee joint and includes the collateral ligaments and patellar ligament. These ligaments are thickenings of the capsule [13], though anatomy textbooks will often imply them to be separate structures. Due to these features, it was the most difficult geometry to build in the model of the knee joint. A simplified structure of the joint capsule was built with the use of the design software, AutoCAD. Curves from the CT and MRI scans were selected, so that the capsule will fit the femur and tibia at attachment sites, see Figure 44. A shell geometry was then created using the lofting tool.

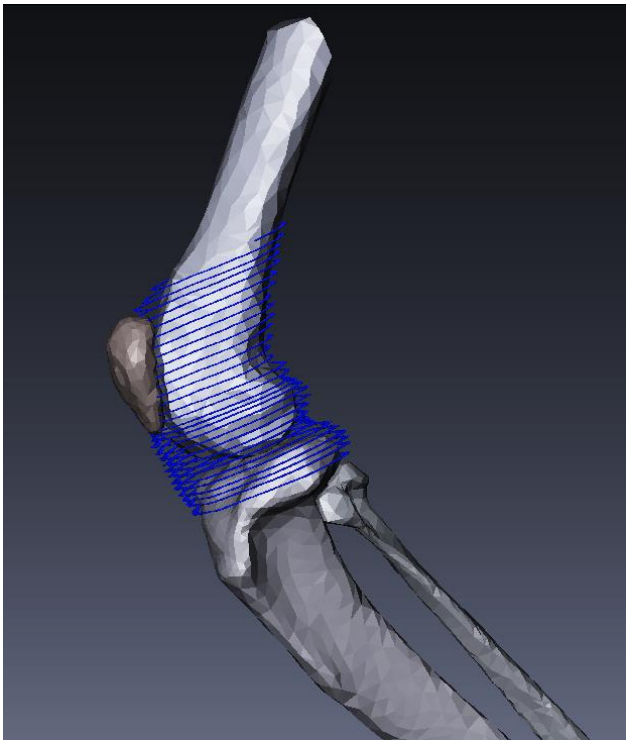

Figure 44: Curves representing the joint capsule, from CT and MRI scans. Blue lines represent the capsule geometry, as segmented from MRI scans.

The resulting geometry was imported into Abaqus, and the patella, patellar ligament, lateral collateral, and medial collateral ligaments geometries used to cut the capsule. Finally, tie constraints were applied between capsule edges and the three ligaments. The geometry that has been developed is shown in Figure 45, which shows the cut capsule with the ligaments. This figure shows that the patella is sticking through the capsule, which is also seen in Figure 44. Though this is not an ideal situation, the boundaries of capsule are controlled using penalty contact with the patella.

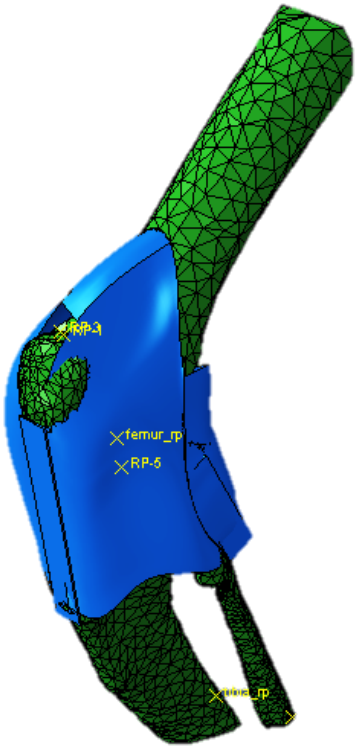

Figure 45: The joint capsule geometry, built based on the curves from previous figure, after cutting with the ligament geometries.

3.3.4.2 Properties and meshing

As already stated, the joint capsule is a very thin, membrane structure, so the geometry has been meshed using membrane, quadrilateral elements. Membrane elements allow some of the capsule behaviour to be captured, such as being unable to resist a compression load. In the case of the model, this results in a buckling or wrinkling effect of the capsule. In reality, the joint capsule is probably in a stressed state when the joint is in neutral position, and will shrink when the tension is removed; for example the posterior capsule would shrink during flexion. However, as with development of the ligament geometries, we do not know the shape or size of the joint capsule when it is fully at rest so have not been able to apply this behaviour to the model. Since the mechanoreceptors in the joint capsule respond specifically to tensile strains, i.e. the Ruffini endings and Nociceptors, it is unlikely that the behaviour of the capsule under compression will have a great effect on the global neural response. Figure 46 shows the meshed structure.

The remaining behaviour of the joint capsule is assumed to be linear elastic. Hoffman et al. [42] describe the joint capsule to have bands of different stiffness levels; with the lowest stiffness at the bottom, and the highest at the top where it attaches to the femur. However, this description is only valid for the posterior knee capsule and does not include any dimensions of the different regions. Therefore, for this model the capsules properties are simplified to be isotropic, with Young's modulus of 1MPa and Poisson's ratio of 0.49.

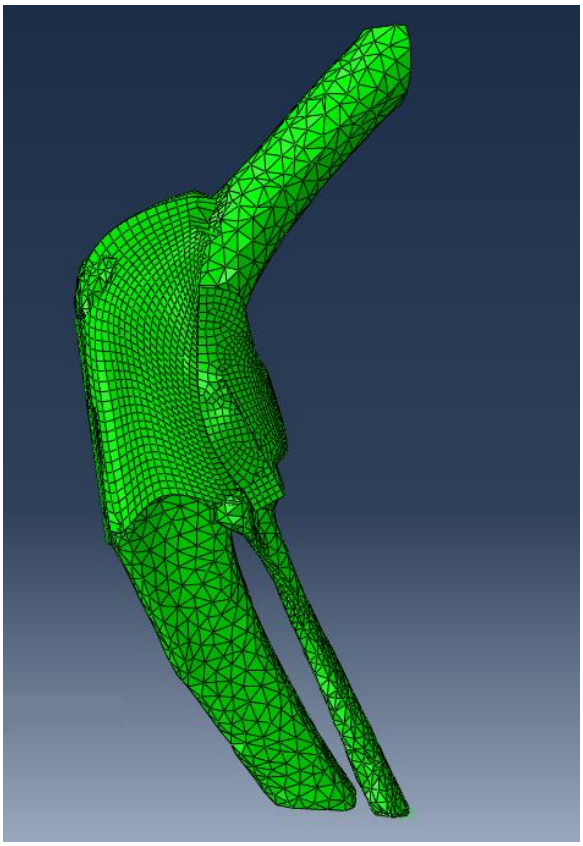

Figure 46: The entire joint, including the meshed capsule, consisting of linear quadrilateral elements.

3.3.4.3 Interactions

Similar to the attachment sites of ligaments to bone, the capsule fixes to bone through fibrous thickening of the capsule. For the model, to attach the capsule to the femur, tibia and fibular, tie constraints were applied to the nodes on each surface to ensure a strong fixation. This method can result in unrealistically high deformation of a small number of elements close to the attachment site. To avoid this extreme deformation, frictionless contact was defined between capsule and bones, helping to distribute the loads over the capsule.

As already mentioned, the MCL, LCL and patellar ligament are thickenings of the capsule. This is represented through cutting the capsule geometry with the relevant ligaments, and applying tie constraints between the cut edges of the capsule and the ligaments. Though this added further difficulty to the model, through more interactions between structures, it ensures that the knee joint will not be over-constrained from having both capsule and ligaments taking loads.

3.4 Testing the Finite Element Model

When the FE model of a feline knee joint was run for the applied boundary conditions described previously for maximum flexion and extension (page 79), the images in Figure 47, below, are achieved.

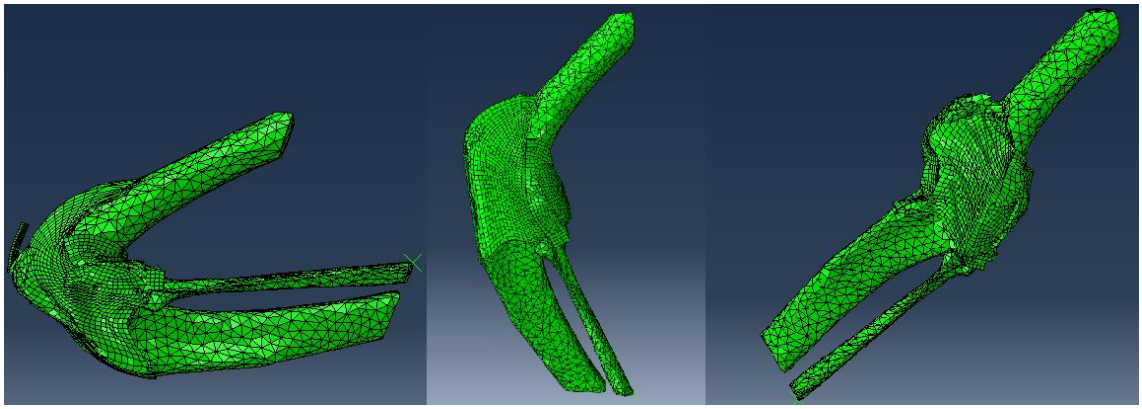

Figure 47: The complete feline knee FE model for flexed (left image), neutral (middle image), and extended (right image) positions.

The FE model of feline knee joint has been developed for use with the neural models, developed in chapter 2 previously, so that a global neural response to changes in knee positions can be predicted. Before this model is combined with the neural models, it must be tested for accuracy to ensure that it does satisfactorily represent the behaviour of a feline knee joint. Unfortunately, there is far less literature available for the behaviour of the feline knee joint than the human knee. However, it is possible to test its behaviour qualitatively. One paper available to us is that of Grigg [39].

Grigg [39] fixed the femur of an anesthetised cat, and recorded the neural response in the posterior articular nerve (PAN) to changes in knee joint position. This paper also reports the torques required for obtaining joint angle changes in both flexion and extension. A plot showing this relationship can be seen in Figure 48. This plot suggests that for changes in joint angles during range of motion for walking or running, around 70-150 degrees, very

low torque levels are required. However, to achieve the more extreme angles of flexion and extension, for example those involved in landing, much higher torques are required. If the relationship in Figure 48 is simplified to assume three separate linear lines, gradients of 100, 0 and -100g.cm/deg can be achieved for the joint angle ranges of 30-75 degrees, 75-150 degrees, and 150-180 degrees respectively. If the FE model predicts this behaviour, we can assume that the properties and constraints that have been applied are acceptable.

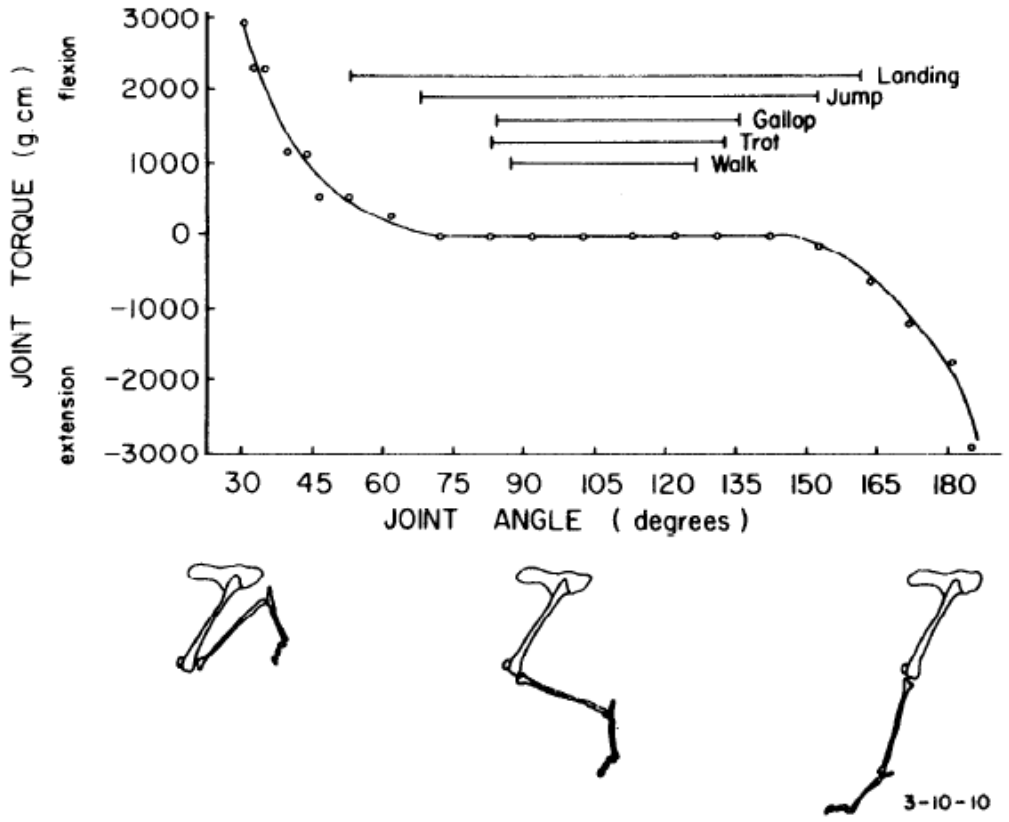

Figure 48: Torque-angle function for passive displacements of the feline knee joint. The curve represents the amount of torque required to maintain the associated joint angle, as published by Grigg [39], after section of the quadriceps tendon.

Figure 49 shows the reaction moments predicted by the FE model of a feline knee joint, when the tibia is moved through full range of flexion and extension. Though the absolute values of predicted moments are a little low, the general relationship matches that of Grigg, with the moments at extreme flexion and extension being of in the right range. The model that has been developed captures the behaviour of the feline knee joint to a satisfactory level. The range of angles for which no torque changes are required for the

model is around 80-150 degrees, which matches the experimental relationship in Figure 48. Also, when the slopes at either end of the curves are compared, the slope during flexion of the model matches the slope reported by Grigg [39] at around 100g.cm/deg. However, the slope during extension is lower than the slope of Grigg [39], at around 50g.cm/deg compared with the 100g.cm/deg of Grigg [39]. This behaviour suggests that the knee joint model is less constrained during the extension movements than the knee is in the experiments. This could be due to some structures not being included in the model, such as the popliteus muscle and tendon which are believed to be involved in resisting hyper extension of the knee joint.

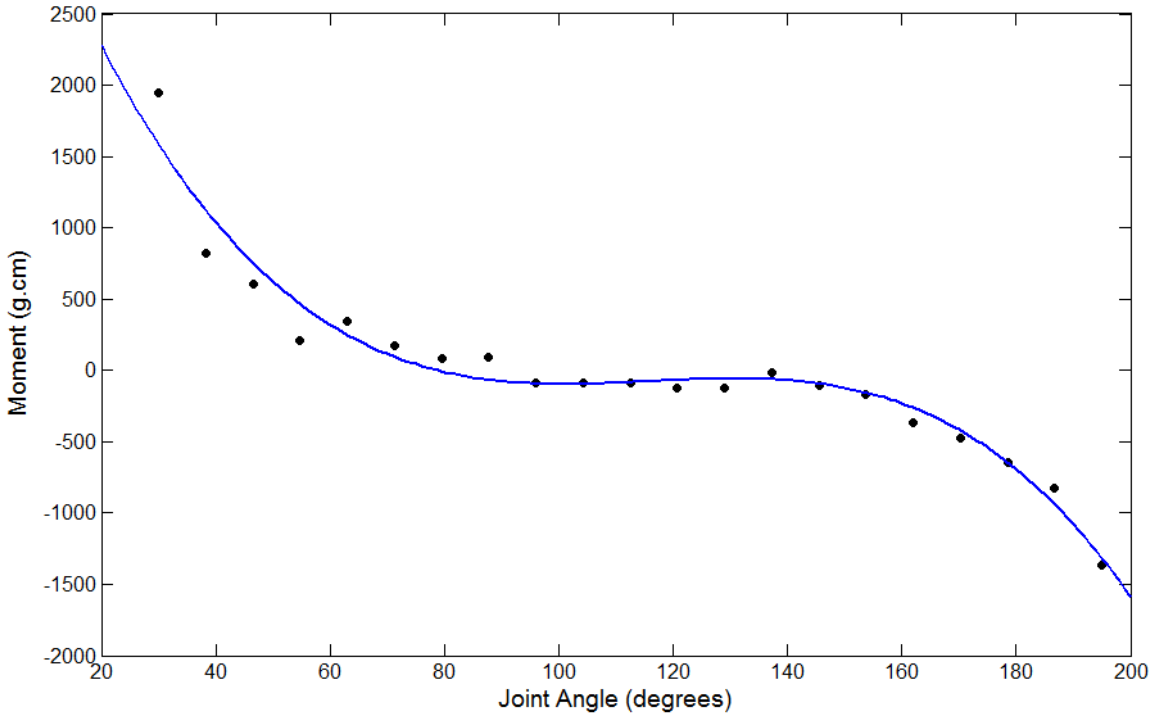

Figure 49: Reaction moments during flexion and extension of knee model. Black points represent the output moments from the model, and the blue line represents a 3rd degree polynomial fitted to the data, fitted using cftool in MATLAB.

3.5 Discussion

In this chapter, a FE model of a feline knee joint has been developed to a level that is ready for linking with the four neural models, developed in chapter 2 previously. Both CT and MRI scans have been used to build the geometries of bones, ligaments, capsule, and fat pad. The bones were built through segmentation of CT scans, while the soft tissue geometries were simplified, with the dimensions obtained from MRIs. As summarised in

the previous section of this chapter, the knee model behaves satisfactorily and produces a torque-angle relationship similar to that reported by Grigg [39].

Although the model that has been developed here uses common methodologies in the area of biomechanical engineering and orthopaedics [108, 109], it has a number of novel aspects, for example this is the first FE model of a feline knee joint. The inclusion of joint capsule and fat pads to a finite element model of a knee joint is also new. These structures are usually not included in this type of model, as they do not necessarily provide stability, which is often the primary motive for the models. However they are highly innervated, thus were required to be present in our study.

As already highlighted, a number of simplifications have been used in the development of the model. One of these simplifications is in the geometries used for the model. Usually soft tissue geometries are built using segmentation methods from MRI scans, however in this case the MRI scans were too coarse to build geometries for satisfactory meshing. This meant that the geometries had to be simplified and built in ABAQUS. Since the dimensions of the soft tissues were used from the MRIs, this simplification should not affect the behaviour of the model as a whole.

One aspect of ligament behaviour that has not been mentioned in this chapter, but should be discussed, is that they are rarely in a stress-less state [96, 114]. They generally will experience a pre-stress; however it is unknown what magnitude this may be. Since there is great uncertainty in this area, it has not been included in the model. This is an improvement that could benefit the model in the future, as it would allow the strains to be more accurate. Currently, however, the model focusses on the general changes in strain experienced by soft tissues due to changes in joint angle. Including a pre-stress would be likely to change the magnitude of these strains, rather than the relationship between joint position and strain.

The joint capsule is a novel addition to the FE knee joint model, however there are aspects that have not been included in this model. For example, the capsule contains synovial fluid in the joint, which inevitably applies an outward pressure to the tissue. Outward pressures of around $0.0023 Nmm^2$ have been reported to be experienced by the capsule of human knee joint [123, 124]. However, there are no examples of the pressures experienced by the feline knee joint capsule specifically, and it is unknown whether it is uniformly distributed around the joint. Also during flexion and extension, the synovial fluid moves around the

knee joint which could result in changes in the pressure experienced by the capsule, and it has been shown that joint angle can affect the intra-articular joint pressure in the canine knee joint [77]. Although the pressure was not included in the model for this reason, this is likely to have resulted in the predicted deformation of the joint capsule to differ from what would happen in reality. For example, during the flexion-extension movement, the model predicts a high occurrence of wrinkling of the joint capsule, which may not happen with the presence of an outward pressure, meaning the predicted strains could be different.

When the knee joint is at maximum flexion (left image in Figure 47, page 88), the patella is causing extreme local deformation of the joint capsule. This could have caused excessive strains at these areas, as well as strains that are too low at other locations of the capsule. Improvement of the capsule's behaviour could involve more accurate geometry development, through using finer MRI scans, or through using graduated tissue properties for the joint capsule. The joint capsule could also be defined to be stiffer around the patella, and other bone attachment sites, and gradually become less stiff in the parts of capsule further away from bones.

Though verification of the model's behaviour during flexion and extension has been possible with use of data from Grigg [39], where the torque versus joint angle relationship for the feline knee joint was published, ideally a more thorough testing of the FE model would have been carried out. Due to a lack of experimental data relating to the mechanics of the feline knee joint, it was not possible to further validate the model's behaviour in this study. Data that would have been useful in the testing of the general behaviour of the feline knee joint model include the force/displacement relationship during anterior tibial drawer, and the torque/angle relationship during internal and external rotation. Another testing method that would be useful in testing the model is comparing strains experienced by each structure during a range of movements. This would both test the properties and the attachment methods of the structures in the model, and perhaps help to identify resting lengths or pre-strains that are experienced.

Even with the previously described simplifications and limitations of the FE feline knee joint model, it has been possible to show that the model produces a similar torque/joint angle relationship to that of the feline knee joint in the literature [39] during flexion and extension. The model shows a similar shaped curve, with no changes in torque over the angle range of 70-150 degrees, which increases to around 2000g.cm during flexion, and decreases to around -1500g.cm during extension. Although the maximum and minimum

torques are not the same as those reported by Grigg [39], they are of a similar magnitude, and are likely to be related to the soft tissue properties which are known to vary greatly even within species. Since the behaviour of the model is similar to the experimental data of the feline knee [39], it has been accepted that the model is at a satisfactory level for linking with the neural models. This process, along with results, is described in the following chapters.

Chapter 4

Integrating Knee Model with Neural Models

4.1 Introduction

This chapter describes the process of combining the finite element model of a feline knee joint developed in chapter 3, and the four nerve ending models developed in chapter 2. How this is related to the rest of the project is indicated in Figure 50. Experimental data describing global neural responses to changes in knee joint positions is summarised in this chapter, along with descriptions of the distribution and locations of nerve endings in the feline knee joint. Methods for combining multiple neural signals are then discussed, and predictions for global neural responses are compared with the literature [39, 91].

The purpose of this project is to use a computational model determine whether the knee joint receptors are likely to play a proprioceptive role, as opinions in the literature are split (see chapter 1). Proprioception itself can be split into two types; conscious and unconscious. Conscious proprioception is where the neural signals are processed in the cerebrum, and unconscious proprioception is where the signals are processed either in the cerebellum or spinal cord. These two types of proprioception would require different communication paths, however there are no detailed descriptions of which, if any, of the nerves of the knee joint are involved in conscious or unconscious proprioception. For this reason, we have considered only the neural response before the spinal cord is reached.

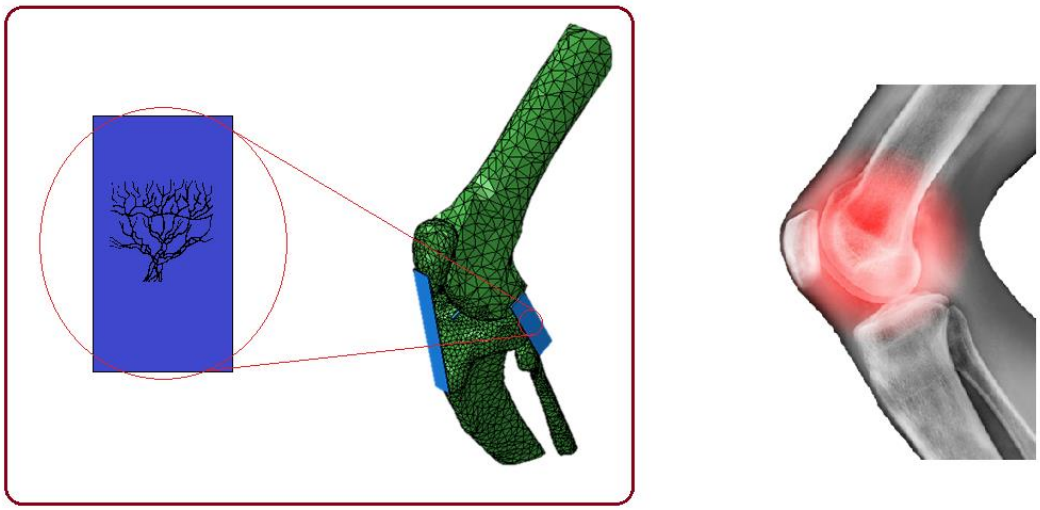

Figure 50: A flowchart to indicate how the work in this chapter is related to the rest of the project.

4.2 Literature Review

In this section the innervation around the feline knee joint is described, both in its arrangement and behaviour. Previously, in chapter 2, the individual nerve endings and their response at the knee joint were discussed in detail so this has not been repeated here. It is the global innervation of the knee joint that is of interest in this chapter; how the endings are distributed, and the changes in neural response from a nerve, relating to movement of the joint.

The knee joint is served by two types of articular nerve; primary and accessory. Primary nerves include the Posterior, Medial and Lateral articular nerves (PAN, MAN, and LAN, respectively), and they innervate most structures in the knee. Accessory nerves arise from muscular nerves, however the number of fibres in these nerves are negligible in comparison to the primary articular nerves [17], and there are no descriptions of recordings from these nerves, so they are not discussed further. The primary nerves consist of a bundle of nerve fibres; the numbers of fibres reported present in PAN and MAN are summarised in Table 12. The PAN is thickest, and mostly innervates the posterior capsule, along with the posterior fat pads and posterior cruciate ligament (PCL) [17]. The MAN is finer, and supplies the medial aspects of the capsule, the medial collateral ligament (MCL), patellar ligament and fat pad [17]. The LAN innervates the lateral parts of the knee

joint such as the lateral collateral ligament (LCL), and is reported less frequently than the PAN and MAN, possibly due to its variable nature [17].

Since both myelinated and unmyelinated nerve fibres are reported in Table 12, separation of the type of mechanoreceptor that the fibre may lead to is possible, since the only receptors that can arise from an unmyelinated fibre is the Nociceptor. Also, since a single mechanoreceptor generally arises from a nerve fibre [17], it can be assumed that the number of fibres in a primary nerve is equivalent to the number of mechanoreceptors in the knee joint.

	Posterior Articular Nerve			**Medial Articular Nerve**		
	Total number of fibres	Myelinated fibres	Un-myelinated fibres	Total number of fibres	Myelinated fibres	Un-myelinated fibres
Gardner [52]	286	171	115	266	144	122
Skoglund [23]	-	176	-	-	145	-
Freeman & Wyke [17]	387	224	162	291	157	131

Table 12: Composition of primary articular nerves to the knee joint, table adapted from Freeman and Wyke [17]. The values represent the mean number of fibres.

The general method used for recording a global neural signal involves dissecting the relevant nerve from an anaesthetised mammal [23, 25, 39]. The dissected nerve is then immersed in a paraffin bath, and the action potentials led through silver wire electrodes to be amplified and recorded using a cathode follower [23]. To ensure the mechanosensors in the knee joint are stimulated in a meaningful manner, the joint must be secured so that only the desired movements will occur [39]. Often the hip and femur are fixed, and the tibia moved through the required range or motion using a stepping motor. It is then possible to record the neural response to both normal and painful positioning of the knee. As described in chapter 3, the neutral position for a cat is around 120˚, and the normal range of motion for flexion and extension is between 30˚ and 195˚ [91]. Painful positions of the knee can be assumed to be those outside of this normal range of motion.

Global response is measured from the entire nerve, rather than the individual fibres that relate to a single nerve ending. When recording from the entire nerve, the frequencies are far higher than those of individual fibres [39]. The signal recorded from the primary nerve is a combination of all individual fibre signals, and no processing method for obtaining this combined signal is described [16, 39, 91]. In general, the frequency of the global discharge from the PAN and MAN has been shown to increase in response to both flexion and extension in the knee joint [16, 23, 39, 91]. Figure 51 and Figure 52 both display the changes in neural response from the PAN to changes in feline knee joint position.

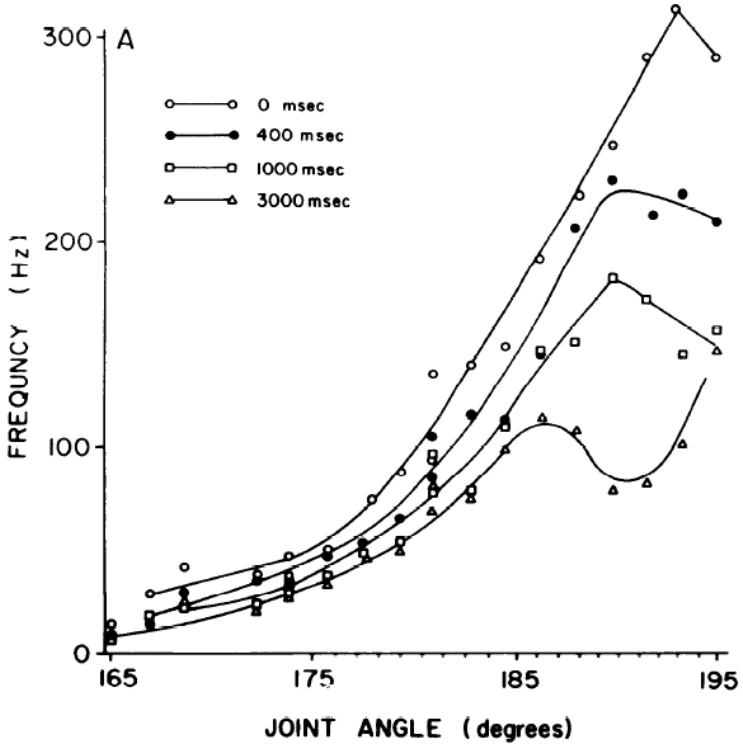

Figure 51: Rate of neural discharge recorded from PAN versus joint angle during extension of the feline knee joint, as published by Grigg [39]. The instantaneous frequency was recorded at 0, 400, 1000, and 3000msec after the required joint angle was reached. The joint positions were reached at an angular velocity of around 30-40˚sec, and held for 10 seconds or longer.

The plot in Figure 51 shows the neural response to normal flexion of the feline knee joint, from a starting position of 165˚ [39]. This indicates the increase in response as the knee reaches its maximum joint angle. The four lines represent the recordings at different times after joint position had changed; the response decreases with time. This suggests that the mechanoreceptors in the tissues are adapting to the applied stimulus. Since an increase in neural response is seen during normal range of motion, it is likely that these nerve endings are involved in proprioception and not only painful stimuli.

Figure 52 shows the neural response of the PAN to both flexion and extension of the feline knee joint as published by Ferrell [91]. Though the maximum angles are not reached, it is still clear that there is an increase in neural response for both flexion and extension, with the minimum response recorded at neutral position. Maximum responses recorded here are during knee extension, with flexion giving responses of almost half the frequency. However, Ferrell [91] highlights that this behaviour is only demonstrated by half of the cats. He indicates that some cats (25%) displayed maximum responses to knee flexion, and others (25%) did not display the mid-range dip in neural response. This is an example of the highly variable nature of neural and biological systems.

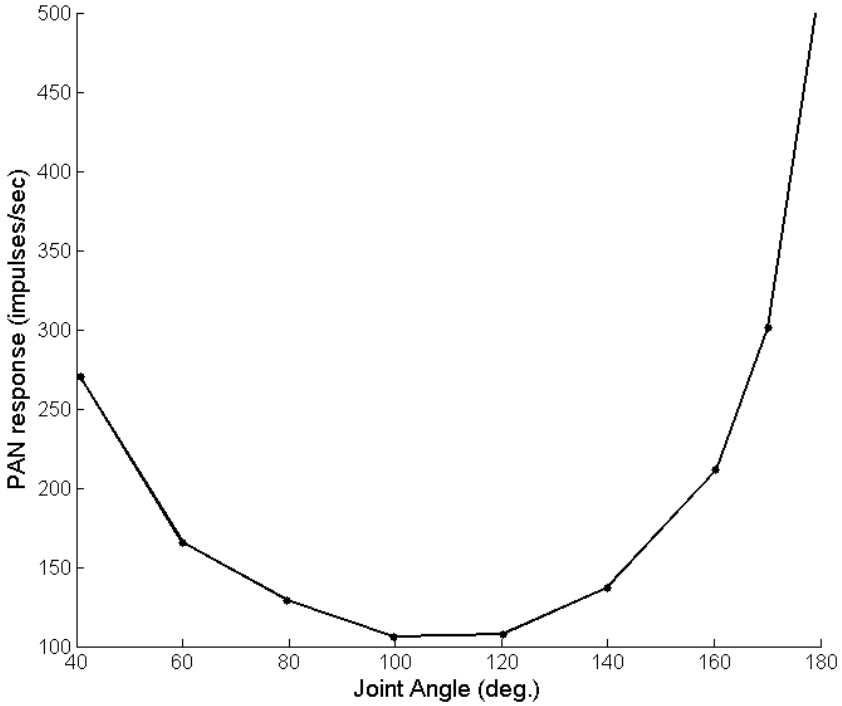

Figure 52: Reproduced from Ferrell [91], integrated PAN discharge pattern. Each point represents the adapted PAN discharge with the limb held stationary at successive angles, over the flexion-extension range.

Though there are limited studies describing the neural activity at the knee joint, there are some detailed descriptions of the effects of both joint position and joint damage on neural activity. All of these reports are focussed on the feline knee joint, along with the descriptions of the innervation of the knee joint [17, 23]. This lends itself to direct application of nerve fibre numbers to the computational model, and direct comparison between experimental data and the response from the model for satisfactory validation.

4.3 Distribution of Nerve Endings

In the previous section, the numbers of nerve fibres in the PAN and MAN have been summarised (Table 12, page 97). From the content of Table 12, and the qualitative descriptions of ending locations through the knee joint [17, 23, 28, 31, 36], we have been able to estimate how the fibres are distributed. As already mentioned, in general nerve fibres result in a single mechanoreceptor [8, 17], so it has been assumed in this project that the number of nerve fibres is equivalent to the number of mechanoreceptors in the knee joint. Though this is not always the case, with reports of the Ruffini ending sometimes occurring in twos or threes from the same nerve fibre [23], these are not consistent with other studies [17, 52], so the assumption that one mechanoreceptor arises from each nerve fibre is reasonable.

Freeman and Wyke [17] provide the most detailed description of innervation of the feline knee joint, including the indicating structures that are innervated by each of the three primary nerves. The PAN is said to innervate the medial and lateral posterior parts of the capsule and the posterior cruciate ligament. The MAN innervates the medial and antero-medial parts of the capsule, the medial collateral ligament, patellar ligament and anterior fat pad. The LAN innervates the lateral collateral ligament and the lateral part of the joint capsule. Though the primary articular nerves are described to innervate specific structures [17], these are variable, and can result in multiple nerves innervating the same structures.

Table 13 shows the distributions of nerve endings, for each primary articular nerve, in each soft tissue structure in the feline knee that have been assumed for this project, based on the descriptions by Freeman and Wyke [17]. These distributions are based on the numbers of fibres and quantitative descriptions of the structures that they innervate [17]. Since the number of fibres in the LAN has not been reported, it has been assumed to be less than 200.

Table 13: Distributions of nerve endings, based on qualitative descriptions [17] and the number of nerve fibres summarised in Table 12.

	Ruffini Ending			Golgi Tendon Organ			Nociceptor			Paciniform Corpuscle		
	PAN	MAN	LAN	PAN	MAN	LAN	PAN	MAN	LAN	PAN	MAN	LAN
Capsule	70	30	-	-	-	-	150 (posterior)	20 (antero-medial)	20 (antero-lateral)	5	5	-
Fat Pad	-	-	-	-	-	-	-	70	-	-	10	-
Patellar Ligament	-	20	-	-	6	-	-	50	-	-	-	-
Anterior Cruciate Ligament	-	-	-	-	-	6	-	-	15	-	-	-
Posterior Cruciate Ligament	-	-	-	6	-	-	30	-	-	-	-	-
Medial Collateral Ligament	-	20	-	-	6	-	-	50	-	-	-	-
Lateral Collateral Ligament	-	-	20	-	-	6	-	-	15	-	-	-

Now that the distribution of nerve endings has been determined for each soft tissue structure in the knee joint, it is possible to select their locations on the finite element model of a knee joint. As already stated, the exact locations of nerve endings are not reported for the feline knee joint. It is understood, though, that these locations are likely to differ greatly between specimens. For example, the study conducted by Khalsa et al [21] reports the locations of Ruffini endings in samples of joint capsule, seen in Figure 53. Although there is a higher incidence of mechanoreceptors found in the left half of the sample, the locations otherwise appear to have no correlation. It is therefore assumed that the mechanoreceptor location in the knee joint is random, except for the Golgi Tendon Organ, which is mostly found at the ends of ligaments [17].

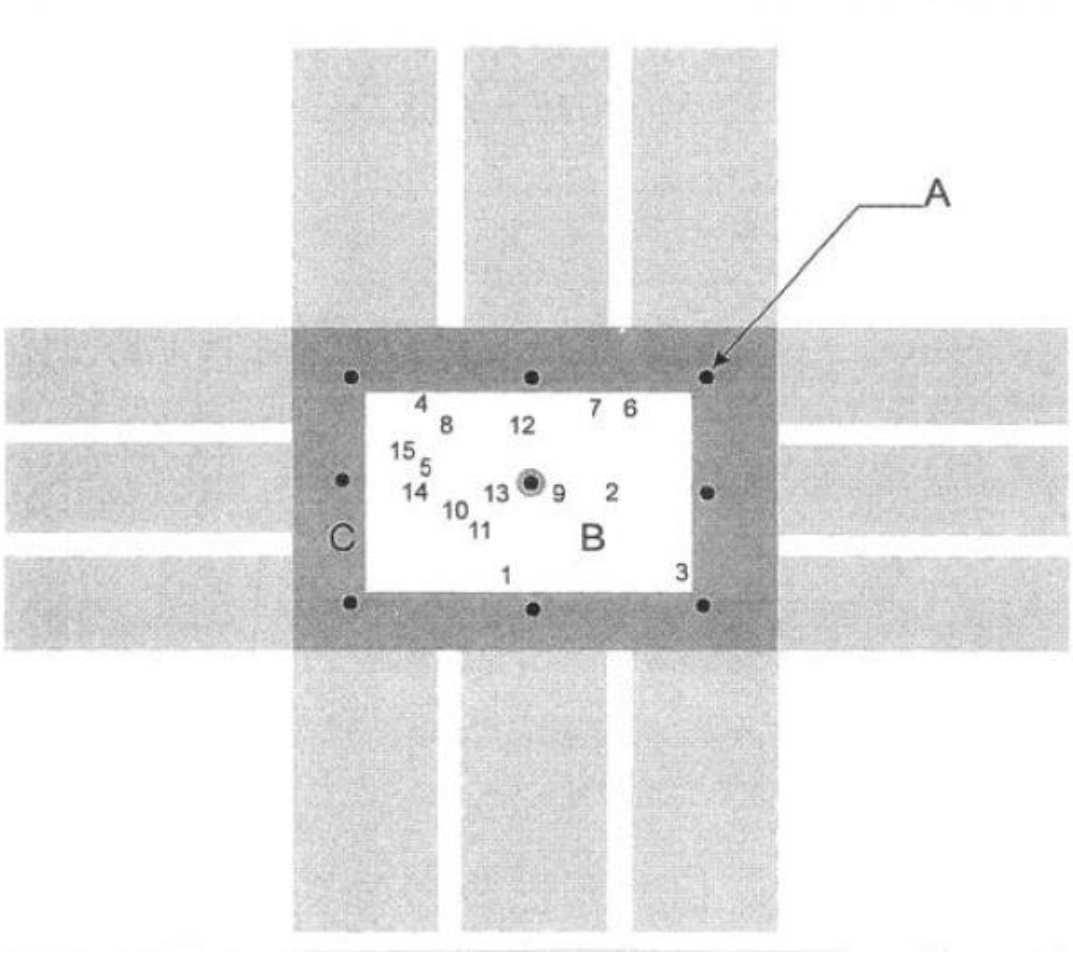

Figure 53: Relative locations of 15 Ruffini endings from 11 samples of feline joint capsule. The light grey lines are the tabs to which loading apparatus was applied. Figure from Khalsa et al [21].

The nerve ending models developed in chapter 2 previously require strains as input, so the strains at the relevant locations must be acquired. To obtain these, there are two main techniques in ABAQUS; nodal strains and element strains. For the first of these, a node set could be created, where each node represents a mechanoreceptor. This technique assumes that the mechanoreceptor is only present at a point, with no physical dimensions. For element strains, an element set is created, and the strain experienced by the mechanoreceptor is the strain at the centroid point of the element. The displacements and stresses experienced by the nodes are extrapolated from the integration points of the elements. In this model, as described in the previous chapter, membrane and hexahedral elements are used. For these types of elements, the integration points are the same as the centroid points due to a reduced integration method that is implemented by Abaqus/Explicit. The ligament and fat pad 3D elements contain linear interpolation functions, while the membrane elements of the joint capsule contain quadratic interpolation functions. This could mean that the strains calculated at the centroid of the elements may be more accurate than the strains at the nodes.

Of these two methods, the elements technique has been used for this model, as it more closely matches reality and should result in more accurate strain calculations. Although mechanoreceptors can have a size of only 100μm [17], their receptive field area can be up to 2-3mm [36]. The receptive field area of a mechanoreceptor is the distance from the cell body a stimulus can be while still resulting in an action potential response. Although the elements in the finite element model are often larger than 2-3mm, it is accepted that the element sizes represent the receptive field area.

Element sets were created, to represent each of the mechanoreceptor types for each primary articular nerve, in each soft tissue structure. The number of elements in each element set was equal, where possible, to the numbers indicated in Table 13. This was not possible in all cases, as the mesh of PCL contained fewer elements than assigned nerve fibres. In these cases, all elements were selected, however this was not expected to affect the results significantly as the structure was only short of ten elements. The element sets were selected manually in Abaqus/CAE, with random distribution across structures, except for the Golgi Tendon Organ element sets, which were selected only at the ligament ends. The strains experienced by these elements throughout the time step were then saved, ready for input to the relevant nerve ending model in MATLAB. An example of the strains output by the knee model is shown in Figure 54, where each line represents the

strain experienced by a single mechanoreceptor during extension. This shows that the majority of the higher strains were in the capsule and MCL, and that minimal strains were experienced by the fat pad and patellar tendon. The strains in the MCL change the most during knee extension, which is sensible as this structure is known to be engaged during the movement, to avoid hyperextension [125].

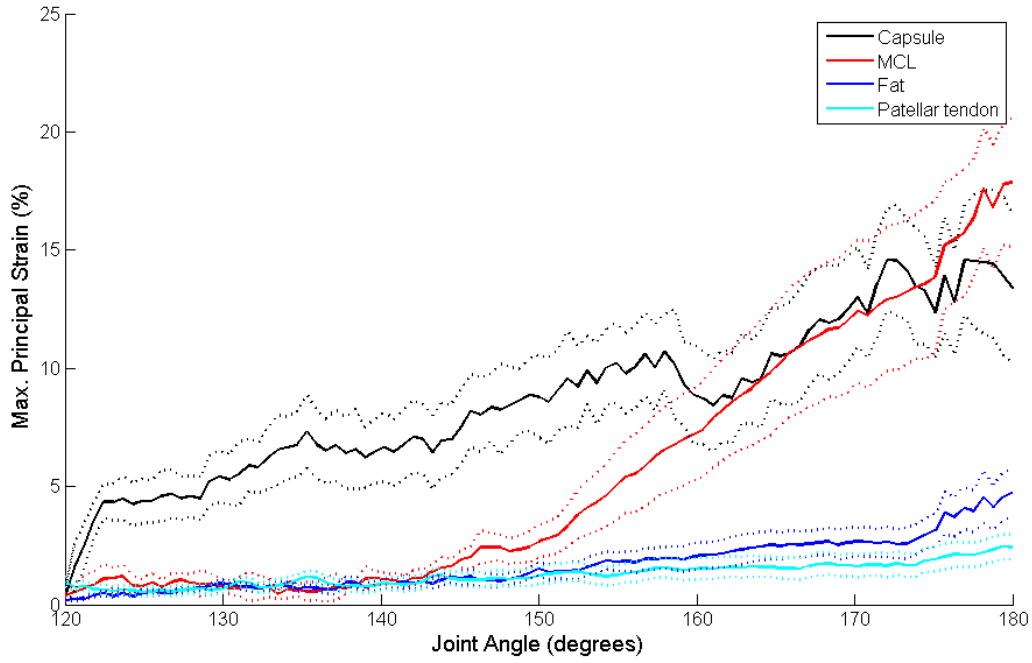

Figure 54: The mean and 95% confidence intervals of the local maximum principal strains experienced by each Nociceptor of the MAN, during extension of the knee joint. Black lines represent the capsule strains, red lines represent the MCL strains, blue lines represent the fat pad strains, and light blue lines represent the patellar tendon strains.

4.4 Signal Combination

After obtaining the local strains of the relevant element sets, they were input to the four neural models; Ruffini, Golgi, Paciniform, and Nociceptor. This resulted in a neural frequency for each nerve ending. Though the local responses are of interest, it is the global neural response that is required for comparison with experimental data. As described previously, the neural responses to position changes in the knee joint are reported as a single value that represents neural frequency. The recordings taken from the major nerves such as PAN, however, would have been a combination of the signals from multiple nerve cells. It is not known exactly how these signals were combined, so some assumptions have been made, which are discussed in this section.

There are a number of factors that should be considered while determining the best method for combining the individual neural response to calculate a global response. One of these is the fact that neural signals can deteriorate over distance during their transmission, which could change the resulting neural frequency. These deteriorations are mostly in the amplitude of the electrical signal, so the frequencies are not lost [8], and are minimal so that signals in healthy nerve fibres will not be adversely affected. Another factor is that nerves are known to have branching structures from single axons, which could result in a change in the overall signal. For sensory neurons, however, these may be discounted as issues, since each fibre only connects to a single mechanoreceptor [8], and the distances that are being considered in this project are relatively short, when compared with the distances some axons cover in the body.

The method that would have been used by Grigg [39] and Ferrell [91] to measure the global neuronal response at the knee joint involved measuring the number of action potentials at a point on the PAN in a set period of time. This method means that the authors would not have known specifically which type of nerve ending was signalling, or which structures they originated from. In the absence of evidence suggesting otherwise, summation is the method that more closely represents the procedure followed during the experimental recordings. Since the experimental data available to us from the literature consists of only the global neural frequency, in impulses/second, in response to changes in joint position this is the characteristic from the neural models that has been focussed on. Although we are able to determine the action potential magnitudes from the models, this characteristic is less related to the stimulus strength, and less reported experimentally so is not of as much use as the frequency.

Figure 55 shows the predicted global neural response to flexion and extension, using summation of the individual frequencies. To produce this movement in the FE model, the femur is fully constrained, and a rotational displacement applied to the tibia from its neutral position to either the full flexion position or the full extension position in a time. The displacements were applied over a time of 0.01 seconds, to achieve a low running time, and the element strains calculated at 100 points during the movement. The plot in Figure 55 shows a similar relationship between the joint angle and neural response to that reported by Ferrell [91]; lowest response at the neutral position, an increase with both flexion and extension, and the highest response at maximum extension. The neural responses in Figure 55 are to a larger range of motion than those reported by Ferrell [91].

However, at the comparable angles, the predicted responses are similar; at neutral position (120˚) responses of around 100impulses/second are predicted, at flexion angle of around 40˚ responses of around 350impulses/second are predicted, and at extension angle of around 160˚ responses of around 500impulses/second are predicted.

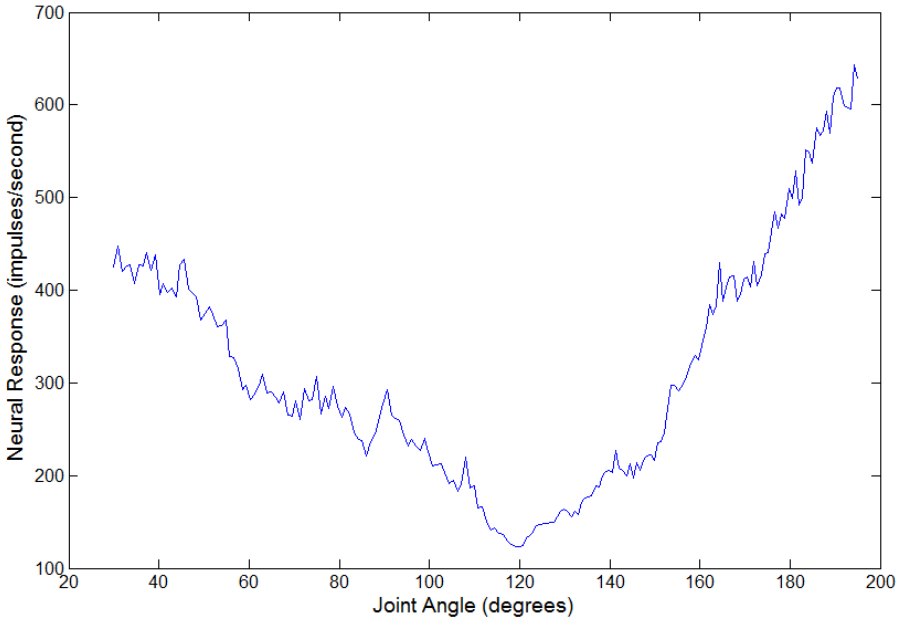

Figure 55: The predicted global neural response of the PAN to changes in joint angle during the complete flexion-extension movement, using summation method of individual neural frequencies.

Another area that must be considered is how noise and base level frequencies are included. Even with no stimulus, the nerve ending models have a low frequency of around 0.5 to 1 Hz. Though this may not have any impact at low numbers of nerve endings, when the whole knee is considered there are hundreds of endings. This can result in a base level frequency of 100-200 Hz. Some papers report neural responses along these lines at neutral joint angles [91], which suggests that the authors have not normalised the responses. In other papers, however, the global neural response is far lower [16, 39], suggesting that there is some form of reduction of noise recording is made. The responses reported by Gomez-Barrena et al. [16], for example, have been set to zero at 90˚. This should not affect the overall change of neural response, only the magnitude, so the model that has been developed in this study has kept the base level frequency.

4.5 Verification of Model

The response of the completed model could now be compared with the published data available to us. This data consists of a global neuronal recording from the PAN of an anaesthetised cat for a range of knee positions. One of the more detailed descriptions of the neural response of PAN to flexion and extension is that from Ferrell [91], see Figure 52, page 99. This displays a U-shaped curve relationship between joint angle and neural response, with the lowest frequency being recorded at around 120˚, neutral position, and the highest response at joint extension. The plot in Figure 55 (page 106) indicates that the model predicts realistic neural behaviour, through giving a similar curve of a similar magnitude to that seen in the literature [91]. Before observing how the developed model responds to removal of soft tissues, it is important to check for robustness while the knee is intact.

Ten different element sets were created within the finite element knee model, before the simulations were run. It has been assumed that the nerve ending locations vary between knees, while maintaining the same numbers. For each of the element sets, the nerve ending locations were selected randomly by hand, while ensuring there was a wide variation in locations between the different element set. This allowed observation of how the results differ with changed nerve distributions, representing differences that may be seen between different feline knee joints. For the PCL, which had fewer elements than mechanoreceptors, the same element locations were used throughout the simulations, to avoid losing more of the PCL contribution to the global response. Although there is a known variation of mechanoreceptor numbers between cats [17], they were maintained constant between simulations, as it was the changes in location that were of greater interest; these were initially random, due to a lack of information suggesting otherwise.

The following plots show the mean and standard errors of neural responses for PAN, MAN and LAN respectively. These plots suggest that the neural responses of PAN and MAN are less affected by changes in locations of nerve endings than the responses of LAN, especially at the more extreme angles.

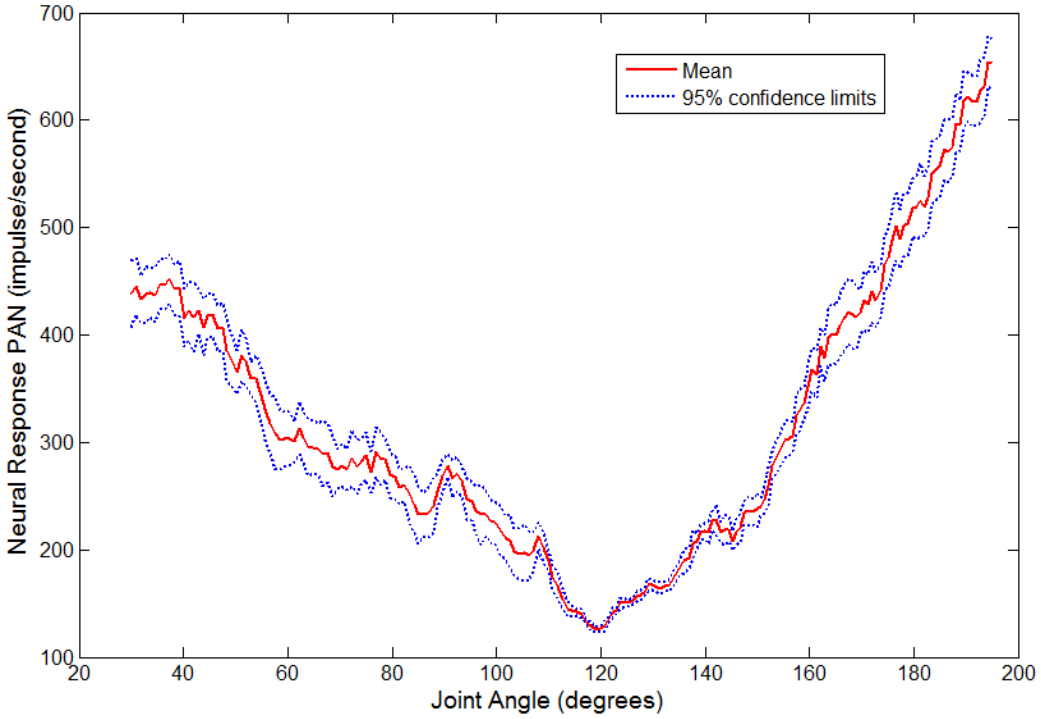

Figure 56: The mean and standard error of predicted neural responses of the PAN to knee flexion and extension, from ten simulations with different nerve locations.

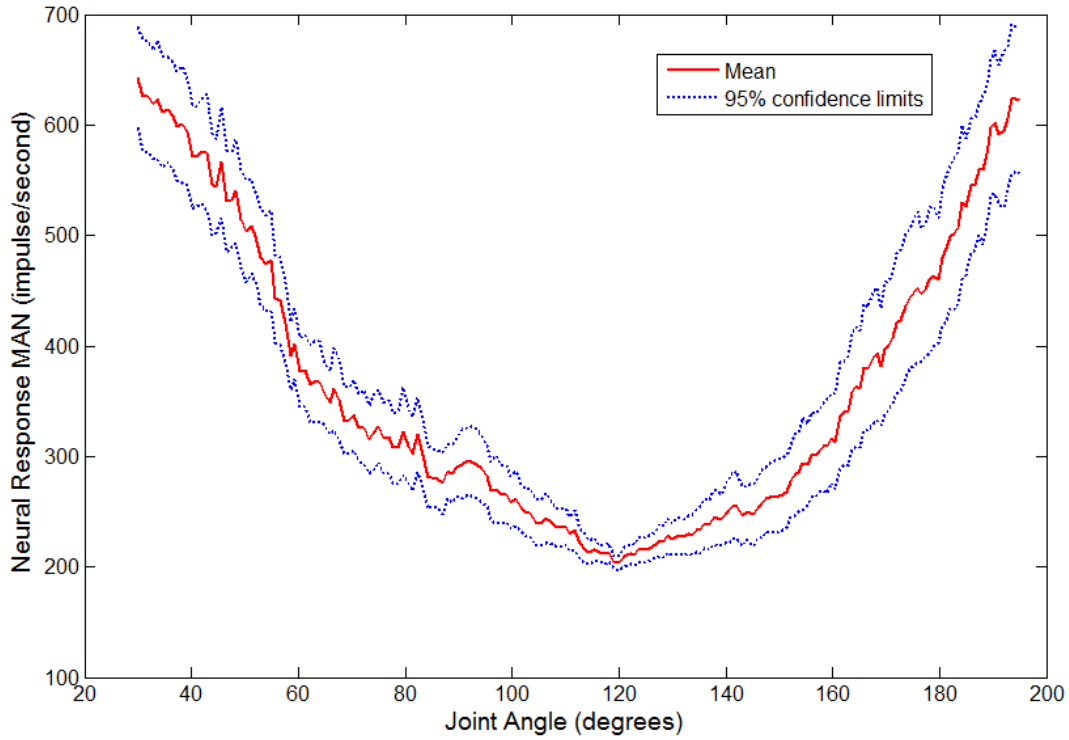

Figure 57: The mean and standard error of predicted neural responses of the MAN to knee flexion and extension, from ten simulations with different nerve locations.

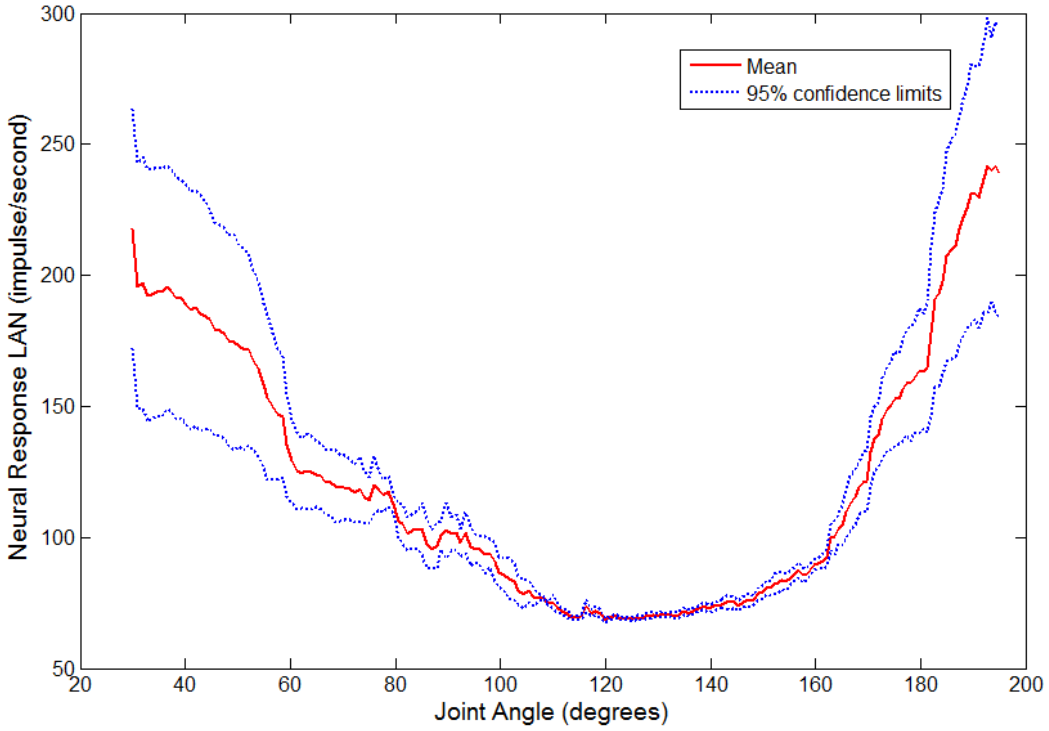

Figure 58: The mean and standard error of predicted neural responses of the LAN to knee flexion and extension, from ten simulations with different nerve locations.

In all of the plots, the general shape is comparable and the lowest variability in each primary nerve appears at the neutral positions; between 100˚ and 140˚. This is likely to be due to the lower strains throughout the knee joint at these angles, while at flexion and extension a different location of ending would result in a different strain, thus the related nerve endings threshold may not be reached until a higher joint angle. A larger variation in the neural responses with nerve ending location is observed in the LAN than the other two primary nerves. This is likely to be due to the far lower numbers of fibres in the LAN, making it more sensitive to relatively small changes. However, it has been accepted that the variability seen in these plots are at an acceptable level, and that the nerve ending locations does not affect the global neural behaviour considerably.

The beauty of the model that has been developed is that it is possible to break the global neural response to the contributing structures and nerve ending types; a process that is not possible with current experimental methods. The following plots show the predicted neural response of the PAN, broken down to the contributing structures and mechanoreceptor type.

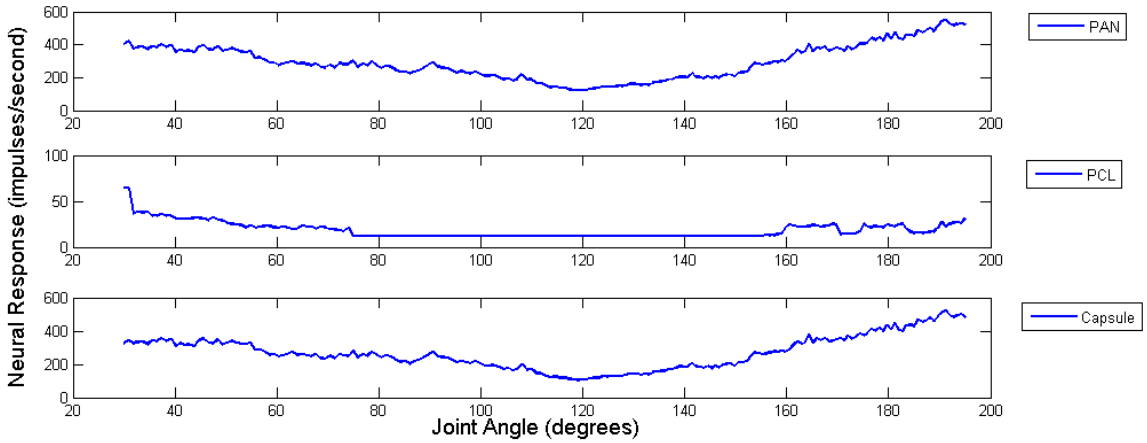

Figure 59: Predicted neural response of the PAN to joint flexion and extension, along with the individual structure contributions to the global response.

Figure 59 indicates that PCL only contributes to the response as the joint angle reaches higher flexion angles; this is likely to be due to the high density of Nociceptors in this structure. The largest contribution to the PAN response is the joint capsule. This structure has the highest population of nerve endings out of all structures in the model, consisting of both Ruffini endings and Nociceptors. Although the joint capsule is not involved in stabilisation of the knee joint, it is a highly innervated structure [17, 21, 22]. It has been suggested that this high level of innervation could be related to the joint capsule playing a large role in proprioception of the knee joint [31, 126, 127]. Boyd and Roberts [31] highlight that the sensory organs of the PAN that respond to normal knee joint motion are mainly from the posterior joint capsule.

Figure 60 shows the neural response of the PAN, with the four mechanoreceptor contributions. Here it can be seen that the strongest contribution to the PAN neural response is from the Ruffini endings. This is not surprising, as they largely populate the joint capsule; the structure that dominates the neural response of PAN. The Nociceptors show very little change in neural response until the joint reaches the higher extension angles, when the response increases. Very little change in Nociceptor response is shown during flexion. Although the model has more Nociceptors (150 endings) present in the posterior joint capsule than the Ruffini ending (70 endings), it has a far lesser impact on the global neural response during the movement. Since the Nociceptor is a pain sensing mechanoreceptor that responds to potential or actual damage to its local environment [60], this behaviour is as would be expected in the feline knee joint. The Golgi Tendon

Organ response is considerably lower than that of the Ruffini ending; this is most likely to be due to there being far fewer Golgi Tendon Organs contributing to the neural response of the PAN. Finally, the Paciniform corpuscle also contributes a low neural response to the PAN. This is likely to be due to the fact that there are very few of these mechanoreceptors in the knee joint [23], and that they respond to strain rates and vibration stimuli.

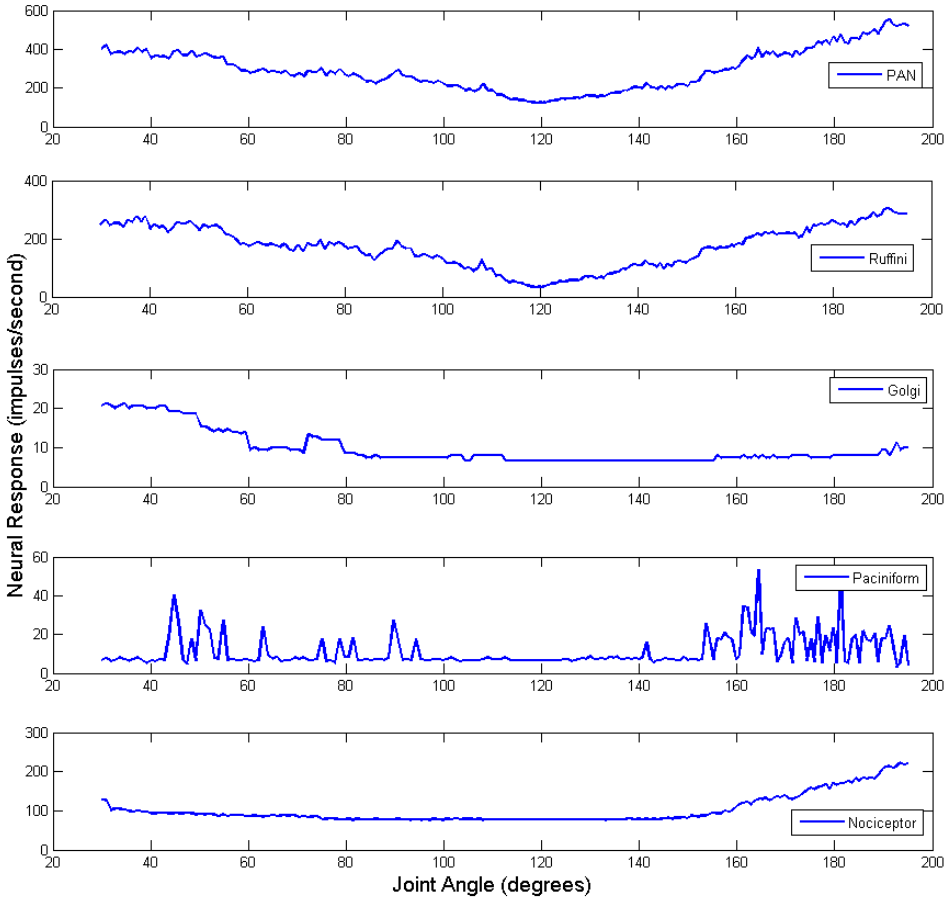

Figure 60: The predicted neural response of the PAN to joint flexion and extension, along with the contributions from each nerve ending type.

There is less literature on the neural response of the MAN, and even less on the response of the LAN; however the following plots show the structural contributions to predicted MAN and LAN neural response to flexion and extension. Figure 61 shows the structure contributions to the MAN neural response during this movement. The MCL clearly has the strongest influence over the global response, with both their shape and magnitudes being similar. The patellar tendon, capsule and fat pad do not appear to contribute to the shape of the response of MAN, though their base level responses would contribute to the overall magnitude of the global response.

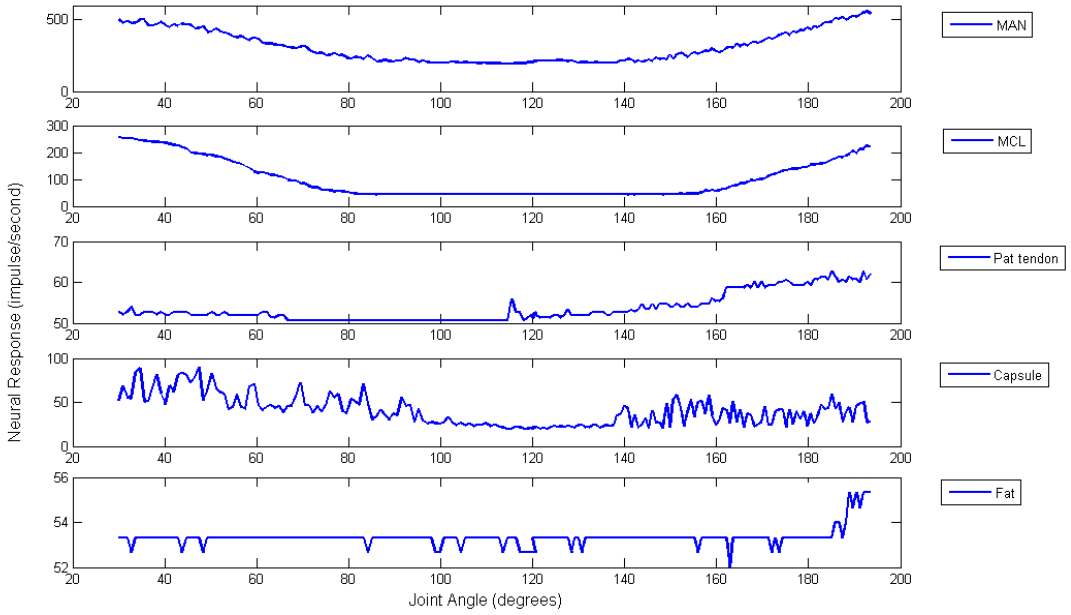

Figure 61: The predicted neural response of the MAN to joint flexion and extension, along with the individual structure contributions to the global response.

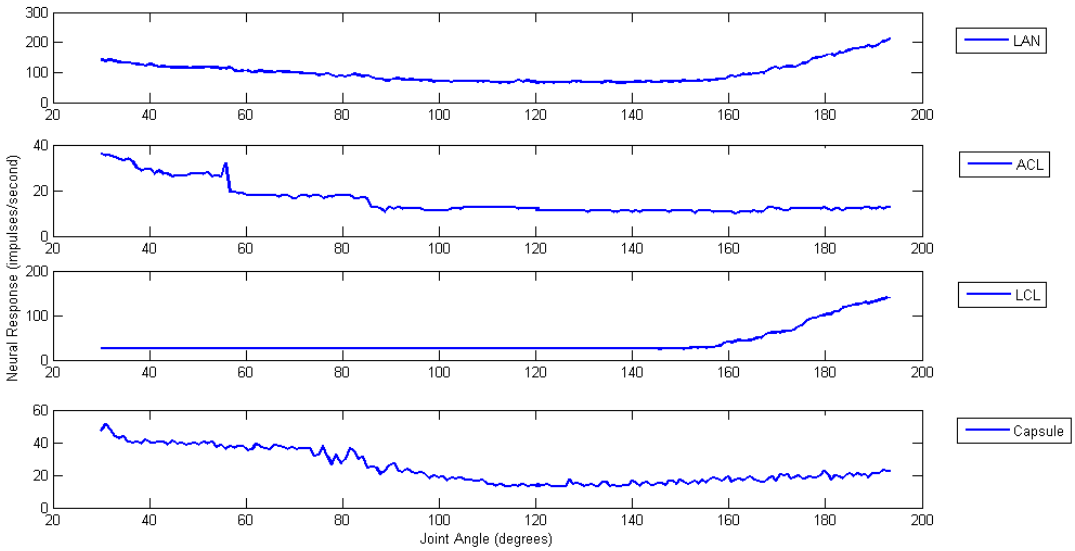

Figure 62: The predicted neural response of LAN to joint flexion and extension, along with the individual structure contributions to the global response.

Finally, Figure 62 shows the structure contributions to the neural response of LAN, and suggests that during flexion both the ACL and capsule contribute to the shape of the global response. The largest contribution to the LAN response, however, is that of the LCL which generates neural responses of over 100impulses/second. Though there is little literature on the neural responses of MAN and LAN, it makes sense that it is the collateral ligaments that dominate the global neural responses since they are the large structures.

4.6 Discussion

The model that has been developed through this thesis has been shown to be able to capture realistic neural response during flexion and extension of the feline knee joint. The predicted neural response of the PAN matches the response published by Ferrell [91]; a U-shaped curve, with the lowest frequency at the neutral position of around 120˚, and higher frequencies at both flexion and extension. The model is even able to predict correctly that the highest frequency occurs at the maximum extension position of the knee joint. The model could even be considered to have abilities that are advantageous over the experimental recordings; we are able to observe how the neural behaviour is broken down to either structural or mechanoreceptor type recordings. This is a process that is not possible with experimental methodologies.

When the global neural responses of the MAN, PAN and LAN were broken down to their structural contributors, there were certain structures that clearly contributed more than others. The MCL has the greatest effect on the MAN response, providing most of the shape and magnitude that was observed. This was also seen in the LCL contribution to the LAN response and the capsule contribution to PAN response. Since these are the structures that have the highest populations of mechanoreceptors, it makes sense that they have the largest effect of the global neural responses. The ACL and PCL are structures that are commonly believed to be involved in proprioception [14, 128], with reflexes involving the cruciate ligaments and surrounding muscles to avoid damage being reported. Though the model does predict changes in neural behaviour of both of these structures to flexion and extension, the magnitudes of their frequencies are far lower than the dominant structures (LCL, MCL and capsule). These lower frequencies are mainly due to the low population of mechanoreceptors in the cruciate ligaments, in comparison to the other structures [61], with the joint capsule having the largest population of mechanoreceptors [129].

In chapter 3 the presence of a pre-strain in the soft tissues around the knee joint was discussed, but not included in the model due to a lack of experimental data describing the magnitudes that would be expected. It must be understood here that through not including pre-strains, or a resting length for the soft tissues in the model, the magnitudes of the global neural responses that have been calculated in this chapter may have been affected. However, since it is mostly the changes in neural response during joint movements, and how they may be linked with proprioception, that are of interest to us the lack of pre-strains should not adversely affect any conclusions made in the following chapter.

With respect to the general mechanoreceptor populations in the feline knee joint, there is no detailed description of the innervation of the feline knee joint that includes the numbers of nerve endings for each of the major soft tissue structures. In the development of the model in this project it has been assumed that one nerve fibre results in one mechanoreceptor. This is justified in literature, as sensory endings are mostly described to originate from non-branching fibres [8, 17]. However this is not always the case, as some studies describe multiple mechanoreceptors branching from the same nerve fibre [34]. The numbers of nerve fibres have been reported for the PAN and MAN [17], and these were used in the construction of element sets representing mechanoreceptors in the feline knee joint. Though it is known that the numbers of fibres in PAN and MAN vary between cats [17], the effect of changes in nerve populations has not been tested in this study. It is believed, however, that so long as the proportions of endings in each structure remain fairly consistent, no drastic changes in the global behaviour should be observed.

Though the effect of variation in the numbers of mechanoreceptors on global neural response has not been tested, the effect of their locations has. Since the only descriptions of mechanoreceptor locations in the feline knee joint are vague, the locations in the model are random. To ensure this has not adversely influenced the results predicted by the model, the locations have been varied over ten different sets. The predictions of PAN and MAN results show very little changes as the mechanoreceptor locations are changed. The LAN predictions are more varied; however this nerve has contributions from fewer mechanoreceptors, so perhaps is more sensitive to location changes.

As described previously in this chapter, the methods used experimentally to record global neural responses are not clear. It is likely that they are summing that action potentials from all fibres in the primary nerve, however we do not know how the individual neural

responses interact with each other. The method used for combining all responses in the computational model is summation of the frequencies of each mechanoreceptor that contributes to the global response. This is a simple method, and in the absence of more information is a good first approximation of the processes that may be occurring experimentally.

It must be noted here that the neural response predicted by the model is of the pre-processed form of the neural response, before it reaches the spinal cord or brain. A higher level of processing is likely to occur later in the neural system that results in more directly relatable with conscious proprioception and nociception. Although the predictions from the model may match experimental recordings, they cannot be used to directly infer what the perception around the knee joint is. This has been discussed in more detail in the next chapter, where the neural responses at an unstable knee joint have been predicted.

When all neural frequencies are combined to obtain the global PAN, MAN and LAN responses, the minimum neural responses, at the neutral knee position, are still quite high. This is a combination of all mechanoreceptor types, since each model does not actually report a zero response, even when the threshold has not been reached. Though these frequencies are low, at around 0.7 impulses/second, when they are summed over tens of receptors the results can be substantial. For example, the base responses of the PAN, MAN, and LAN are around 100, 200, and 50 impulses/second, respectively. When the PAN response is broken down to the mechanoreceptor contributions, it is clear that most of the base response is from the Nociceptors. This is most likely to be due to the high population size of this type of mechanoreceptor in comparison to the others. Perhaps the higher level processing mentioned previously could involve suppressing any base level neural response, meaning the changes in neural responses are of more interest than the magnitudes.

The behaviour of the neural models could be adapted so that a zero response is in fact achieved when the stimulus has not reached the threshold of mechanoreceptors. However it is suggested in the literature that although the frequencies of Ruffini endings can be increased through applying tension, they could never be silenced [30]. This suggests that there is always a low level frequency from mechanoreceptors. Another reason that it may not be necessary to remove the base level responses is that experimental recordings show high initial frequencies at neutral positions of around 100 impulses/second [91]. Although

not all literature shows this [16, 39], an element of normalising responses at initial positions is suggested [16] which would result in lower base level frequencies.

When the global neural response of the PAN is broken into the four mechanoreceptors' contributions, the Ruffini endings dominate the response. This is likely to be because there is a higher occurrence of this type of ending than the Golgi or Paciniform, and the threshold of the Nociceptor is far higher, so it is sensible that this ending has a far stronger response throughout the flexion-extension movement. Literature suggests that Ruffini endings are involved in proprioception of the knee joint [128, 129]. Since the model predicts that these endings are responsive throughout normal joint movement, the suggestions in the literature can be confirmed.

It has already been mentioned that the Nociceptor response contributes greatly to the base level response of the PAN. The other contributions made by the Nociceptors are only as the knee reaches the higher angles of extension; from around 160°. This type of nerve ending should respond to painful or damaging stimuli. Since this angle is still considered to be within the normal range of motion of the feline knee joint [91], perhaps the Nociceptors are responding prematurely based on the relatively low pain threshold of 0.2MPa. To avoid this, the threshold of the ending could be increased; however to do this satisfactorily, experimental data would be required.

Another area that has not been considered is the existence of 'silent' Nociceptors, which have far higher thresholds than normal Nociceptors, and are believed make up a significant portion of the Nociceptors present at the knee joint [60]. For simplicity in the model for this thesis, all Nociceptors have been assumed to have the same threshold. Including 'silent' Nociceptors would likely to have resulted in a reduced Nociceptor contribution in the global response.

Both the Golgi tendon organs and Paciniform corpuscles have a far lower influence on the global neural response than the Ruffini endings and Nociceptors. This is because both of these have smaller population sizes in the joint. To have a larger impact on the response, perhaps there is some form of a weighting factor involved later in the processing stage of proprioception. Also, the Paciniform corpuscles are compression and vibration sensors, so perhaps they would be more likely to have a larger impact on global response if the joint capsule pressure were to be included in the knee joint model.

The main limitation in verification of the model is that the only available experimental recordings of the full flexion-extension movement are of the PAN, so this is the only response that can be directly compared with the model's predictions. However, it has been shown that generally higher responses are recorded from the MAN than the PAN [16]. This knowledge, and the fact that there are more mechanoreceptors contributing to the MAN, means that the difference between the predictions of the MAN and PAN can be accepted to be appropriate. The LAN has the fewest mechanoreceptors contributing to its response, so it is sensible that it has the lowest response of all three primary nerves.

This chapter has described the methods used for combining the neural models from chapter 2 and the knee joint model from chapter 3 to calculate changes in neural activity to movements in the knee joint. It has been shown that the predictions of neural responses from the computational model are comparable with published experimental data, where possible. This verification means that it was possible to use the model to predict the effect of damage to the knee joint on the neural response. These tests are described and discussed in chapter 5, comparing results with the literature.

Chapter 5

Effect of ACL Resection on Neural Response

5.1 Introduction

The initial motivation for this thesis is whether the receptors in the knee joint are involved in proprioception, as described in chapter 1. Damage of the anterior cruciate ligament (ACL) is a common sports injury, with approximately 200,000 ACL injuries occurring in the United States annually [130]. Tearing the ACL results in not only severe levels of pain, but stability and proprioception of the knee joint have been shown to reduce significantly [131]. Both proprioception and pain are subjective senses that rely on sensory nerve endings to provide relevant information on the state of the joint. This chapter describes how the model has been used to predict neural changes around the knee joint after the ACL has been removed, and how the results of this may indicate reasons for changes in pain and proprioception levels in patients with this injury. Figure 63 indicates how this chapter is related to the overall project, with the results from this chapter being the ultimate goal of the thesis since they will help us to understand whether the joint receptors at the knee are in fact involved in proprioception.

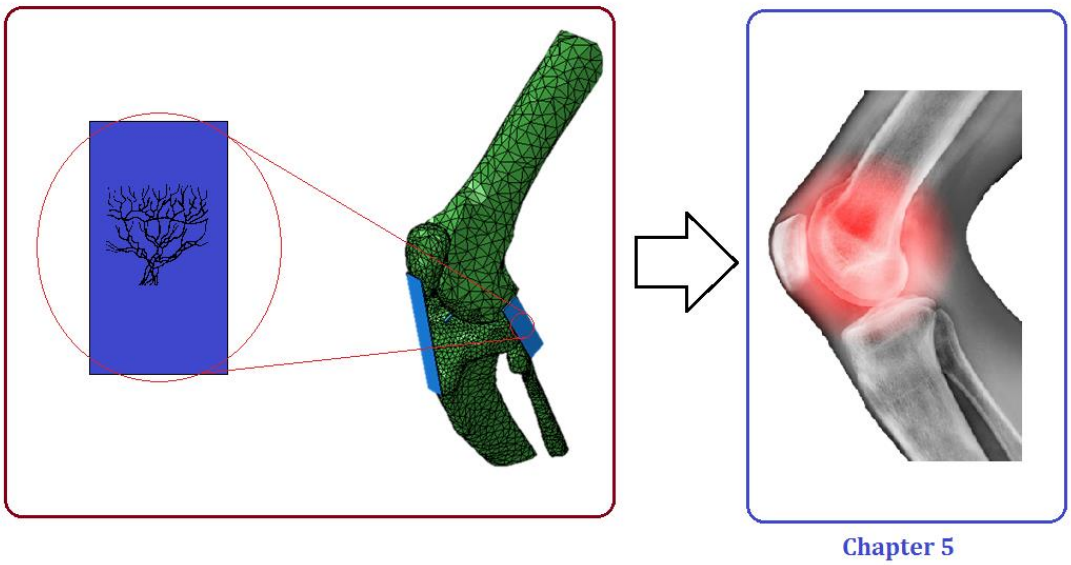

Figure 63: Flowchart to indicate how the work in this chapter is related to the overall project in this thesis.

The literature suggests that the removal of the ACL results in an increase in neural response to flexion and extension [16]. However, this could be counter-intuitive, as resection of a structure will result in less mechanoreceptors being present in the knee joint, thus it could be expected that the neural response would in fact decrease. It could be justified that on removal of the ACL, the remaining structures will experience a higher load, thus resulting in more mechanoreceptors reaching thresholds and generating electrical impulses. Another potential cause for the change in neural response is that the removal of the ACL would change the stability, and the way that the joint moves, resulting in different structures being stretched. As discussed in the previous section, it is possible to observe the different structures' contributions to predicted global neural response with this model. This could prove useful in determining what may be causing the changes seen in global responses due to instability in the knee joint.

5.2 Neural Effects of Loss of the ACL; Experimental Recordings

Gomez-Barrena et al. [16] investigated the effect of ligament damage on the global neural response at the knee joint to a range of passive joint movements. In particular, they observed the neural response changes from PAN and MAN after ACL transection. The authors performed three main movements on cat knees, before and after removing the ACL, to determine the neural changes. The movements were flexion-extension, anterior tibial drawer, and internal-external rotation. Significant increases in neural response were

reported for flexion, extension, anterior tibial displacement, summarised in Table 14, with the strongest changes recorded in the PAN during flexion.

	PAN	MAN
Flexion	↑[b]	↑[a]
Extension	NS	↑[b]
External rotation	NS	↑[b]
Internal rotation	NS	NS
Anterior tibial displacement (90˚ flexion)	NS	↑[b]

Table 14: Changes in the electrical activity recorded from the PAN and MAN after ACL transection from feline knee joints, as published by Gomez-Barrena [16]. [a] $p<0.05$, [b] $p<0.01$, NS not significant.

In their paper, Gomez-Barrena et al. [16] are unable to identify the causes of the observed neural changes after the ACL was removed. This is because they were limited to only recording the global neural responses of PAN and MAN, and could not break down the signals to the different structures or mechanoreceptors. They suggest that possible causes for the increased neural responses could have been from the collateral ligaments, capsule and medial meniscus experiencing higher loads; however they were unable to confirm this. Using the model developed in this thesis, it has been possible to predict the neural changes that may occur in all three primary nerves after removing the ACL. So that direct comparisons can be made with the literature, the same tests performed by Gomez-Barrena et al. [16] have been run with the model; the next section of this chapter describes the methods followed for this.

5.3 Methods

The tests that were performed to replicate the study of Gomez-Barrena et al. [16] are summarised in Table 15. To achieve the flexion-extension movement, the required rotational displacement was applied to the rigid body's reference point (Table 15). These are based on the normal range of motion of the feline knee joint [91], and were used in the verification processes in chapters 3 and 4. In this test, all degrees of freedom were unconstrained, except for the applied rotational displacement. When the ACL structure in

the model was removed and all related interactions suppressed, the same method for flexion and extension was applied.

For the anterior tibial drawer test, an applied force was used to achieve the correct movement. There is no literature describing the forces used in anterior tibial drawer tests for the feline knee joint, however forces of 80N have been described for the same test in the human knee joint [132]. Since the feline knee joint is smaller than the human knee, a lower force has been used (Table 15). The rotational degrees of freedom of the tibia were fixed, so that only the required movement was achieved, and an anterior force applied to the tibia's centre of mass. Before the anterior load was applied, the tibia was displaced to the correct flexion angle of 90˚, which was then held constant for the rest of the step. The same force was used for both the intact knee and the ACL deficient knee; a larger displacement in the latter knee was expected.

Finally, to produce internal or external rotation of the tibia, two opposing forces were applied to neighbouring nodes at the centre of mass of the tibia. Khalsa and Grigg [129] describe stiffness of knee joint in this test to be around 0.1Nm/rad. Though equivalent loads were not achieved in the model without excess deformation, the highest loads possible were used (Table 15). As with the anterior tibial displacement test, before the loads were applied the tibia was displaced to a flexion angle of 90˚, and held constant for the rest of the step. The other two rotational degrees of freedom were fixed for the entire step. Since both a force and a displacement was required to be applied to produce the internal/external and anterior tibial drawer tests, the step was split into two stages; during the first stage the displacement was applied to achieve the required flexion angle, and during the second stage the loads or torque were applied.

	Applied displacement (degrees)	Applied Load (Newtons)	Applied torque (Nm)
Maximum Flexion	90	-	-
Maximum Extension	-75	-	-
	STAGE 1	STAGE 2	
Anterior tibial drawer (at 90˚ flexion)	30	30	-
External rotation (at 90˚ flexion)	30	-	0.06
Internal rotation (at 90˚ flexion)	30	-	-0.04

Table 15: The maximum positions or forces applied to feline knee joint to achieve the required tests for replicating the tests performed by Gomez-Barrena et al. [16].

So that any significant difference between predicted neural responses before and after ACL removal can be determined, ten different groups of element sets are used. This represents ten different feline knees, assuming that the main variation between knees is the mechanoreceptor locations in each soft tissue structure. As already mentioned, it is predicted that removal of the ACL will result in an increase in neural response due to remaining structures taking the loads that would usually be taken by the ACL. The following chapters describe and discuss the results from the simulations that have been described in this section, and whether the prediction is proven true.

5.4 Results

The tests that were run by Gomez-Barrena et al. to determine changes in neural response, due to ACL resection, were flexion/extension, anterior tibial drawer, and internal/external rotation of the knee. This section of the chapter first shows the kinematics changes observed in the knee model after the ACL structure is removed. The effects of this on the neural response are then summarised towards the end of the section.

5.4.1 Kinematics

As already mentioned, one of the strengths of the computational model over experimental methods are in the ability to measure more aspects of the system. When the ACL is removed from a knee joint, it is known that the stability is reduced and kinematics can change dramatically. The plots in Figure 64 show the changes in kinematics of the knee joint during flexion after the ACL is removed. They show that once the ACL was removed from the feline knee model, the tibia became less stable and moved more medially and anteriorly than it did in the intact knee. Very little change was observed in the vertical displacement of the tibia during flexion. In all of the following kinematic plots, for the three different types of test, a small number of sample points were taken, so some of the curves may appear piece-wise linear at times.

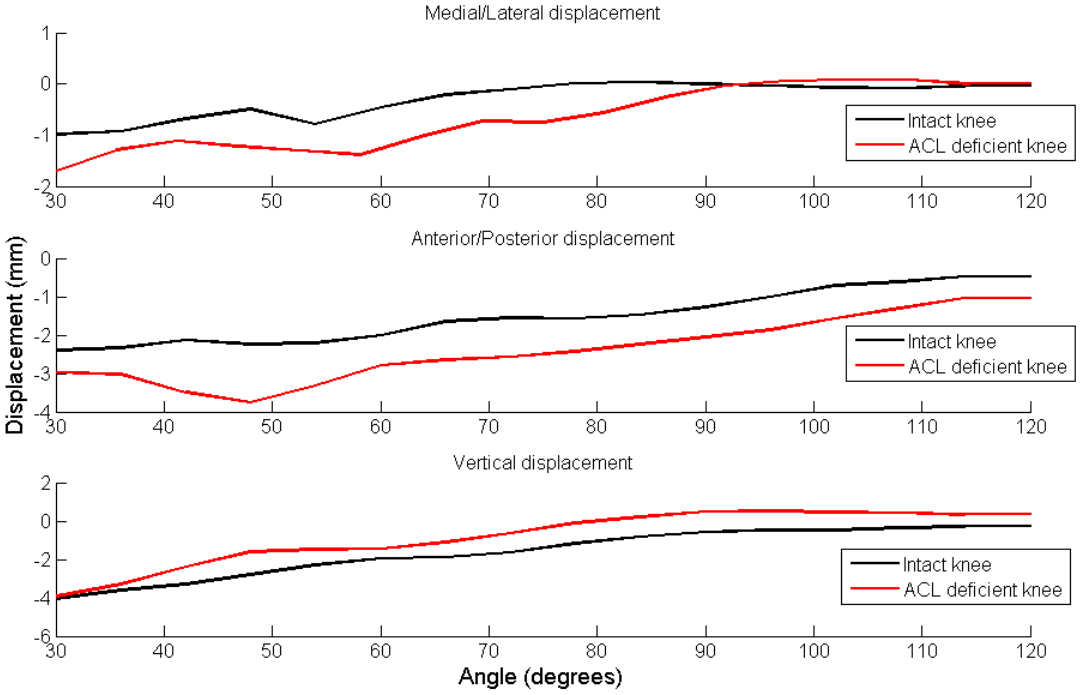

Figure 64: Kinematics of knee joint during flexion from neutral position of 120˚ to 30˚, before and after removing ACL. The top plot shows medial-lateral displacement where negative displacement indicates medial displacement, middle plot shows anterior-posterior displacement where negative displacement indicates anterior displacement, and bottom plot shows vertical displacement.

The anterior tibial drawer test is a common method used for determining whether an ACL is damaged or torn. For this test, a force in the anterior direction is applied to the tibia, and the distance it moves is measured. If there is a damaged or torn ACL, the tibia will move

further than if it is undamaged. Figure 65 shows that after removing the ACL from the feline knee model, the tibia was displaced around 2.5mm further than it did in the intact knee. This not only indicates that the model behaves as would be expected after loss of the ACL, but that this extra displacement could have led to greater deformation of soft tissues, thus resulting in higher neural responses.

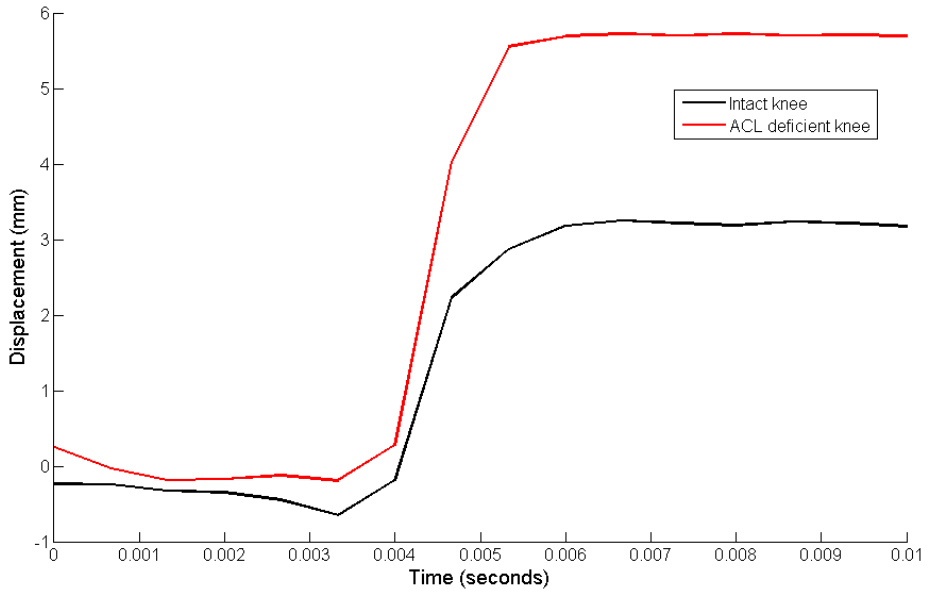

Figure 65: Anterior displacement of the tibia when a load of 30N is applied, before and after removal of the ACL from the FE model of the feline knee joint.

Finally, when loads were applied to the tibia to induce either internal or external rotation, there also could have been a change in the kinematics of the ACL deficient knee. Figure 66 shows the angles that the tibia rotated through after application of the loads, for both internal and external rotation. This suggests that during external rotation, the tibia in the ACL deficient knee rotates slightly further than in the intact knee. Although a different curve is observed between the two knees during internal rotation, the final angle is not different. This could indicate why no significant change in neural response was reported by Gomez-Barrena et al. [16] during this test.

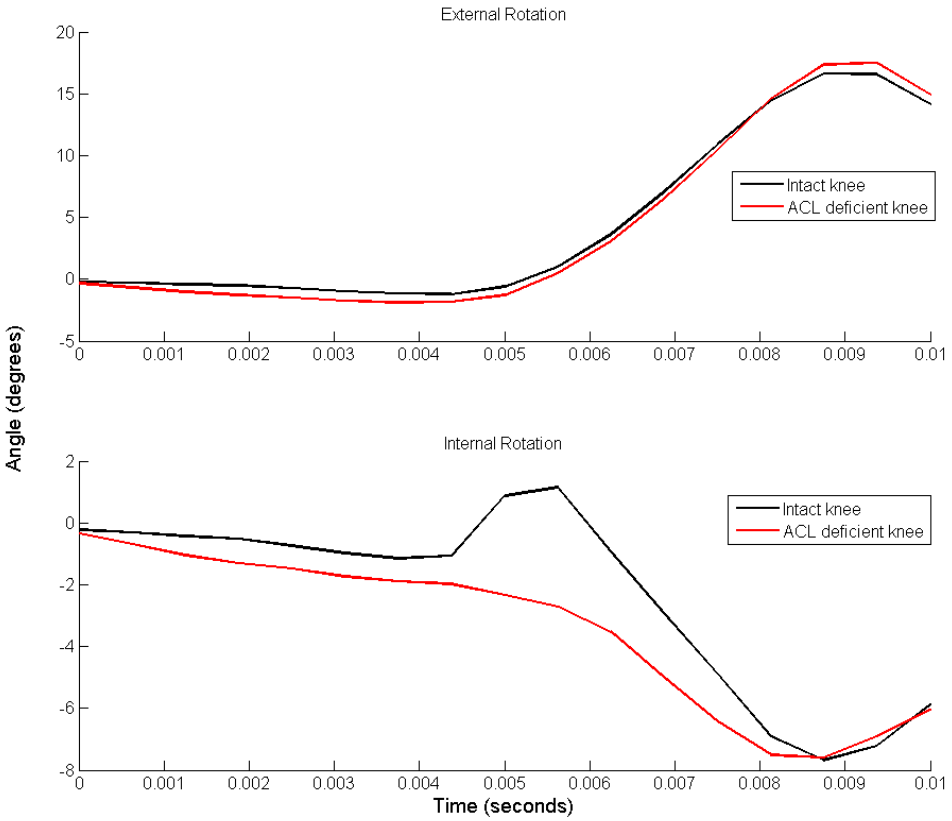

Figure 66: Rotation of tibia during external (top) and internal (bottom) rotation tests, before and after ACL removal. For external rotation, two opposing loads of 30N on neighbouring nodes were applied, and for internal rotation, the loads were 20N.

5.4.2 Neural Responses

This section summarises the changes in neural responses predicted by the model, for each test. Where a significant change is observed, the global signal is broken down to the contributing structures. This helps to indicate why a neural change is observed.

5.4.2.1 Flexion-Extension

In their paper, Gomez-Barrena et al. [16] report that a change in global neural response is observed when the feline knee joint is at 90°, maximum flexion, and maximum extension, after ACL resection. The following plots show the mean global neural responses of both intact knee joint and ACL deficient knee at these three positions. The mean neural responses for these plots were calculated from the ten different element sets that were described in chapter 4.

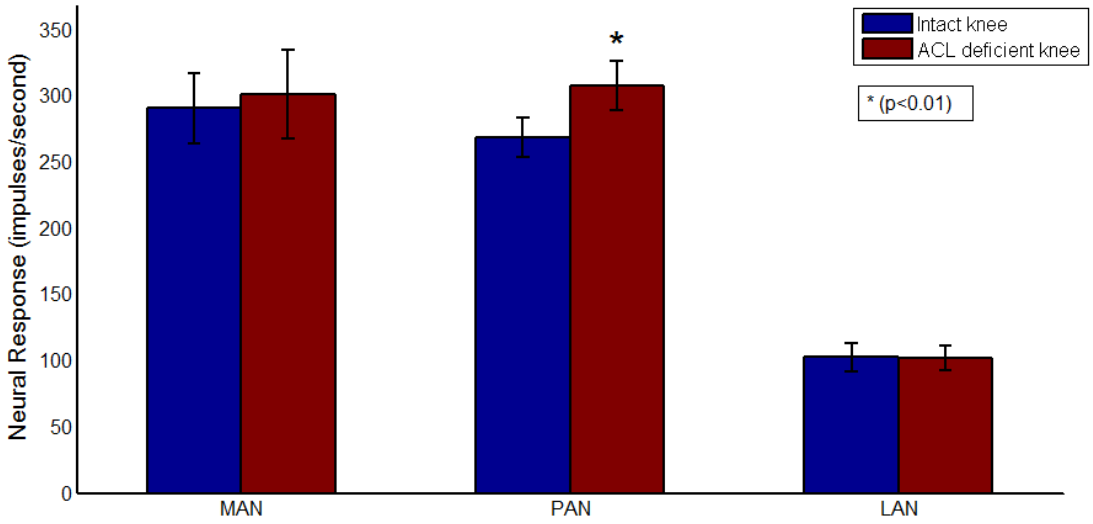

Figure 67: The mean predicted responses at the MAN, PAN, and LAN with knee joint at 90˚, n=10. Blue bars represent the predicted responses from the intact knee, and red bars represent the predicted responses from the ACL deficient knee joint. *(p<0.01).

Figure 68 shows the changes in neural response for the three primary nerves at the maximum flexion angle of 30˚. This indicates that a significant change in neural response is displayed by all three nerves after ACL is removed. Only the neural response of the PAN increases after ACL resection, while the response of the other two nerves decreases.

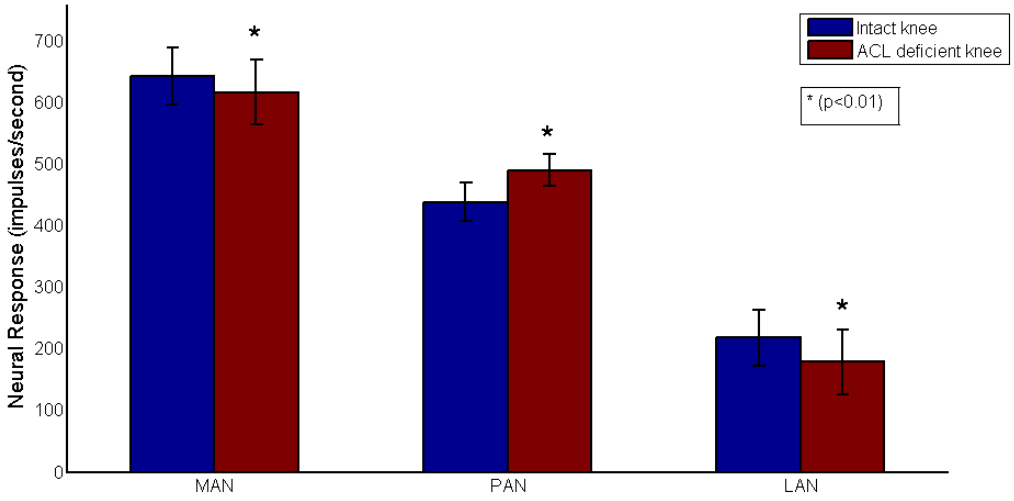

Figure 68: The mean predicted responses at the MAN, PAN, and LAN with knee joint at maximum flexion position of 30˚, n=10. Blue bars represent the predicted responses from the intact knee, and red bars represent the predicted responses from the ACL deficient knee joint. *(p<0.01).

Figure 69 shows that a significant increase in neural response is observed in all primary nerves at the maximum extension angle of 195˚. All plots show that the neural response of LAN is much lower than the responses of PAN and MAN.

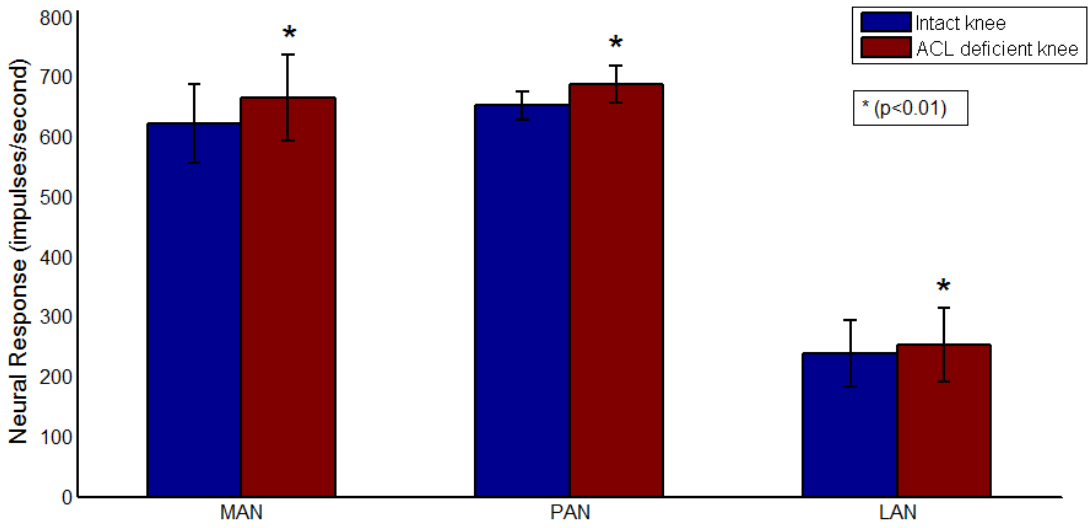

Figure 69: The mean predicted responses at the MAN, PAN, and LAN with knee joint at maximum extension angle of 195˚, n=10. Blue bars represent the predicted responses from the intact knee, and red bars represent the predicted responses from the ACL deficient knee joint. *(p<0.01).

Since significant changes were observed in all three primary nerves, the responses of the dominant structures that contribute to the primary nerves have been broken down to the different types of mechanoreceptor. This helps to understand the causes of any significant changes. The previous chapter highlighted that the dominant structure contributing to the MAN neural response is the MCL, the dominant structures contributing to the PAN were the posterior capsule and PCL, and the dominant structure contributing to the LAN was the LCL. A significant increase in neural response of MAN at joint extension was predicted by the model after ACL removal. The plot in Figure 70 suggests that the MCL contribution to the MAN response is mostly dominated by the Ruffini endings. Increases in response at extension in the ACL deficient knee are displayed. It appears that a step increase in the Ruffini response at about 190˚ in the stable knee appears at 180˚ in the unstable knee. This is also seen, though less prominently, in Golgi and Nociceptor contributions.

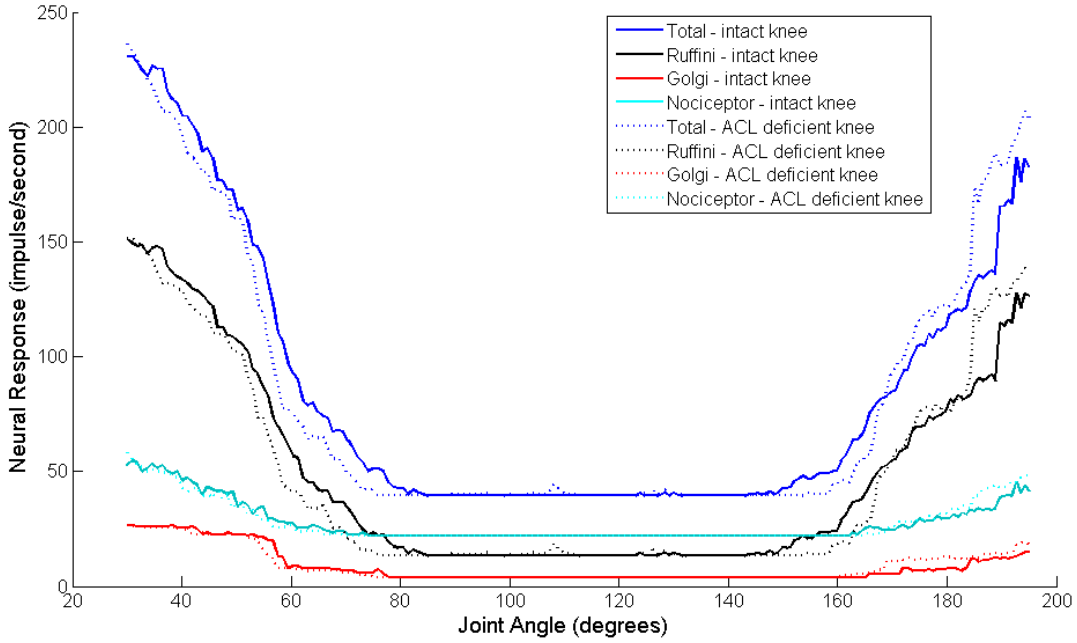

Figure 70: The predicted neural response contribution from the MCL to the global MAN response, broken down to the nerve ending types, during the flexion-extension movement; before and after the ACL is removed from the feline knee joint model. Solid lines represent the neural responses from the intact knee joint, and dotted lines represent the neural responses from the ACL deficient knee joint.

Figure 71 shows the breakdown of mechanoreceptor responses to the PCL contribution to PAN response during flexion and extension. This shows that the Nociceptor is the dominant mechanoreceptor here, with a much stronger response becoming apparent at 50˚ for the unstable knee, even though the initial onset is about 15˚ later than the stable knee. The capsule contribution to the PAN neural response is plotted in Figure 72, and it can be seen that there is not much of a change in its neural repsonse. The percentage increase in neural response is larger from the PCL contribution than the capsule contribution, however the PCL has a lower number of mechanoreceptors, so would have had less of an impact on the global neural response.

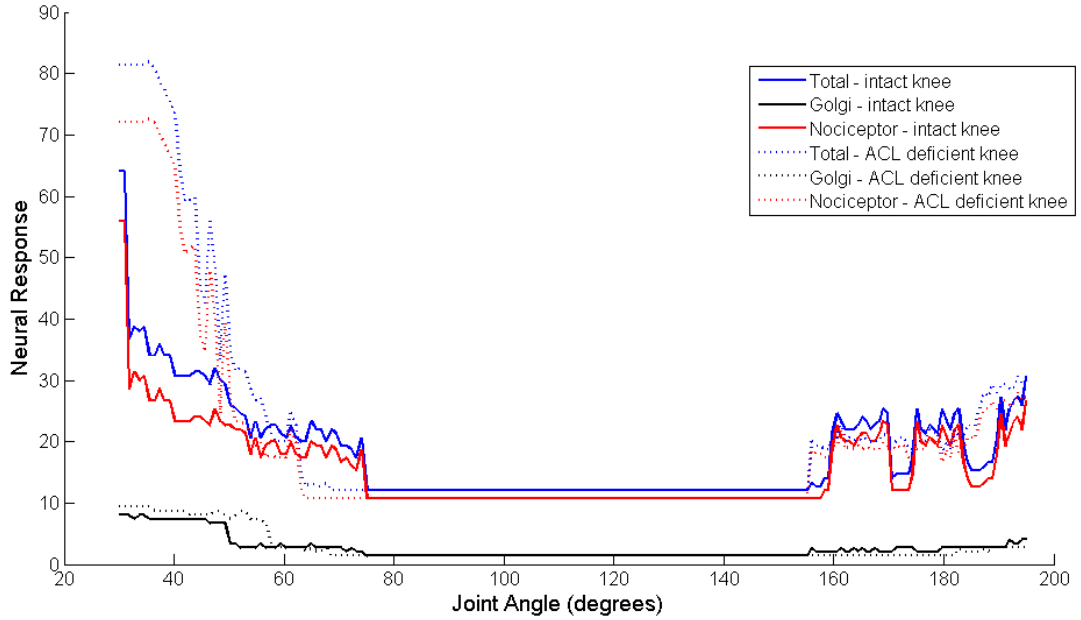

Figure 71: The predicted neural response contribution of the PCL to global PAN response, broken down to the nerve ending types; before and after the ACL was removed from the feline knee joint model. Solid lines represent the neural responses from the intact knee joint, and dotted lines represent the neural responses from the ACL deficient knee joint.

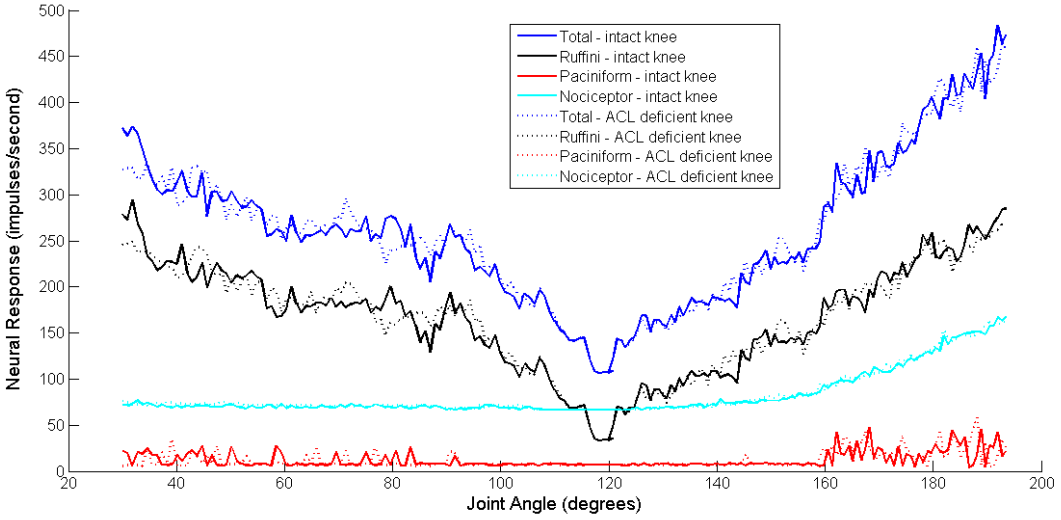

Figure 72: The predicted neural response contribution of the capsule to the global PAN response to flexion and extension, broken down to the nerve ending types; before and after the ACL was removed from the feline knee joint model. Solid lines represent the neural responses from the intact knee joint, and dotted lines represent the neural responses from the ACL deficient knee joint.

On observing the mechanoreceptor contributions to the LCL response in LAN to flexion and extension in Figure 73, it can be seen that the majority of the increase in neural response is due to the Ruffini ending. The Nociceptor response also increases from the base-level response earlier (around 5˚) in the unstable knee than stable knee. No change is seen in the Golgi Tendon Organ. The increases seen in this plot are likely to be the cause of the significant increase at joint flexion of the LAN after ACL removal, as predicted by the model.

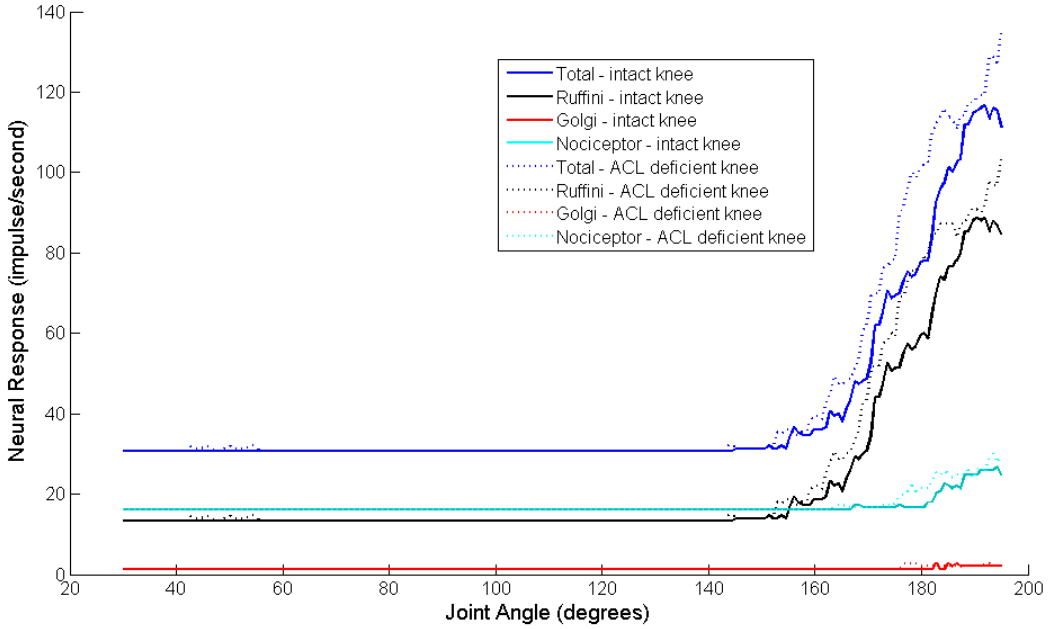

Figure 73: The predicted neural response contribution of the LCL to the global LAN response, broken down to the nerve ending types; before and after the ACL was removed from the feline knee joint model. Solid lines represent the neural responses from the intact knee joint, and dotted lines represent the neural responses from the ACL deficient knee joint.

5.4.2.2 Anterior Tibial Drawer

Since a considerable increase in anterior displacement was observed after the ACL was removed in this test, it was expected that the neural response would reflect this. Figure 74 shows the mean predicted responses of PAN, MAN and LAN to this test, in both intact knee and ACL deficient knee. This shows that the model does indeed predict a significant increase in response for both MAN and PAN after the ACL was removed. The change in LAN response was not significant, though a slight increase was observed.

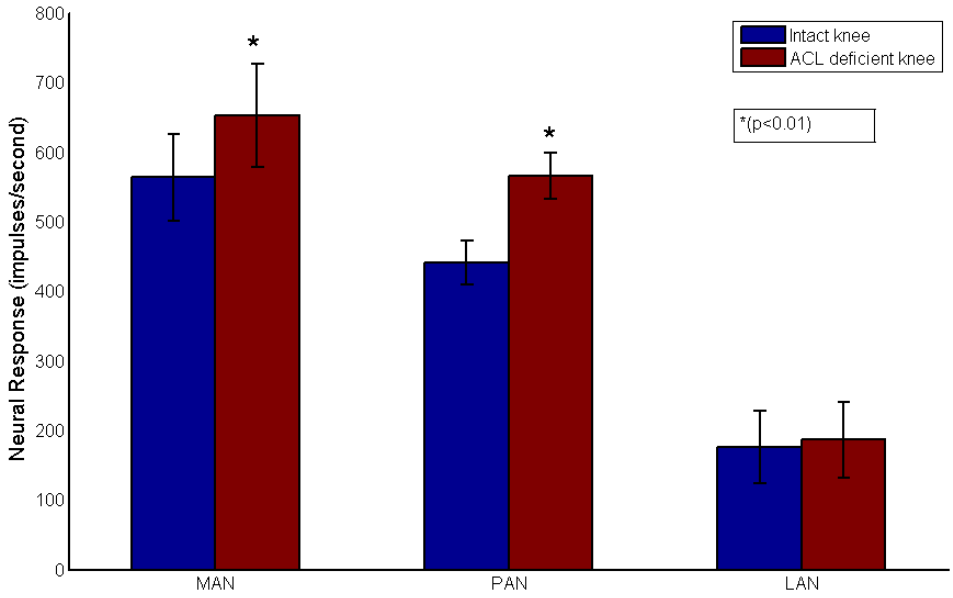

Figure 74: The mean predicted responses at the MAN, PAN, and LAN to anterior tibial drawer with the knee joint at maximum extension angle of 90°, n=10. Blue bars represent the predicted responses from the intact knee, and red bars represent the predicted responses from the ACL deficient knee joint. *(p<0.01).

Both the MAN and PAN responses were predicted to increase significantly after the ACL was removed from the knee joint. The following plots show the neural contributions to the dominant structures for the PAN and MAN. Figure 75 shows all three mechanoreceptor types produce stronger responses in the ACL deficient knee than the intact knee, leading to a significant increase in the total MCL response. A large percentage increase in the neural responses of the PCL and capsule contributions to the PAN is observed, shown in Figure 76 and Figure 77 respectively, suggesting that when the anterior force is applied to the tibia, the remaining structures were stretched more in the ACL deficient knee. This is supported by the higher displacement of the tibia after the ACL was removed (Figure 65, page 125).

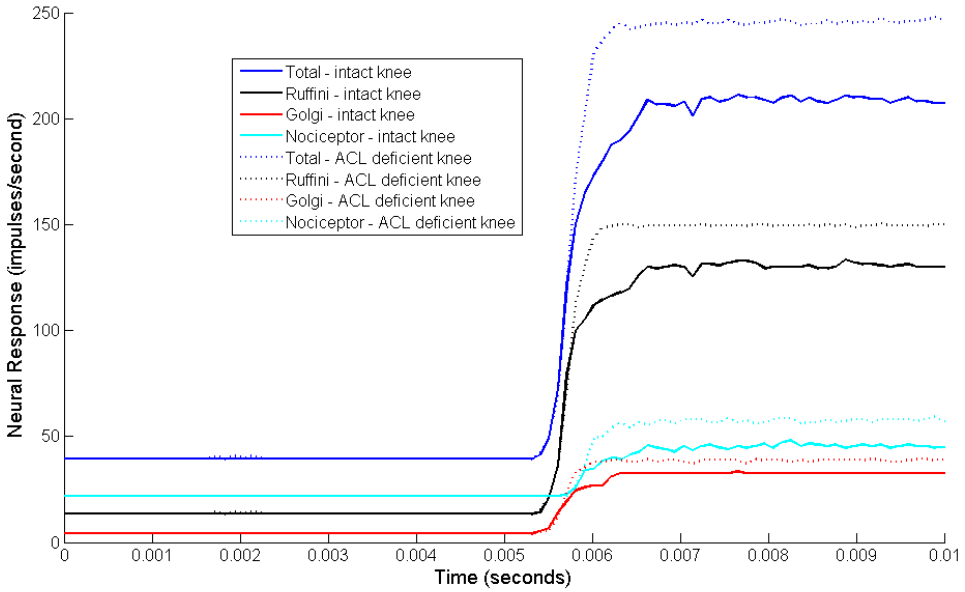

Figure 75: The predicted neural contribution of the MCL to the global MAN response during anterior tibial drawer, broken down to the contributing nerve ending types, before and after the ACL was removed from the feline knee joint. Solid lines represent the neural responses from the intact knee joint, and dotted lines represent the neural responses from the ACL deficient knee joint.

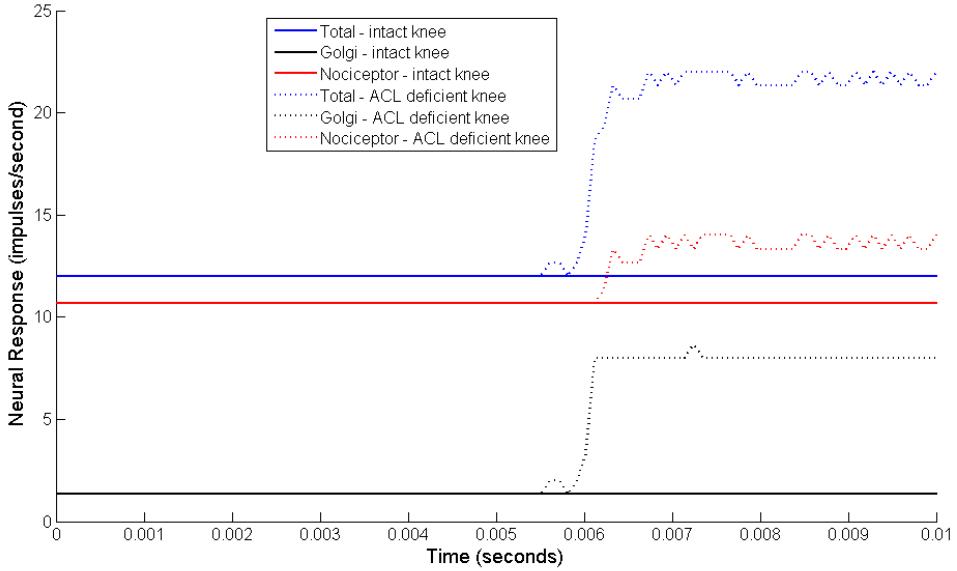

Figure 76: The predicted neural contribution of the PCL to the global PAN response during anterior tibial drawer, broken down to the contributing nerve ending types, before and after the ACL was removed from the feline knee joint. Solid lines represent the neural responses from the intact knee joint, and dotted lines represent the neural responses from the ACL deficient knee joint.

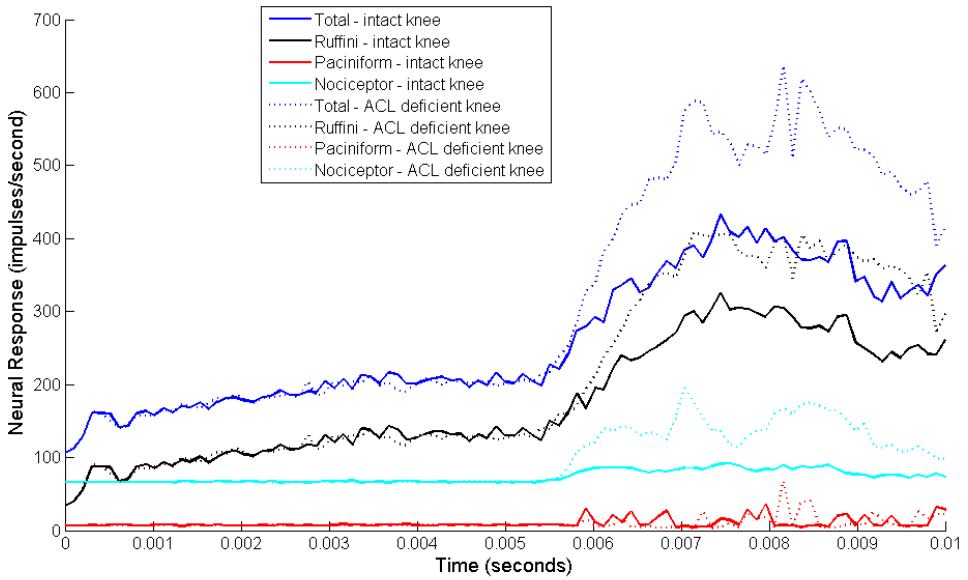

Figure 77: The predicted neural contribution of the capsule to the global PAN response during anterior tibial drawer, broken down to the contributing nerve ending types, before and after ACL was removed from the feline knee joint model. Solid lines represent the neural responses from the intact knee joint, and dotted lines represent the neural responses from the ACL deficient knee joint.

5.2.2 Interior and Exterior Rotation

Finally, the effects of ACL removal on neural response during internal and external rotation of the tibia are shown in the following plots. Figure 78 shows the mean predicted responses of all articular nerves before and after ACL removal for external rotation of the tibia. A significant increase in neural response of the PAN is predicted by the model after removing the ACL. Though slight increases can also be seen in the MAN and LAN responses, they are not significant changes.

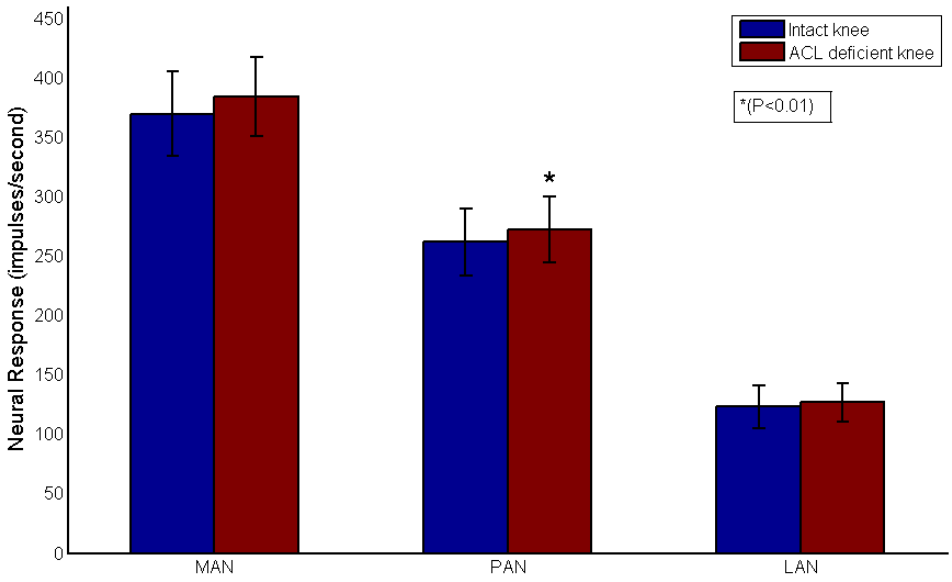

Figure 78: The mean predicted responses at the MAN, PAN, and LAN to external rotation with the knee joint at maximum extension angle of 90˚, n=10. Blue bars represent the predicted responses from the intact knee, and red bars represent the predicted responses from the ACL deficient knee joint. *(p<0.01).

Since a significant increase in the PAN response was predicted, the responses of the dominant structures contributing to this response have been plotted in Figure 79 and Figure 80. Though the neural responses of contributing mechanoreceptors to the PCL response show a decrease after the ACL was removed, the mechanoreceptor responses of the capsule show an increase. Since the frequencies of the capsule responses are far higher than those of the PCL, the overall effect of removing the ACL is likely to be dominated by the capsule response. The PCL contribution to the PAN neural response, in Figure 79, has an unusual shape to the curve. A possible cause for this could be that the knee model was not tested for this type movement, due to a lack of experimental data. This could have resulted in the PCL not being loaded correctly. Also, through observing the behaviour of the neural models in chapter 2, it was seen that they have stepped behaviour to stimulus. Therefore if the structure loading was resulting in fluctuating strains relatively close to the model's threshold, the neural response may suggest more fluctuation than is occurring.

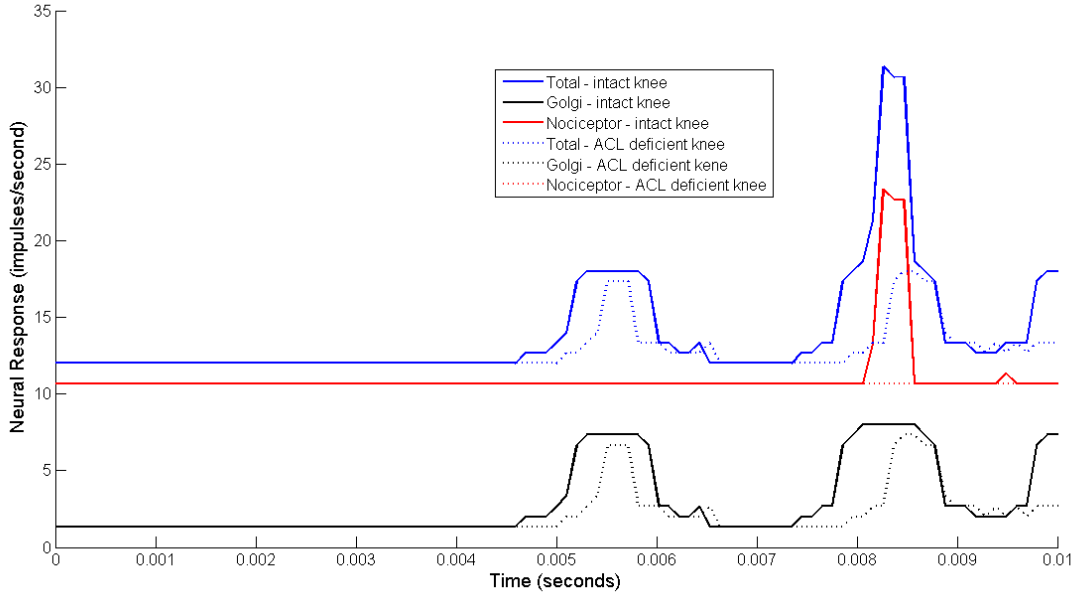

Figure 79: The predicted neural contribution of the PCL to the global PAN response during external rotation, broken down to the contributing nerve ending types, before and after removing the ACL from the feline knee joint model. Solid lines represent the neural responses from the intact knee joint, and dotted lines represent the neural responses from the ACL deficient knee joint.

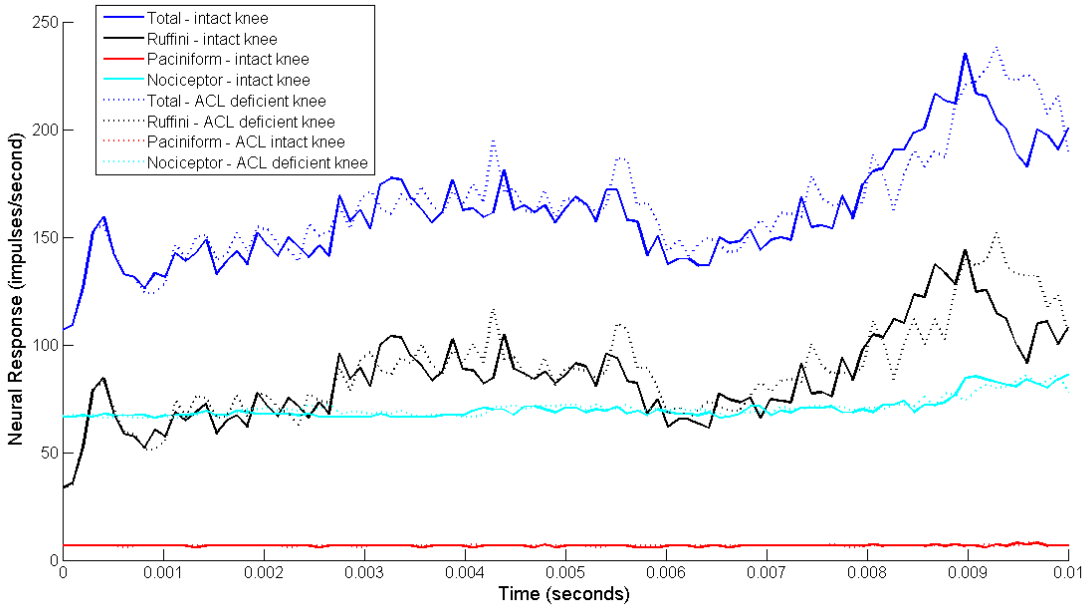

Figure 80: The predicted neural contribution of the capsule to the global PAN response during external rotation, broken down to the contributing nerve ending types, before and after removing the ACL from the feline knee joint model. Solid lines represent the neural responses from the intact knee joint, and dotted lines represent the neural responses from the ACL deficient knee joint.

The mean neural responses of the primary nerves for internal rotation of the tibia are plotted in Figure 81. All three primary nerves show a significant decrease in neural response after the ACL was removed from the model.

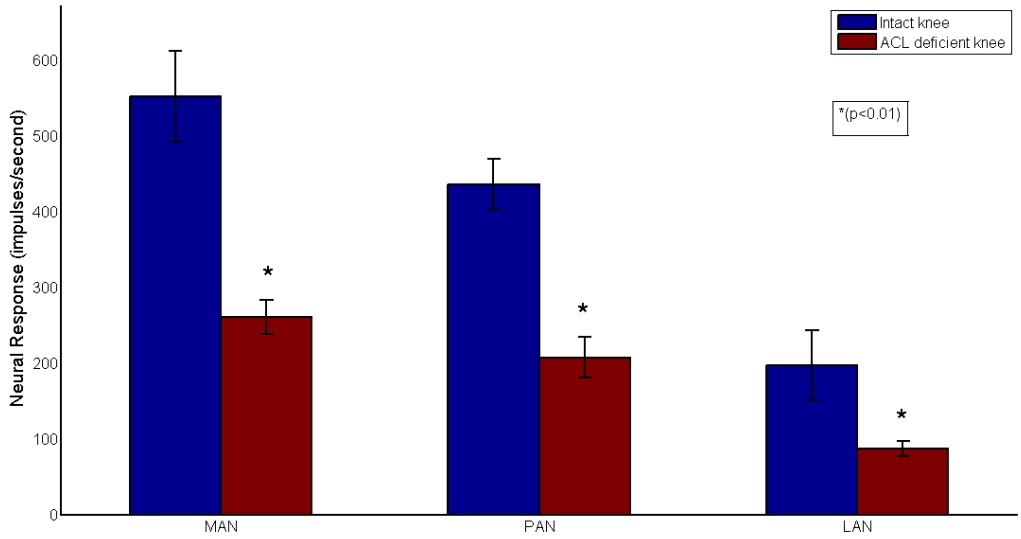

Figure 81 The mean predicted responses at the MAN, PAN, and LAN to internal rotation with the knee joint at maximum extension angle of 90˚, n=10. Blue bars represent the predicted responses from the intact knee, and red bars represent the predicted responses from the ACL deficient knee joint. *(p<0.01).

Since the neural response of the ACL contributes to the LAN responses, it is likely that this is the main cause of the reduced response in this nerve. However, the decreases seen in the other two primary nerves must be due to decreases in the response of remaining structures. Figure 82 shows the response of the MCL, which contributes to the MAN, broken down to the different mechanoreceptor responses. This shows that when the ACL was removed from the model, the response of all mechanoreceptors decreases; this is also seen in the responses of the capsule in Figure 84 (page 139). The PCL response in Figure 83, however, shows an increase during internal rotation of the knee joint in the ACL deficient knee, due to the Golgi tendon organ responses. This could be as a result of the change in kinematics of the knee, shown in Figure 66 (page 126). However, the increased response of the PCL is lost in the global response, due to the high frequencies of the capsule.

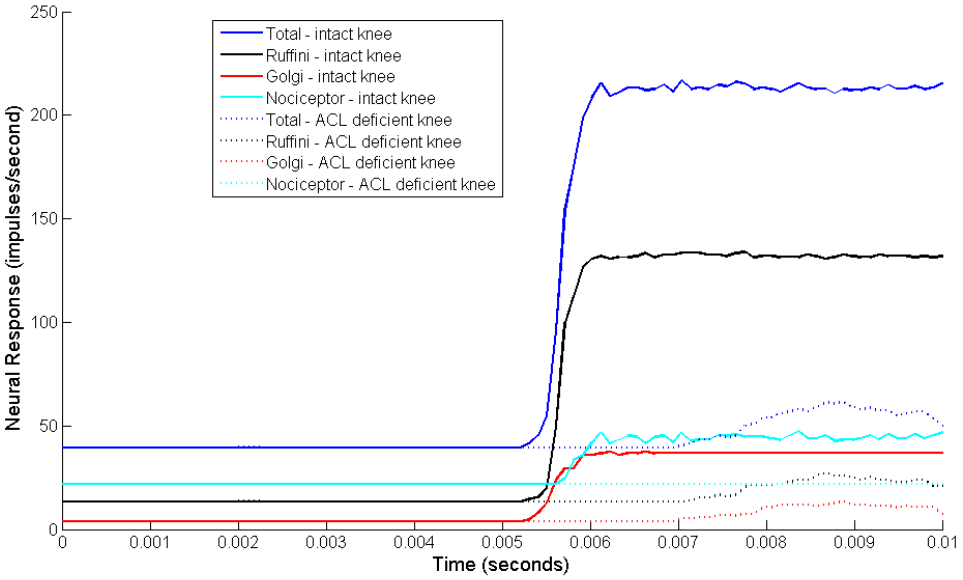

Figure 82: The predicted neural contribution of the MCL to the global MAN response during internal rotation of tibia, broken down to the contributing nerve ending types, before and after the ACL was removed from the feline knee joint model. Solid lines represent the neural responses from the intact knee joint, and dotted lines represent the neural responses from the ACL deficient knee joint.

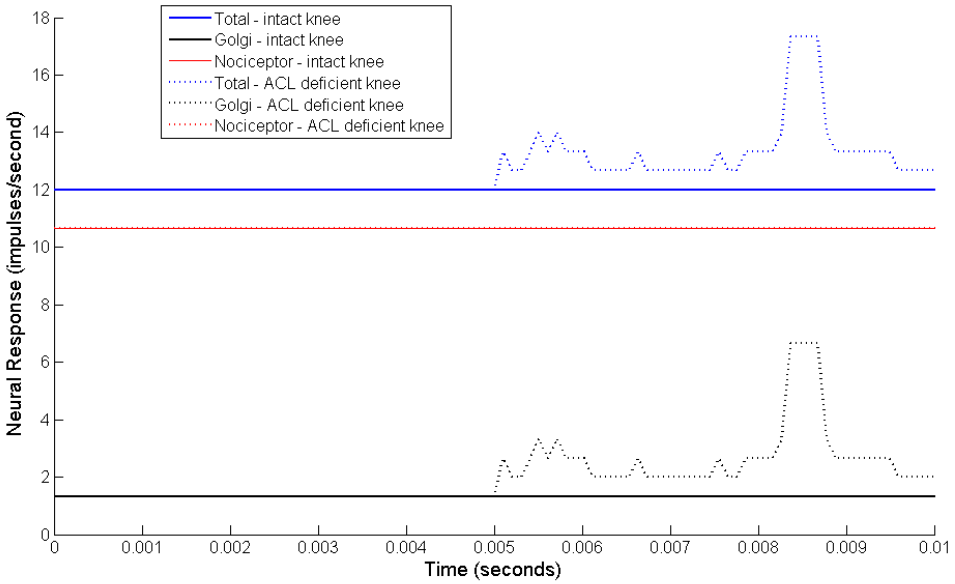

Figure 83: The predicted neural contribution of the PCL to the global PAN response during internal rotation of tibia, broken down to the contributing nerve ending types, before and after the ACL was removed from the feline knee joint model. Solid lines represent the neural responses from the intact knee joint, and dotted lines represent the neural responses from the ACL deficient knee joint.

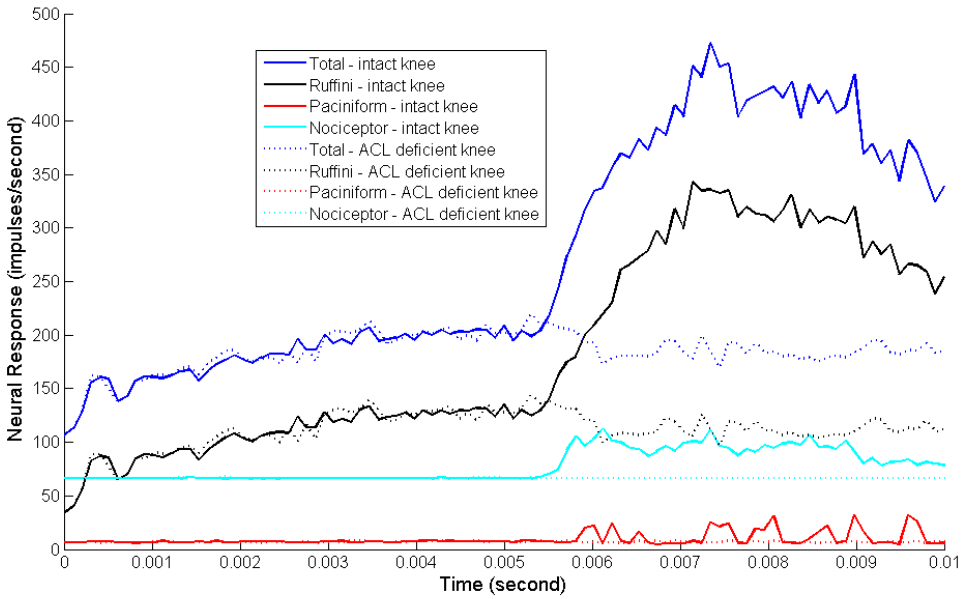

Figure 84: The predicted neural contribution of the capsule to the global PAN response during internal rotation of tibia, broken down to the contributing nerve ending types, before and after the ACL was removed from the feline knee joint model. Solid lines represent the neural responses from the intact knee joint, and dotted lines represent the neural responses from the ACL deficient knee joint.

The curves of the neural response in the ACL deficient knee have a strange shape, as seen in the PCL response during external rotation. This is likely to also be due to the PCL being loaded unusually during the tibia rotation tests. Since the PCL is giving some unusual behaviour, the mean strains that this structure is experiencing during internal and external rotation have been plotted in Figure 85. This shows that from about halfway through the movement, the strains begin oscillating, explaining the shapes of the neural responses in Figure 79 and Figure 83. This behaviour is likely to be due to the model not capturing the internal and external rotation movement well; this is an area where experimental testing of a knee joint could be beneficial in improving the FE knee joint model.

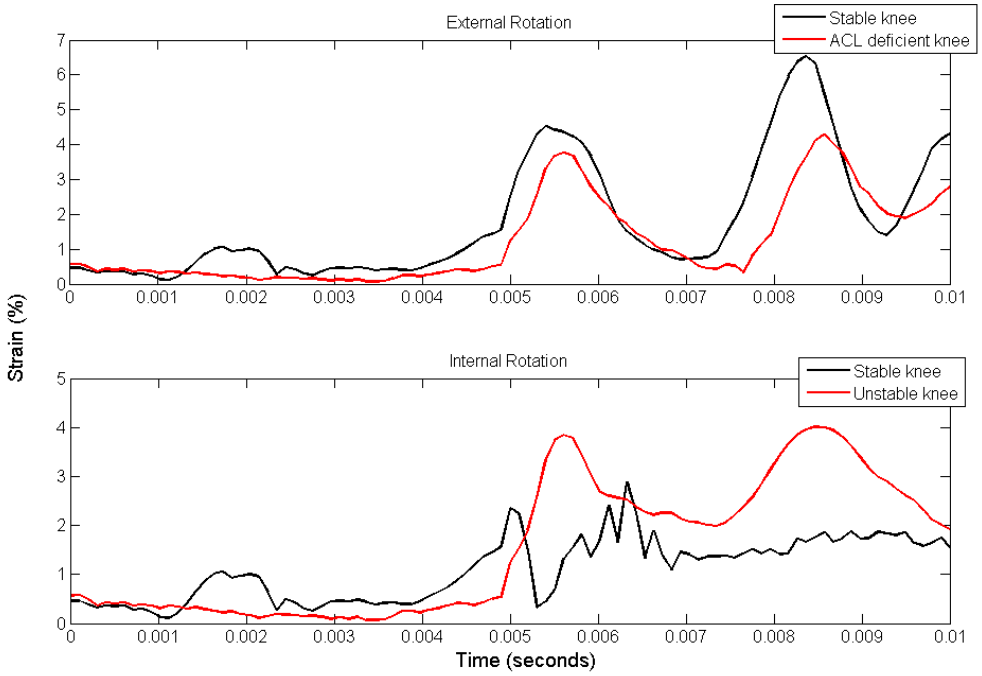

Figure 85: Mean strains experienced by the PCL part of the element set during both external and internal rotation of the tibia.

On observing the PCL behaviour in the model during both the internal and external tibial rotation movements, the structure appears to be experiencing loading and unloading while it is expected that only loading would be experienced. This indicates that either the attachment of the ligament is not strong enough for the loading, or that the tibia has not been constrained enough. This is an area that would have benefited from more detailed validation with experimental data, however as there are no descriptions of the feline knee joint kinematics during internal or external rotation it has not been possible for this study.

5.5 Discussion

This chapter has investigated the effects of loss of the ACL in the knee joint on the neural response, to a range of different movements. A knee that is ACL deficient is less stable than an intact knee, as there is no longer a structure to avoid anterior subluxation of the tibia. Before observing how the neural responses were affected, the kinematics of the intact knee and ACL deficient knee were compared. During flexion, the displacement in both medial and anterior directions was seen to change after the ACL was removed, while vertical displacement remained consistent. The model shows that the tibia moves more in the anterior direction after the ACL was removed than in the intact knee. This is reported to be seen in ACL deficient canine knees [133], suggesting that the model is predicting

realistic changes. The small increase in displacement in the medial direction predicted by the model is also supported by Tashman et al. [133] in the same study.

During the anterior tibial drawer test at 90˚, the model predicted that there was a drastic increase in anterior displacement after the ACL has been removed. Though reports of ACL deficient knees do show an increase in anterior displacement during this test [132], a displacement of 2.5mm is still very high; with the mean increase in displacement in the human knee joint only being 2.1mm [134]. It is known that the medial meniscus plays an important role in preventing the tibia from moving too far anteriorly [135], especially in ACL deficient knees. Since the knee joint model developed in this project does not include the medial meniscus, there may not be enough structures present to prevent excessive anterior tibial displacement, resulting in this high increase. If the medial meniscus were to be included in the model, the results of this test could be improved. Finally, when the tibia was rotated externally, the model predicted that the tibia rotated slightly further in the ACL deficient knee than it did in the intact knee. This has been shown to occur in patients lacking the ACL in a knee [136], supporting the model predictions.

Once it was confirmed that the model was predicting changes in the kinematics of the knee joint after removing the ACL, the neural responses were calculated. Since the knee was clearly less stable without the ACL present, it was expected that the neural response would change. Table 16 below summarises both the changes predicted by the model of the three primary nerves to all five tests, and the changes in neural response of the MAN and PAN reported by Gomez-Barrena et al. [16], for comparison. The predictions of the model match the reports of Gomez-Barrena et al. [16] for the PAN during flexion and external rotation, and for the MAN during extension, tibial drawer and external rotation.

	Gomez-Barrena et al.		Model Predictions		
	MAN	**PAN**	**MAN**	**PAN**	**LAN**
Flexion	↑[b]	↑[a]	↓[b]	↑[b]	↓[b]
Extension	↑[b]	NS	↑[b]	↑[b]	↑[b]
Tibial Drawer	↑[b]	NS	↑[b]	↑[b]	NS
External Rotation	NS	↑[b]	NS	↑[b]	NS
Internal Rotation	NS	NS	↓[b]	↓[b]	↓[b]

Table 16: Changes in neural activity at the articular nerves after ACL removal, as reported by Gomez-Barrena et al. [16], and as predicted by the model. [a]($p<0.05$), [b]($p<0.01$), and NS not significant.

For the neural changes in the PAN for both extension and tibial drawer tests, the model predictions over-estimated the reports from Gomez-Barrena et al. [16]. Though they reported that there was no significant change in the PAN response for these tests, their graphs suggested that there was a slight increase after the ACL was removed; the model predicted a significant increase. Since both of these over-estimations were from the PAN response, perhaps they are due to the Nociceptors having a threshold that is too low, as discussed in the chapter 4. The PAN innervates the posterior capsule with a high population of Nociceptors, if all of these Nociceptors had thresholds that were too low then they could have been be over-sensitive to the changes in kinematics of the joint after the ACL was removed. Another possible cause of these over-estimations could be due to the movement in the anterior-posterior axis. Musculoskeletal structures that have not been included in the model, such as the meniscus and popliteus tendon, could provide more stability to the knee, resulting in less of an increase in the neural response.

In the case of patients that have experienced ACL rupture, often specialised training is offered to try and develop the muscles around the knee joint so that they can take on the role of the ACL in its absence. This is, however, a lengthy process with reports that a 4-week program of rehabilitation is not enough to observe any improvements in proprioception around the knee joint [131]. However in the long term, the muscles around the knee joint, such as quadriceps and hamstring, appear to be recruited in different orders or for different periods, to allow for improved proprioception [131]. Since the

purpose of this study has been to focus on the proprioceptive nature of the soft tissues within the knee joint, this adaptive nature of improving proprioception has not been considered further. Through including the muscle structures and muscle spindles in the model, it may be possible to test what muscular activity may be required to return the joint neural activity to a similar level as seen in the stable knee joint.

The model predictions do not match the reports from Gomez-Barrena et al. [16] for the MAN response to flexion and internal rotation, and for the PAN response to internal rotation. As already mentioned, the lack of medial meniscus could have resulted in changes in the kinematics of the knee. However, it could also contribute to the neural response of the MAN, with reports of it being innervated [137] and suggestions that it is this structure that results in increased responses from the MAN [16]. For the internal rotation test, it was not possible to apply a torque to the model of a similar magnitude to that described by Khalsa and Grigg [129] in their experiments, due to excess deformation of the joint capsule. This meant that the full movement that was performed by Gomez-Barrena et al. [16] may not have been reached by the model, and could be the reason that the model predicted lower neural responses in the ACL deficient knee.

It has not been possible to verify the predictions of the LAN response, since Gomez-Barrena et al. [16] did not measure the nerve's response during any of these tests. In most of the tests, the LAN response decreased after the ACL was removed from the knee. This is sensible, since the LAN innervates the ACL, so there would be fewer mechanoreceptors contributing to this global response. In extension, however, the model predicted an increase in the LAN. This could have been due to the LCL becoming more involved in the movement, and its neural contributions increasing more than the initial decrease due to the lack of ACL contributions.

The changes in neural response described so far could indicate a change in proprioception around the knee joint after removal of the ACL. Literature suggests that ACL deficiency leads to a decrease in proprioception [131]. However, in their paper, Gomez-Barrena et al. [16] highlight that their definition of proprioception is "the transmission of mechanically-evoked electrical nerve signals triggering muscular response", and not the conscious perception of joint positions. The studies suggesting increased proprioception [131] are likely to be reporting the conscious proprioception, so are not comparable with the results of this study. If we use the definition of proprioception from Gomez-Barrena et al. [16], the

predictions from the model suggest that proprioception has been altered as a result of removing the ACL.

Although the level of proprioception that the model was able to predict was in the neural behaviour before any higher level processing, perhaps the neural behaviour from each structure could help to indicate the cause of a decrease in conscious proprioception that is observed in patients that have ruptured the ACL. When the ACL neural contribution to the global LCL response was observed in chapter 4 (Figure 73, page131), it could be seen that its frequency increased during knee flexion, from around 60˚. After the ACL was removed from the knee joint model, the structures that displayed different neural response during the flexion movements were mainly the MCL and PCL. The neural responses of these structures in the flexion movement up to 60˚ were lower in the ACL deficient knee than the intact knee (Figure 82, page 138 and Figure 83, page 138). It is not until the knee reaches flexion angles of around 40˚ that the neural responses become higher in the ACL deficient knee. This perhaps suggests a delay in the remaining structures that are taking the load left by the ACL. This delayed response from the remaining structures may not provide the required information for position control in the ACL deficient knee joint, thus explain the reduced proprioception reported in patients with a damaged ACL.

Even though conscious proprioception has not been predicted by the model in this thesis, it may be possible to make connections between the neural responses and either proprioception or nociception. For example, since Nociceptors sense harmful and painful stimuli, an increase in their response such as those predicted during anterior tibial drawer, could be assumed to represent an increase in the pain experienced at the knee joint. Similarly, the increases observed in responses of Ruffini endings, such as those predicted during flexion and extension, could suggest more of a change in proprioception. These are only suggestions, however, since we do not know the processes that occur in the spinal cord and brain to result in either nociceptive or proprioceptive sensations.

This chapter has described the effects of removing the ACL from the knee joint on the predicted neural responses during a range of movements. In general the model predicted an increased neural response in the MAN and PAN after the ACL was removed, and a decrease in response in the LAN. When compared with the experimental data of Gomez-Barrena et al. [16], the predictions from the model for the MAN and PAN mostly matched. In the cases that the predictions did not match, the model had been over-sensitive to the changes experienced by the ACL deficient knee joint, which could have been due to

excessive movement of the tibia or Nociceptors with low thresholds. The relationship between neural responses measured from the primary nerves and conscious proprioception have also been discussed in this chapter. It has been highlighted that although the model is unable to directly predict changes in the perceived proprioception, it helps us determine that it is likely that the knee joint mechanoreceptors are involved in proprioception. Potential future uses for a model of this type include the testing of rehabilitation methods for patients with poor proprioception, and even in development of robotics; these are discussed in more detail in the following chapter.

Chapter 6

Conclusions and Future Work

Knee pain is a major problem, as the knee is a joint that is susceptible to injuries, such as tearing of ligament structures. Though it is often possible to repair the damaged joint, it is more difficult to ensure the patient will no longer experience pain, as pain is highly subjective and its causes are not always completely understood. It is known, however, that in order to feel pain, sensory nerve endings must be present in the relevant body part. Some sensory endings are involved in proprioception, a conscious sensation that is also shown to be affected by injuries. While mechanical sensing endings are present in the soft tissues around the knee joint, such as ligaments, the literature is inconsistent with indicating whether they are involved in proprioception. Determining whether the deeper soft tissues in the joint are involved in this sensation was the motivation behind this thesis, and through the use of computational methods it has been possible to expand our understanding of neural activity around the knee joint. A computational model has been developed that is able to simulate the neural activity at the feline knee joint, which has involved building models of both the mechanical sensing nerve endings and of a feline knee joint.

The sensory nerve ending models that were developed in this thesis have been based on the popular Hodgkin-Huxley model, and the general model was verified using recordings from the Viscerofugal nerve endings found in gut tissue; this was described in chapter 2. Though we were able to both calibrate and verify the model's predictions for this type of mechanoreceptor, there are very few detailed reports of recordings of nerve endings that are specific to the knee joint. For this reason, it was not possible to test the behaviour of all of the sensory ending models, although the sensitivity of the general model was tested for

different types of input strains, indicating that it was able to predict satisfactory results with both hydrostatic and *y* only strains. The second stage of the model development process involved building a computational model that represents a feline knee joint; described in chapter 3. For this, x-ray CT scans were used to build a finite element model that included all of the four main ligaments, patellar tendon, joint capsule and fat pad; structures that had not been included in a single model together until now. This resulted in a complex model that was able to predict the relationship between torque and joint angle that is displayed by the feline knee joint.

Chapter 4 describes the method that was used to combine the two types of model, resulting in a computational model that could predict the neural response to changes in knee position. The sensitivity of the model to nerve ending locations, which were assumed to be random, was tested through creating ten models, each with different locations of endings. It was determined that the nerve location did not affect the global neural response considerably, so the assumption of randomly located nerve endings was acceptable. When all of the predicted frequencies were summed, it was shown that the ending locations did not affect the global neural response during flexion and extension of the knee joint. The final version of the model was also shown to be able to predict a similar relationship between the neural response and the flexion-extension movement to that seen in the literature.

Once it was accepted that the model was predicting realistic neural responses to changes in knee joint position, it was used to predict the effect of losing the anterior cruciate ligament (ACL) on neural response. As already described damage of a soft tissue structure, such as the ACL, can not only prove painful but can also drastically change the joint's stability and proprioception. It was predicted that the neural response of the ACL deficient knees would be significantly different to the response of intact knees when the joints were moved through a range of positions; flexion-extension, anterior tibial drawer and internal-external rotation. When compared with reports from the literature, most of the predictions from the model were similar, although in some cases it was over-sensitive to the removal of the ACL. These differences were likely to have been due to the lack of certain structures in the knee joint model, such as medial meniscus and popliteus tendon, which could have resulted in the kinematics of the knee joint changing more dramatically than may be seen in reality.

Since the initial motivation of this thesis was the high occurrence of knee pain, and whether joint receptors were involved in proprioception, a question that must be answered is whether the model developed through this thesis can be used to further our understanding in this area. First, we must answer the question of whether an increase in neural response is equivalent to an increase in pain and proprioception. Ultimately, the processing of neural response into a conscious sense is carried out later in the neural system, so it is unlikely that a simple increase in neural response can be equal to a direct increase in pain. However, a significant change in the neural response is likely to be relatable to changes in proprioception, since it indicates a change in the information that the brain is receiving. Understanding signal processing that is likely to occur later in the neural system is outside of the scope of this thesis, so we can only suggest what the changes in neural response may represent. One area that could be utilised in understanding whether there is pain at the knee joint is in the type of mechanoreceptor that is firing. It is known that Nociceptors have a higher threshold than the other mechanoreceptors at the knee joint, so will only respond to noxious stimuli. In some cases, the model predicts higher neural response to be produced by the Nociceptors in the ACL deficient knee; this could be directly related to an increase in the pain at the knee joint.

The results of this thesis have led us to ask more questions on the understanding of neural responses at the knee joint. Though improvements on the model could lead to higher accuracy in the results I believe that before any additions to the model itself are made, more validation and experimental data is required regarding the innervation of the knee joint. This is probably the area of this project that is most lacking. A study that involves detailed descriptions of the innervation of the knee joint would be essential to any further progress in this field. The study would need to report the number of nerve endings that are present in each structure of the joint, and ideally the locations of the nerve endings would also be described. The variation of these both within and between species would also be useful.

A second study that I would suggest performing before any additions to the model are made involves recording the behaviour of each of the four mechanoreceptor types to a range of loading conditions would be required. These experiments would be similar to those performed for the recordings of Viscerofugal neurons, as described in chapter 2, although the samples would be from a range of soft tissues from the knee joint. Also, global

recordings of entire ligaments, and eventually the knee, would be invaluable to understanding neural behaviour at this joint.

Only after these suggested experiments have been completed would it be worth developing a more detailed version of the model in this thesis. After the new information acquired from these experiments have been applied to the model it would be possible to begin to include more complexity, with the knowledge that we would be able to verify its predictions. Major changes to the model include the addition of extra structures in the knee, that were originally missed out; this would be possible with more detailed MRI scans, so the structures could be identified and accurate geometries built. Also, the effects of the synovial fluid could be included, through use of a multi-physics software such as Comsol. This would mean the pressure changes experienced by the capsule that occur during joint movement could be captured, and any neural responses predicted.

Ideally, it would be possible to apply the knowledge developed through these improvements to a neural model of the human knee joint. Since it is pain of the human knee that is of interest to us, this is the only way to get meaningful results that could help in the recovery process of patients experiencing knee pain. Unfortunately, it would be very difficult to validate a model of this type, since all experiments involved in the neural response of the knee joint are highly invasive and unlikely to meet ethical regulations for application to the human knee. It is very important, therefore, that the feline knee joint model is producing accurate neural predictions before the human knee joint is considered. Also, before direct application to the human knee joint is possible, the differences between these new joints must be fully understood. While there are areas that are known to be relatively similar such as the anatomy, as discussed in chapter 3, there are others that are less well known. For example, the nerve ending density is likely to be different, and it is not known whether the same nerve endings found in the feline knee are present in the human knee joint, with the same thresholds. Other areas of differences are in the loading and uses of the joint, with the cat being a four legged mammal the ways in which the knee is used would differ from the knee of a human. Finally, based on the different loading conditions, the tissue properties would also be different, although this information is better recorded for the tissues of the human than cat.

With a model that is capable of predicting the neural response around a human knee joint the possible uses are exciting, from testing of rehabilitation techniques to development of robotics. If the model could be incorporated with more of the musculoskeletal system, the

effects of certain rehabilitation techniques for patients with damaged ACL, or other stability reducing trauma, could be compared with surgery or other options the patient may have. It could also be used to identify which muscles specifically are likely to require strengthening to reduce the neural response around the knee joint. With the pain aspect of the model, early design prosthetic joints could be tested to determine whether they would increase the patient's pain in the process of improving function. Finally, since the neural system is a feedback loop, this model could help with the design of robotic limbs, where a constant feedback from sensory stimuli is required to ensure stability and functionality.

This thesis describes the development of a model that can simulate the neural response at a feline knee joint. It is the first computational model that can simulate the neural activity at a global level, since previous neural models only consider the response to local changes in soft tissue. It is also the first finite element model of a knee joint to include the fat pad or complete joint capsule. Even with the lack of experimental data for validation of the model through the different stages, the results from the completed model were comparable with experimental data, both in the healthy and ACL deficient feline knee joint. The fact that the knee model was able to predict significant changes in neural response after the ACL was removed allows us to suggest that the joint receptors are involved in proprioception, therefore achieving the main objective of this project. Although it has not been possible to directly connect the neural response with conscious proprioception, I have also been able to use the model to suggest reasons for the lowered proprioception experienced by patients with a damaged ACL.

Bibliography

1. KNEEguru. *The capsule of the knee joint*. 2008 [cited 2010 13/07/10]; Available from: http://kneeguru.co.uk/KNEEnotes/node/827.

2. Registry, N.J., *10th Annual Report 2013, National Joint Registry for England, Wales and Northern Ireland*, 2013.

3. English, S. and D. Perret, *Posterior knee pain.* Current Reviews in Musculoskeletal Medicine, 2010. **3**: p. 3-10.

4. Dennis, D.A., *Evaluation of painful total knee arthroplasty.* Journal of Arthroplasty, 2004. **19**(4 Suppl 1): p. 35-40.

5. Wylde, V., et al., *Persistent pain after joint replacement: Prevalence, sensory qualities, and postoperative determinants.* Pain, 2011. **152**(3): p. 566-572.

6. Baker, P.N., et al., *The role of pain and function in determining patient satisfaction after total knee replacement - Data from the National Joint Registry for England and Wales.* Journal of Bone and Joint Surgery-British Volume, 2007. **89B**(7): p. 893-900.

7. Brazier, M., *A history of neurophysiology in the 19th century*. 1988: Raven Press.

8. Guyton, A.C. and J.E. Hall, *Textbook of Medical Physiology*. 11th ed. 1956, Phyladelphia: Elsevier Inc.

9. Simmons, S., et al., *Proprioception After Unicondylar Knee Arthoplasty Versus Total Knee Arthroplasty.* Clinical Orthopaedics and Related Research, 1996. **311**: p. 179-184.

10. Isaac, S.M., et al., *Does arthroplasty type influence knee joint proprioception? A longitudinal prospective study comparing total and unicompartmental arthoplasty.* The Knee, 2007. **14**: p. 212-217.

11. Swanik, C.B., S.M. Lephart, and H.E. Rubash, *Proprioception, Kinesthesia, and Balance After Total Knee Arthroplasty with Cruciate-Retaining and Posterior Stabilized Prostheses.* Journal of Bone and Joint Surgery [Am], 2004. **86**: p. 328-334.

12. Wada, M., et al., *Joint Poprioception Before and After Total Knee Arthroplasty.* Clinical Orthopaedics and Related Research, 2002. **403**: p. 161-167.

13. Ralphs, J.R. and M. Benjamin, *The joint capsule: structure, composition, ageing and disease.* Journal of Anatomy, 1994. **184**: p. 7.

14. Katonis, P., et al., *Mechanoreceptors of the Posterior Cruciate Ligament.* The Journal of International Medical Research, 2008. **36**: p. 387-393.

15. Hodgkin, A.L. and A.F. Huxley, *A quantitative description of membrane current and its application to conduction and excitation in nerve.* Journal of Physiology, 1952. **117**: p. 500-544.

16. Gomez-Barrena, E., et al., *Neural and muscular electric activity in the cat's knee: Changes when the anterior cruciate ligament is transected.* Acta Orthopaedica Scandinavica, 1997. **68**(2): p. 149 - 155.

17. Freeman, M.A. and B. Wyke, *The innervation of the knee joint. An anatomical and histological study in the cat.* Journal of Anatomy, 1967. **101**(3): p. 505-532.

18. Shepherd, G.M., *Neurobiology*. 3rd ed. 1994, New York: Oxford University Press, Inc.

19. Morris, C.E., *Mechanosensitive Ion Channels.* Journal of Membrane Biology, 1990. **113**: p. 93-107.

20. Hogervorst, T. and R.A. Brand, *Current Concepts Review - Mechanoreceptors in Joint Function.* The Journal of Bone & Joint Surgery, 1998. **80**: p. 1365-1378.

21. Khalsa, P.S., A.H. Hoffman, and P. Grigg, *Mechanical States Encoded by Stretch-Sensitive Neurons in Feline Joint Capsule.* Journal of Neurophysiology, 1996. **76**(1): p. 175-187.

22. Grigg, P. and A.H. Hoffman, *Properties of Ruffini afferents revealed by stress analysis of isolated sections of cat knee capsule.* Journal of Neurophysiology, 1982. **47**(1): p. 41-54.

23. Skoglund, S., *Anatomical and physiological studies of knee joint innervation in the cat.* Acta Physiologica Scandinavica, 1956. **36**(Suppl 124).

24. Hromada, J. and P. Polacek, *A contribution to the morphology of encapsulated nerve endings in the joint capsule and in the preiarticular tissue.* Acta Anatomica, 1958. **33**: p. 187-202.

25. Boyd, I.A., *The histological structure of the receptors in the knee-joint of the cat correlated with their physiological response.* Journal of Physiology-London, 1954. **124**(3): p. 476-&.

26. Heppelmann, B., et al., *Ultrastructural Three-Dimensional Reconstruction of Group III and Group IV Sensory Nerve Endings ("Free Nerve Endings" in the Knee Joint Capsule of the Cat: Evidence for Multiple Receptive Sites.* The Journal of Comparative Neurology, 1990. **292**: p. 103-116.

27. Loewenstein, W.R., *On the 'specificity' of a sensory receptor.* Journal of Neurophysiology, 1961. **24**: p. 150-158.

28. Ekholm, J., G. Eklund, and S. Skoglund, *On the Reflex Effects from the Knee Joint of the Cat.* Acta Physiologica Scandinavica, 1960. **50**: p. 167-174.

29. Johansson, H., et al., *Peripheral Afferents of the Knee: their effects on central mechanisms regulating muscle stiffness, joint stability, and proprioception and coordination*, in *Proprioception and Neuromuscular Control in Joint Stability*, S.M. Lephart and F.H. Fu, Editors. 2000, Human Kinetics. p. 5-22.

30. Eklund, G. and S. Skoglund, *On the specificity of the Ruffini like joint receptors.* Acta Physiologica Scandinavica, 1960. **49**: p. 184-191.

31. Boyd, I.A. and T.D.M. Roberts, *Proprioceptive discharges from stretch-receptors in the knee-joint of the cat.* Journal of Physiology-London, 1953. **122**(1): p. 38-59.

32. Iggo, A. and K.H. Andres, *Morphology of Cutaneous Receptors.* Annual Review of Neuroscience, 1982. **5**: p. 1-31.

33. Loewenstein, W.R., *Excitation and inactivation in a receptor membrane.* Annals of the New York Acadamy of Sciences, 1961. **94**((2)): p. 510-534.

34. Bell, J., S.J. Bolanowski, and M. Holmes, *The structure and function of Pacinian Corpuscles: a review.* Progress in Neurobiology, 1994. **42**: p. 79-128.

35. Kandel, E.R., J.H. Schwartz, and T.M. Jessell, *Principles of neural science*. 4th ed. 2000, United States of America: McGraw-Hill Companies. 1414.

36. Macefield, V.G., *Physiological characteristics of low-threshold mechanoreceptors in joints, muscle and skin in human subjects.* Clinical and Experimental Pharmacology and Physiology, 2005. **32**: p. 135-144.

37. Taylor, D.C.M. and F.K. Pierau, *Nociceptive Afferent Neurons*. Studies in Neuroscience, ed. W. Winlow. 1991, Manchester: Manchester University Press. 155.

38. Pare, M., C. Behets, and O. Cornu, *Paucity of presumptive Ruffini corpuscles in the index finger pad of humans.* Journal of Comparative Neurology, 2003. **456**(3): p. 260-266.

39. Grigg, P., *Mechanical factors influencing response of joint afferent neurons from cat knee.* Journal of Neurophysiology, 1975. **38**(6): p. 1473-1484.

40. Hibberd, T.J., N.J. Spencer, and S.J. Brookes, *Extracellular Recordings of Identified Vescerofugal Neurons in Guinea Pic Colon.* Gastroenterology, 2011. **140**(5).

41. Hibberd, T.J., et al., *Identification and mechanosensitivity of viscerofugal neurons.* Neuroscience, 2012. **225**: p. 118-129.

42. Hoffman, A.H., P. Grigg, and D.M. Flynn, *A Biomechanical Model of the Posterior Knee Capsule of the Cat.* Journal of Biomechanical Engineering, 1985. **107**: p. 140-146.

43. Grigg, P., *Stretch Sensitivity of Mechanoreceptor Neurons in Rat Hairy Skin.* Journal of Neurophysiology, 1996. **76**(5): p. 2886-2895.

44. Schäfer, S.S., B. Berkelmann, and K. Schuppan, *Two groups of Golgi tendon organs in cat tibial anterior muscle identified from the discharge frequency recorded under a ramp-and-hold stretch.* Brain Research, 1999. **846**: p. 210-218.

45. Gregory, J.E. and U. Proske, *The responses of Golgi tendon organs to stimulation of different combinations of motor units.* Journal of Physiology, 1979. **295**: p. 251-262.

46. Mileusnic, M.P. and G.E. Loeb, *Mathematical Models of Proprioceptors. II. Structure and Function of the Golgi Tendon Organ.* Journal of Neurophysiology, 2006. **96**: p. 1789-1802.

47. Fukami, Y. and R.S. Wilkinson, *Responses of isolated Golgi tendon organs of the cat.* Journal of Physiology, 1977. **265**(3): p. 673-689.

48. Crago, P., J.C. Houk, and W.Z. Rymer, *Sampling of Total Muscle Force by Tendon Organs.* Journal of Neurophysiology, 1982. **47**(6): p. 1069-1083.

49. Petit, J., P. Davies, and J.J.A. Scott, *Static sensitivity of tendon organs to tetanic contration of in-series motor units in feline peroneus tertius muscle.* Journal of Physiology, 1994. **481.1**: p. 177-184.

50. Stephens, J.A., R.M. Reinking, and D.G. Stuart, *Tendon Organs of Cat Medial Gastrocnemius: Responses to Active and Passive Forces as a Function of Muscle Length.* Journal of Neurophysiology, 1982. **47**: p. 1217-1231.

51. Mileusnic, M.P., *Mathematical Models of Proprioceptors*, in *Faculty of the School of Engineering*2005, University of Southern California: Los Angeles. p. 192.

52. Gardner, E., *The Distribution and Termination of Nerves in the Knee Joint of the Cat.* Journal of Comparative Neurology, 1944. **80**: p. 11-32.

53. Güçlü, B., et al., *Ovoid geometry of the Pacinian corpuscle is not the determining factor for mechanical excitation.* Somatosensory & Motor Research, 2006. **23**(3/4): p. 119-126.

54. Bolanowski, S.J. and J.J. Zwislocki, *Intensity and Frequency Characteristics of Pacinian Corpuscles. II. Receptor Potentials.* Journal of Neurophysiology, 1984. **51**(4): p. 812-830.

55. Bell, J. and M. Holmes, *Model of the dynamics of receptor potential in a mechanoreceptor.* Mathematical Biosciences, 1992. **110**(2): p. 139-174.

56. Holmes, M.H. and J. Bell, *A model of a sensory mechanoreceptor derived from homogenization.* Siam Journal on Applied Mathematics, 1990. **50**(1): p. 147-166.

57. Lynn, B., *Cutaneous nociceptors*, in *The Neurobiology of Pain*. 1983. p. 97-107.

58. Holden, A.V. and W. Winlow, *Comparative neurobiology of excitation*, in *The Neurobiology of Pain*. 1983. p. 3-28.

59. Xu, F., et al., *Modeling of nociceptor transduction in skin thermal pain sensation.* Journal of Biomechanical Engineering, 2008. **130**(4): p. 041013.

60. Belmonte, C. and F. Cervero, eds. *Neurobiology of Nociceptors*. 1996, Oxford University Press.

61. Biedert, R.M., E. Stauffer, and N.F. Friederich, *Occurrence of free nerve endings in the soft tissue of the knee joint.* The American Journal of Sports Medicine, 1992. **20**(4): p. 430-433.

62. Meneghini, R.M., et al., *The Effect of Retropatellar Fat Pad Excision on Patellar Tendon Contracture and Functional Outcomes after Total Knee Arthroplasty.* The Journal of Arthroplasty, 2007. **22**(6 (suppl. 2)): p. 47-50.

63. Hamarneh, G., et al., *Deformation Analysis of Hoffa's Fat Pad from CT images of Knee Flexion and Extension.* Medical Imaging, 2006. **6143**: p. 703-711.

64. Schaible, H.-G., et al., *Joint pain.* Experimental Brain Research, 2009. **196**(1): p. 153-162.

65. Hodgkin, A.L., A.F. Huxley, and B. Katz, *Measurement of current-voltage relations in the membrane of the giant axon of Loligo.* Journal of Physiology, 1952. **116**: p. 424-448.

66. Hodgkin, A.L. and A.F. Huxley, *The dual effect of membrane potential on sodium conductance in the giant axon of Loligo.* Journal of Physiology, 1952. **116**: p. 497-506.

67. Hodgkin, A.L. and A.F. Huxley, *The components of membrane conductance in the giant axon of Loligo.* Journal of Physiology, 1952. **116**: p. 473-496.

68. Hodgkin, A.L. and A.F. Huxley, *Currents carried by sodium and potassium ions through the membrane of the giant axon of Loligo.* Journal of Physiology, 1952. **116**: p. 449-472.

69. Noble, D., *A modification of the Hodgkin-Huxley equations applicable to purkinje fibre action and pace-maker potentials.* Journal of Physiology, 1962. **160**: p. 317-352.

70. Cannon, R. and M. Nolan, *PSICS - the Parallel Stochastic Ion Channel Simulator*, 2011.

71. FitzHugh, R., *Mathematical models of excitation and propagation in nerve*, in *Biological Engineering*, H.P. Schwan, Editor. 1969, McGraw-Hill: New York. p. 1-85.

72. FitzHugh, R., *Impulses and physiological states in theoretical models of nerve membrane.* Biophysical Journal, 1961. **1**(6): p. 445-466.

73. Murray, J.D., *Mathematical Biology*. 2nd, corrected ed. 1993, Heidelburg: Springer-Verlag.

74. Hodgkin, A.L. and A.F. Huxley, *Resting and action potentials in single nerve fibres.* Journal of Physiology, 1945. **104**: p. 176-195.

75. Nemoto, I., et al., *Behaviour of Solutions of the Hodgkin-Huxley Equations and its Relation to Properties of Mechanoreceptors.* Biophysical Journal, 1975. **15**(5): p. 469-479.

76. Fowler, A.C., *Mathematical Models in the Applied Sciences*. Cambridge Texts in Applied Mathematics. 1997: Cambridge University Press.

77. Kagorodnyuk, V.P. and S.J. Brookes, *Transduction Sites of Vagal Mechanoreceptors in the Guinea Pig Esophagus.* The Journal of Neuroscience, 2000. **20**(16): p. 6249-6255.

78. Eberl, C. *Digital Image Correlation and Tracking*. File Exchange 2006 [cited 2012; Available from: http://www.mathworks.co.uk/matlabcentral/fileexchange/12413.

79. Grigg, P., A.H. Hoffman, and K.E. Fogarty, *Properties of Golgi-Mazzoni afferents in cat knee joint capsule, as revealed by mechanical studies of isolated joint capsule.* J Neurophysiol, 1982. **47**(1): p. 31-40.

80. Campbell, J.N. and R.A. Meyer, *Cutaneous nociceptors*, in *Neurobiology of Nociceptors*, C. Belmonte, Editor. 1996, Oxford University Press.

81. Segal, P. and M. Jacob, *The Knee*. 1984, Somerset: Wolfe Medical Publications Ltd.

82. WebMD. *Knee Pain Health Center*. 2010 [cited 2012 25/05/2012]; Available from: http://www.webmd.com/pain-management/knee-pain/picture-of-the-knee.

83. Kellgren, J.H. and E.P. Samuel, *The sensitivity and innervation of the articular capsule.* Journal of Bone and Joint Surgery-British Volume, 1950. **32**(1): p. 84-92.

84. Prosé, L.P., *Anatomy of the Knee Joint of the Cat.* Acta Anatomica, 1984. **119**(1): p. 40-48.

85. Herzog, W., et al., *Material and functional properties of articular cartilage and patellofemoral contact mechanics in an experimental model of osteoarthritis.* Journal of Biomechanics, 1998. **31**(12): p. 1137-1145.

86. Shepherd, D.E.T. and B.B. Seedom, *Thickness of human articular cartilage in joints of the lower limb.* Annals of the Rheumatic Diseases, 1999. **58**: p. 27-34.

87. Proffen, B.L., et al., *A comparative anatomical study of the human knee and six animal species.* The Knee, 2012. **19**(4): p. 493-499.

88. Grood, E.s., S.F. Stowers, and F.R. Noyes, *Limits of Movement in the Human Knee; effect of sectioning the posterior cruciate ligament and posterolateral structures.* The Journal of Bone & Joint Surgery, 1988. **70-A**(1): p. 88-97.

89. MacFadden, L.N. and N.A.T. Brown, *Biarticular hip extensor and knee flexor muscle moment arms of feline hindlimb.* Journal of Biomechanics, 2007. **40**: p. 3448-3457.

90. Maitland, M.E., et al., *Method to Assess In Vivo Knee Stability Longitudinally in an Animal Model of Ligament Injury.* Journal of Orthopaedic Research, 1998. **16**: p. 441-447.

91. Ferrell, W.R., *The adequacy of stretch receptors in the cat knee joint for signalling joint angle throughout a full range of movement.* Journal of Physiology, 1980. **299**: p. 85-99.

92. Weiss, J.A. and J.C. Gardiner, *Computational Modeling of Ligament Mechanics.* Critical Reviews in Bioimedical Engineering, 2001. **29**(4): p. 1-70.

93. Noyes, F.R. and E.S. Grood, *The Strength of the Anterior Cruciate Ligament in Humans and Rhesus Monkeys.* Journal of Bone and Joint Surgery, 1976. **58**(8): p. 1074-1082.

94. Komatsu, K., et al., *Comparison of Biomechanical Properties of the Incisor Periodontal Ligament Among Different Species.* The Anatomical Record, 1998. **250**: p. 408-417.

95. Provenzano, P.P., et al., *Subfailure damage in ligament: a structural and cellular evaluation.* Journal of Applied Physiology, 2002. **92**: p. 362-371.

96. Martin, R.B., *Biomaterials*, in *Introduction to Bioengineering*, S.A. Berger, W. Goldsmith, and E.R. Lewis, Editors. 1996, Oxford University Press Inc.: New York.

97. Skalak, R. and S. Chien, *Handbook of Bioengineering*. 1986, New York: McGraw-Hill.

98. Miller-Young, J.E., N.A. Duncan, and G. Baroud, *Material properties of the human calcaneal fat pad in compression: experiment and theory.* Journal of Biomechanics, 2002. **35**(12): p. 1523-1531.

99. Verdejo, R. and N.J. Mills, *Heel-shoe interactions and the durability of EVA foam running-shoe midsoles.* Journal of Biomechanics, 2004. **37**: p. 1379-1386.

100. Gefen, A., M. Megido-Ravid, and Y. Itzchak, *In vivo behavior of the human heel pad during the stance phase of gait.* Journal of Biomechanics, 2001. **34**: p. 1661-1665.

101. Limbert, G. and M. Taylor, *On the constitutive modeling of biological soft connective tissues. A general theoretical framework and explicit forms of the tensors of elasticity for strongly anisotropic continuum fiber-reinforced composites at finite strain.* International Journal of Solids and Structures, 2002. **39**: p. 2343-2358.

102. Decraemer, W.F., et al., *A NON-LINEAR VISCOELASTIC CONSTITUTIVE EQUATION FOR SOFT BIOLOGICAL TISSUES, BASED UPON A STRUCTURAL MODEL.* Journal of Biomechanics, 1980. **13**(7): p. 559-564.

103. Sanjeevi, R., *A VISCOELASTIC MODEL FOR THE MECHANICAL-PROPERTIES OF BIOLOGICAL-MATERIALS.* Journal of Biomechanics, 1982. **15**(2): p. 107-109.

104. Weiss, J.A., et al., *Three-dimensional finite element modeling of ligaments: Technical aspects.* Medical Engineering & Physics, 2005. **27**: p. 845-861.

105. Chandler, E.A., *Feline Medicine and Therapeutics*. 2nd ed. 1994: Blackwell Scientific.

106. Burkholder, T.J. and T.R. Nichols, *Three-Dimensional Model of the Feline Hindlimb.* Journal of Morphology, 2004. **261**: p. 118-129.

107. *DADS*, 1999, LMS/CADSI: Coralville, IA.

108. Chizari, M. and B. Wang, *3D Numerical Analysis of an ACL Reconstructed Knee*, in *2009 SIMULIA Customer Conference*2009.

109. Baldwin, M.A., et al., *Dynamic finite element knee simulation for evaluation of knee replacement mechanics.* Journal of Biomechanics, 2012. **45**: p. 474-483.

110. Bendjaballah, M.Z.e.a., *Finite element analysis of human knee joint in varus-valgus.* Clinical Biomechanics, 1997. **12**(3): p. 139-148.

111. D'Lima, D.D., et al., *Impact of patellofemoral design on patellofemoral forces and polyethylene stresses.* Journal of Bone and Joint Surgery [Am], 2003. **85-A Suppl 4**: p. 85-93.

112. (VSG), V.S.G., *Avizo*, 2010.

113. Sun, Y., E.C. Teo, and Q.H. Zhang, *Discussions of Knee Joint Segmentation*, in *International Conference on Biomedical and Pharmaceutical Engineering* 2006: Singapore.

114. Limbert, G., M. Taylor, and J. Middleton, *Three-dimensional finite element modelling of the human ACL: simulation of passive knee flexion with a stressed and stress-free ACL.* Journal of Biomechanics, 2004. **37**: p. 1723-1731.

115. Shi, J., et al., *Sensitivity analysis of a cemented hip stem to implant position and cement mantle thickness.* Computer Methods in Biomechanics and Biomedical Engineering, 2013: p. 1-14.

116. Armstrong, C.G.M., V.C., *Variations in the intrinsic mechanical properties of human articular cartilage with age, degeneration, and water content.* The Journal of Bone & Joint Surgery, 1982. **64**: p. 88-94.

117. Systemes, D., *Abaqus/CAE*, 2009.

118. Holzapfel, G.A. and T.C. Gasser, *A viscoelastic model for fiber-reinforced composites at finite strains: Continuum basis, computational aspects and applications.* Computer Methods in Applied Mechanics and Engineering, 2001. **190**(34): p. 4379-4403.

119. Peña, E., et al., *An anisotropic visco-hyperelastic model for ligaments at finite strains. Formulation and computational aspects.* International Journal of Solids and Structures, 2007. **44**(3–4): p. 760-778.

120. Holzapfel, G.A., T.C. Gasser, and R.W. Ogden, *A new constitutive framework for arterial wall mechanics and a comparative study of material models.* Journal of Elasticity, 2000. **61**(1-3): p. 1-48.

121. Wilson, W.T., et al., *Comparative Analysis of the Structureal Properties of the Collateral Ligaments of the Human Knee.* Journal of Orthopaedic & Sports Physical Therapy, 2012. **42**(4): p. 345-351.

122. Noyes, F.R., *Noyes' Knee Disorders: Surgery, Rehabilitation, Clinical Outcomes*. 2009, Philadelphia: Saunders.

123. Jayson, M.I.V. and A.S.J. Dixon, *Intra-articular pressure in rheumatiod arthritis of the knee: I. Pressure changes during passive joint distension.* Annals of Rheumatic Diseases, 1970. **29**: p. 261-265.

124. Jayson, M.I.V. and A.S.J. Dixon, *Intra-articular pressure in rheumatoid arthitis of the knee: III. Pressure changes during joint use.* Annals of Rheumatic Diseases, 1970. **29**: p. 401-408.

125. Brantigan, O.C. and A.F. Voshell, *The Mechanics of Ligaments and Menisci of the Knee Joint.* Journal of Bone and Joint Surgery, 1941. **23**: p. 44-66.

126. Barrett, D.S., A.G. Cobb, and G. Bentley, *Joint proprioception in normal, osteoarthritic and replaced knees.* Journal of Bone and Joint Surgery, 1991. **73B**: p. 53-56.

127. Pap, G., et al., *Proprioception after total knee arthroplasty - A comparison with clinical outcome.* Acta Orthopaedica Scandinavica, 2000. **71**(2): p. 153-159.

128. Solomonow, M. and M. Krogsgaard, *Sensorimotor control of knee stability. A review.* Scandinavian Journal of Medicine & Science in Sports, 2001. **11**(2): p. 64-80.

129. Khalsa, P.S. and P. Grigg, *Responses of Mechanoreceptor Neurons in the Cat Knee Joint Capsule Before and After Anterior Cruciate Ligament Transection.* Journal of Orthopaedic Research, 1996. **14**: p. 114-122.

130. Wilk, K.E., et al., *Recent Advances in the Rehabilitation of Anterior Cruciate Ligament Injuries.* Journal of Orthopaedic & Sports Physical Therapy, 2012. **42**(3): p. 153-171.

131. Friden, T., et al., *Review of knee proprioception and the relation to extremity function after an anterior cruciate ligament rupture.* Journal of Orthopaedic & Sports Physical Therapy, 2001. **31**(10): p. 567-576.

132. Iversen, B.F., et al., *Implications of muscular defence in testing for the anterior drawer sign in the knee. A stress radiographic investigation.* American Journal of Sports Medicine, 1989. **17**(3): p. 409-413.

133. Tashman, S., et al., *Kinematics of the ACL-deficient canine knee during gait: serial changes over two years.* Journal of Orthopaedic Research, 2004. **22**: p. 931-994.

134. Moorehead, J.D., et al., *Measurement of tibial displacement during the anterior drawer test, using a magnetic tracking device.* Journal of Bone and Joint Surgery British, 2006. **88-B**(SUPP III 412).

135. Torg, J.S., W. Conrad, and V. Kalen, *Clinical Diagnosis of Anterior Cruciate Ligament Instability in the Athlete.* The American Journal of Sports Medicine, 1976. **4**(2).

136. Zhang, L.Q., et al., *Six degrees-of-freedom kinematics of ACL deficient knees during locomotion-compensatory mechanism.* Gait Posture, 2003. **17**(1): p. 34-42.

137. Mine, T., et al., *Innervation of nociceptors in the menisci of the knee joint: an immunohistochemical study.* Archives of Orthopaedic and Trauma Surgery, 2000. **120**(3): p. 201-204.